Stony Brook University

Biomimetic Calcium Phosphate Coatings Synthesized by Electrochemical Deposition and Air Plasma Spray: Morphology, Composition and Bioactive Performance

A Dissertation Presented

by

Ling Li

to

The Graduate School

in Partial Fulfillment of the

Requirements

for the Degree of

Doctor of Philosophy

in

Materials Science and Engineering

Stony Brook University

August 2013

Stony Brook University

The Graduate School

We, the dissertation committee for the above candidate for the

Doctor of Philosophy degree, hereby recommend

acceptance of this dissertation.

Christopher Weyant – Dissertation Advisor
Assistant Professor, Department of Materials Science and Engineering

Yizhi Meng - Chairperson of Defense
Assistant Professor, Department of Materials Science and Engineering

Dilip Gersappe- Committee Member
Professor, Graduate Program Director, Department of Materials Science and Engineering

Lisa Miller- Committee Member
Associate Division Director, Photon Sciences Directorate at Brookhaven National Laboratory

This dissertation is accepted by the Graduate School

Charles Taber
Interim Dean of the Graduate School

Biomimetic Calcium Phosphate Coatings Synthesized by Electrochemical Deposition and Air Plasma Spray: Morphology, Composition and Bioactive Performance

by

Ling Li

Doctor of Philosophy

in

Materials Science and Engineering

Stony Brook University

2013

In this project, with the aim to develop bioactive biomimetic coatings for dental and orthopedic applications, calcium phosphate based coatings deposited by electrochemical deposition and plasma spray were investigated. Different combinations of process parameters were used to achieve coatings with various chemical compositions and morphologies. The obtained coating composition was investigated by energy dispersive X-ray spectroscopy and X-ray diffraction. The microstructure of the coatings were studied through scanning electron microscopy while the cytocompatibility and bioactivity of the strontium-doped calcium phosphate coatings were evaluated using bone cell culture using MC3T3-E1 osteoblast-like cells.

A set of designed experiments were performed to study the process-product-performance relationship. The experimental results suggested that the properties of the coatings were dramatically impacted by process parameters during both of the air plasma spray and electrochemical deposition processes.

For electrochemical deposition, the influences of different process parameters such as current density, concentration, temperature and pH value of the electrolyte as well as the dose of strontium were investigated. A thermodynamic model was built to describe the calcium phosphate deposition behaviors in this process, which enhanced the understanding of this process, provided the possibility to predict and tailor the properties of deposited coatings.

As for air plasma sprayed calcium phosphate coating, the links between process parameters—> particle state—> coating properties —> performance were successfully built through process map strategy. It was found that current and total gas flow were the key process parameters in this process, which controlled in-flame particle state, the morphologies of single splats, and eventually coating properties such as coating's phase, microstructure as well as coating thickness and the bioactivities of the coatings.

The in-vitro cell culture experiment indicated that coating morphology and composition had dramatic impact on the behaviors of the cells: faceted monetie produced by electrodeposition was the most suitable substrate for the attachment and growth of the cells, compared to smoother air plasma sprayed calcium phosphate coatings and electrochemical deposited needle-like hydroxyapatite. Furthermore, the incorporation of strontium into calcium phosphate coatings leaded to enhanced cell proliferation suggesting its potential benefits for improving the bioactivity of the calcium phosphate coatings.

Dedicated to my Family
献给我的家人

Table of Contents

List of Tables

List of Figures

List of Abbreviations

CaP	Calcium phosphate
HA/HAP	Hydroxyapatite
TTCP	Tetracalcium phosphate
CDHA	Calcium-deficient hydroxyapatite
TCP	Tricalcium phosphate
OCP	Octacalcium phosphate
DCPD	Hydrated calcium phosphate/Brushite
Ca	Calcium
Sr	Strontium
APS	Air plasma spray
ECD	Electrochemical deposition
T	Temperature
TGF	Total gas flow
V	Velocity
MI	Melting index
KE	Kinetic energy
XRD	X-ray diffraction
SEM	Scanning electron microscope
SBF	Simulated body fluid
S	Supersaturation
SI	Supersaturation index

IAP	Ion activity product
K_{sp}	Thermodynamic solubility product
ΔG	Gibbs free energy change
R	Gas constant = 8.314J/ (mol·K)
C	Concentration
i_0	Applied current density
D	Diffusion coefficient
t	Time
F	Faraday constant
ΔE	Energy change
$f(\theta)$	The contact angle function
J	Nucleation rate
P	Probability
v	Volume of primitive crystal cell
γ	Interfacial energy
k	Boltzmann constant
D	Diameter
ρ	Density
v	Volume
P	Porosity
DE	Deposit efficiency
PBS	Phosphate-buffered saline
HMDS	hexamethyldisilazane)

Acknowledgments

First, I would like to give my most sincere thanks to my advisor Dr. Christopher. Weyant and co-advisor, Dr. Yizhi Meng for their guidance and support in my Ph.D. Study. Without their enlightening advices and constant encouragement, this work would not have been possible.

I would like to thank all my dissertation committee members for their inspiring discussions and suggestions.

I truly appreciate Dr. Jim Quinn for his help in SEM, XRD experiments and a lot of useful advices and encouragement.

I should also want to thank Prof. Sanjay Sampath in CTSR, Prof. Scott McLennan from Geoscience department, Prof. Michael Hadjiargyrou from Biomedical department, Dr. Demytro Nykypanchuk, Lihua Zhang from BNL for proving the great experiment environment and facilities during my research.

I am indebted to Kathryn Dorst and Xia Lu who patiently taught me how to do cell culture experiment.

I would also like to acknowledge Mr. Glenn Bancke, Kentaro Shinoda, Yikai Chen and Jose Colmenares for preparing air plasma sprayed samples for the process map study.

I am thankful to Dr. B. W. Choi, Junghan Kim and Lorena Bejarano for teaching me a lot skills regarding sample preparing and instrument operation that I used throughout my Ph.D. study.

I am really thankful to Dilip, Lynn, Debby and Chandrani, who always gave me help and support whenever I need them during the six years.

I am grateful to other members from CTSR and Meng's lab for all their help and support during my study. I feel so luck to meet every one of them during my Ph.D. life.

Last, but never least, I owe everything to my family, my dearest parents and husband, for their unconditional loves and continues encouragements.

Publications

1. **Ling Li**, Chris Weyant, Xia Lu, Yizhi Meng , Influence of Strontium on the Phase, Structure and Bioactivity of Calcium Phosphate Coatings Synthesized by Electrochemical Deposition.2012 MRS, San Francisco (Oral presentation)
2. **Ling Li**, Chris Weyant, Xia Lu, Yizhi Meng , Comparison Study of Biomimetic Strontium-Doped Calcium Phosphate Coatings by Electrochemical Deposition and Air Plasma Spray: Morphology, Composition and Bioactive Performance, J Mater Sci: Mater Med, 23: 2359–2368,2012
3. **Ling Li**, Chris Weyant, Amanda Chin, Yizhi Meng, Electrochemical Deposition of Strontium Doped Hydroxyapatite Coatings. 2011 Materials Sciences and Technology, Columbus, Oct 16-20, 2011. (Oral presentation)
4. Chris Weyant, **Ling Li**, Amanda Chin, Yizhi Meng, Electrochemical Deposition of Strontium Doped Hydroxyapatite Coatings. PACRIM 9 Cairns, Queensland, Australia, 2011. (Oral presentation)

Chapter 1

INTRODUCTION

In modern medicine, artificial implants are frequently used to treat fractures or replace damaged bone and teeth. The design of the orthopedic implants is very complex. It faces several issues including rapid fixation, long-term stabilization in body, and biocompatibility, which means the implant materials should not have adverse effects on the surrounding living tissue of the host.

Therefore, before the designing of implants, there should be some understanding and investigation of the structure and properties of the natural bone that is being substituted, the properties and function of the biomaterials used, and the techniques used to process the materials. This information will allow for making a suitable product to meet the system's requirements.

1.1 Functions and Structure of Bone

Bone is live, mineralized, constantly changing hard tissue which plays a very important role in the body[1]. It provides a frame for support and protection of vital organs and housing of bone marrow as well as attachment to muscle groups, working with them to achieve the movement of the body[2, 3]. The structure of bone is composed of three major parts, as shown in Fig.1-1: bone matrix, cellular component and blood vessels.

(1) The bone matrix consists of two main components: collagen and mineral phase (Fig.1-2) [4]. The first is organic matter, primarily type I collagen fibers which are made up of bundles of fibrils to provide tensile strength. The second is inorganic matter, which is an analogue of calcium phosphate nano crystals. These substances can be seen under electron microscope. Its mineral crystals contribute to the hardness of bone, and resist bending and compression[5].

(2) Cellular component consists of bone cells and an intercellular matrix. According to their functions, morphology and location, bone cell can be classified into three types:

• Osteoblasts — the bone building cells. They synthesize bone extracellular matrix and control its mineralization. When active, they provide the enzyme to hydrolyze

pyrophosphate, which will benefit the formation of saturation state of calcium and phosphate, and thus promote the process of calcification [6-8].

• Osteocytes — when osteoblasts are incorporated into bone matrix during the growth of bone, they become osteocytes. Osteocytes have extensive dendritic processes, by which they communicate with other bone cells. They also have the ability to build bone, and may be involved into the process of bone absorption.

• Osteoclasts—cells responsible for the dissolution and absorption of bone. They are critical in maintaining bone mass and controlling the remodeling process of bone. [9, 10].

(3) Blood vessels comprise the veins and arteries. They bring foodstuffs to the bone and take waste products away from bone[11].

1.2 Implants and Biomaterials in Dental and Orthopedic Application

Due to the reasons such as age deterioration or accidents, damage to bone and teeth is common in life. In modern medicine, orthopedic implants have been developed, which has been successfully used to restore the function of bone and improve the life quality of million individuals suffering from bone damage[12].

Choosing the appropriate materials is very essential in the design of orthopedic implants. Various biomaterials have been used to fabricate the implants. According to the how they behavior in body tissues and fluids, those materials can be classified into bioactive, bioinert and biodegradable/bioabsorbable materials, as shown in table 1-1.

Table. 1-1: Types of biomaterials [12-15]

Type of biomaterials	Typical behaviors	Attachment modes	Examples
Nearly inert	Biological inactive. Has minimal interactions with surrounding tissue	Mechanical interlock between implant and tissue (morphological fixation)	Titanium, alumina, Cr–Co alloys, zirconia, ultrahigh molecular weight polyethylene, carbon
Bioactive	Initiates specific biological reactions at the interface of the implanted material and host tissue, and therefore built a bond between them	Chemical or biological interfacial bond with host tissues at the interface (bioactive fixation)	Bioglasses, hydroxyapatite and bioactive glass-ceramics
Resorbable/ degradable	Can dissolve or be resorbed gradually in the host body and finally can be replaced by advancing host tissue	Replacement with new growing natural host tissues	Calcium sulfate , calcium carbonate,

Since the key factor for the successful fixation of implants is to build a reliable interface between the implant and bone[16], bioactive material, especially calcium phosphates, can induce specific biological reactions in the tissue/materials interface, and therefore built a bond between the host tissue and implant [17, 18], they are considered to be the most promising biomaterials used in dental and orthopedic applications.

However, those materials' mechanical performance is poor, therefore, they usually cannot be used alone to build load bearing parts, but are applied as a top coating on a substrate. The substrate is usually made of bioinert metal, for example, titanium alloy Ti6Al4V or stainless steel. In Table. 1-2, the mechanical properties of bone and other biomaterials are listed and compared. Through combining a bone-bonding ceramic

coating and the metal substrate with good mechanical properties, the optimized combination of bioactive performance and mechanical properties can be obtained.

Table. 1-2: Mechanical properties of bone and orthopedic biomaterials [12, 19-23]

Material	Elastic Modulus (GPa)	Tensile Strengh (MPa)	Hardness (HV)
cortical bone	7~30	50~150	44.1 ~ 51.7
cancellous bone	0.1~1	1.5~3	30.8~34.1
Ti-6Al-4V	116	900	310
316L stainless steel	193	540	220
sintered HA	16~73	50~110	500~800

1.3 Bioactive Calcium Phosphate Ceramics

Calcium phosphate ceramics belong to bioactive materials, and are well known for their orthopedic applications. As discussed before, calcium phosphate (CaP) ceramics are quite similar to the mineral phase in bone, therefore they have been considered as the most suitable materials for bone repair and replacement. They have the ability to enhance formation of new osseous tissue in the interface of implant and host bone by providing a high calcium and phosphorus-rich environment around the interface between bone and the implant [16], thus promoting new bone growth into the prosthesis.

Among various types of calcium phosphate, due to its chemical and structure closest to nature bone and stabilization during implantation, stoichiometric hydroxyapatite (HA) is the first Ca-P ceramic attracting enormous interest, and was once considered to be the most favorite calcium phosphate phase for orthopedic prosthetics applications. However, after several years, researchers have determined that HA

(especially highly crystallized HA) may not always be the best material for bone applications because of its low solubility.

Solubility is very important for the bioactivity performances calcium phosphate because it controls how fast the calcium and phosphate ions can be release from the implant materials to the surround environment. And in some certain cases, it is more desirable to have a coating that can be gradually resorbed totally or partially during implantation and leave the space for new bone to grow into the implant[24].

Therefore, various Ca-P based ceramics, such as octacalcium phosphate [25, 26](Ca_8H_2 $(PO_4)_6.5H_2O$, OCP), monetite ($CaHPO_4$, ADCP)[27-29], tricalcium phosphate [30]($Ca_3(HPO_4)_2$, TCP), tetracalcium phosphate [31, 32]($CaO.Ca_3(HPO_4)_2$, TTCP), as well as their amorphous phases[33], have been introduced for biomedical applications, which are shown in Table 1-3.

These calcium phosphates have various chemical compositions and different solubilities. Generally speaking, as the calcium-to-phosphate ratio decreases in the Ca-P ceramic, the rate of dissolution increases. [12] Monetite which has a Ca/P ratio of 1, dissolves faster than hydroxyapatite which has a Ca/P ratio of 1.67. Also, they also have dissimilar bioactive behaviors. Detsch et al.'s study [34] showed that the bone cells responded in a different manner to HA and TCP, and they proposed that calcium phosphate-based ceramics as a bone substitute material can be chosen either for their fast degradation (such as TCP) or for the slow remodeling of the biomaterial (such as HA). Therefore the choice of ceramic depends on the location and size of the bone defect and the patient's personal characteristics.

Table. 1-3: Chemical name, mineral name, and composition of various calcium phosphate ceramics. [25-33, 35, 36]

Name	Chemical formula	Ca/P molar ratio	Abbreviation
Tetracalcium phosphate	$CaO{\cdot}Ca_3(HPO_4)_2$	2.0	TTCP
Hydroxyapatite	$Ca_{10}(HPO_4)_6{\cdot}\ (OH)_2$	1.67	HA/HAP
Calcium-deficient hydroxyapatite	$Ca_{10-x}(HPO_4)_x{\cdot}(PO_4)_{6-x}\ (OH)_{2-x}$ ($0 < x < 1$)	1.5~1.67	CDHA
α-Tricalcium phosphate	α-$Ca_3(PO_4)_2$	1.5	α-TCP
β- Tricalcium phosphate	β- $Ca_3(PO_4)_2$	1.5	β-TCP
Octacalcium phosphate	$Ca_8(HPO_4)_2(PO_4)_4{\cdot}5H_2O$	1.33	OCP
Hydrated calcium phosphate/Brushite	$CaHPO_4{\cdot}2H_2O$	1.0	DCPD
Dicalcium phosphate anhydrous /Monetite	$CaHPO_4$	1.0	DCPA /ADCP
Calcium pyrophosphate	$Ca_2P_2O_7$	1.0	CPP
Monocalcium phosphate monohydrate	$Ca(H_2PO_4)_2{\cdot}H_2O$	0.5	MCPM
Monocalcium phosphate anhydrous	$Ca(H_2PO_4)_2$	0.5	MCPA

1.4 Biomimetic Ion Substituted Calcium Phosphates

1.4.1 Inspirations from the Nature Bone

Although stoichiometric calcium phosphate has the ability to bond to bone, the rate of osseointegration is relatively slow compared to the bonding speed between nature bones[27] [37]. That is because although the inorganic phase in natural bone has similar chemical composition as calcium phosphate, it also incorporates doped ions such as $(CO_3)^{2-}$,F^- , Mg^{2+}, Sr^{2+}, Zn^{2+} and Na^+ in its structure[38]. Therefore developing ion substituted calcium phosphates that mimic the composition and function of bone mineral can be a potential solution. Furthermore, a series of experiments conducted by Suzuki and coworkers found that Ca^{2+} of calcium phosphate can be exchanged with other metal ions in aqueous media [39-43]. Therefore synthesis of this type of chemical modified calcium phosphates is practical, and it is anticipated that the structure and properties of calcium phosphate can be modified by ion- substitution.

1.4.2 The Active Element: Strontium

Among various doped ions found in bone mineral, strontium (Sr) is a very special element, which falls just below calcium in the periodic table. Since Sr has the same valence (2^+) as Calcium (Ca) and its ionic radius (1.12 Å) is similar with that of calcium (0.99 Å)[44]. In the human body, ionic strontium has similar metabolic pathway as calcium [45, 46], and can be easily incorporated in the mineral structure of bone and teeth replacing calcium.

As shown in Fig. 1-3, strontium has the ability to promote collagen and non-collagen protein synthesis, stimulate the replication of osteoblast as well as inhibit osteoclast differentiation function. Therefore it can induce a positive effect on new bone growth, increase bone density and prevent undesirable bone resorption. [47-53]

1.4.3 Strontium Doped Calcium Phosphates

Recently, strontium-substituted calcium phosphates have been developed which shows enhance osteoblast activity compared to their pure calcium counterparts. The

substitution of strontium into calcium phosphate will cause the expansion of lattice, because the atomic size of strontium is larger than that of calcium. Thus, incorporation of strontium can alter the dissolution behavior and growth kinetics of calcium phosphate. Chen et al. suggested that the doping of strontium gives rise to more lattice distortions in the crystal structure of calcium phosphate and therefore increases calcium phosphate's solubility[54]. The increase of solubility may also benefit the bioactivity performance of this type of material, due to the sufficient calcium phosphate ions provided.

1.5 Methods to Produce Calcium Phosphate-Based Coatings

As mentioned before, due to their poor mechanical properties and intrinsic brittleness, in most applications, calcium phosphate- based bioceramics are used in the form of a coating on a substrate. Various methods have been developed to produce calcium phosphate-based coatings such as plasma spray [55, 56], electrochemical deposition[57], electrophoretic method[58], laser-deposition [59], sol-gel [60, 61], and RF sputtering [62]. Among these methods, electrochemical deposition and plasma spray are two most commonly used technologies.

1.5.1 Air Plasma Spray

As the most traditional way to deposit Ca-P coatings, air plasma spray (APS) is by far the most popular and currently clinically accepted technology [63, 64]. The technique is basically obtaining a top coating at extremely high temperate by spraying of heated softened or molten material onto a substrate. Fig. 1-4 shows the schematic view of plasma spray technique. As shown in the figure, the most important part of the plasma spray equipment is the plasma spray gun, which comprises a copper anode and tungsten cathode. When plasma gas (usually is the combination of hydrogen, argon, nitrogen, helium) passes through the electric arc struck by a huge voltage discharge between electrodes, the extremely high temperature plasma stream is initiated. The material to be deposited is called feedstock, which in most cases is in the form of powder. Feedstock of the certain materials is injected into the plasma stream, and then melted and propelled toward the substrate to form flatten splat onto substrate surface, and then cool down.

When numerous splats successive accumulate on the surface of the substrate, a solid coating forms on the surface of the substrate[65].

Fig. 1-6 shows the typical microstructure of plasma sprayed coatings, which is characterized by the existence of flat splats along with sphere unmelted partials and various pores and cracks including: globular pores (due to the entrapment of air during deposition), interlamellar cracks (result from poor wetting/adhesion between the splats as they accumulate to form the coating) and intra-splat microcracks (originate from stress relaxation) [66].

This technique has several advantages compared to the other methods including good control of thickness and high deposition rate. However, plasma spray processing is a very complex technique. There are numerous factors in this process that may affect the spayed coating properties. And with the extremely high process temperature of this technique, the phase transformation and decomposition of calcium phosphate are almost unavoidable, which make the system even more difficult to be controlled. Therefore, building links between process parameters and the properties of plasma sprayed calcium phosphate coatings is quite a challenge.

A lot of studies have been conducted on this topic in order to get better control over the chemical composition and microstructure of plasma sprayed coatings. Some researchers investigated the influence of single parameters: S. M. Mohd et al. found spray power affects coating morphology showing that increasing the spray power level produced coatings containing less unmelted particles and pores [67]; Y. P. Lu et al. investigated the effects of stand-off distance on the coating characteristics[68]; M. F. Morks and A. Kobayashi studied the effect of current on coating microstructure and crystallinity[69]. Other researchers tried to build links between a group of parameters and coating properties: R. McPherson et al.[70] , C.Y.Yang et al.[71] and S. Dyshlovenko et al.[72] studied the relationship between process parameters (torch powder, spraying distance, carrier gas flow rate, composition of plasma forming gas) and chemical composition and morphology of the coatings; L. Sun et al.[73] and K. A. Khor et al.[74] investigated spray power and spray distance's effects on the phase, structure and

microstructure of the HA coatings. The influences of process parameters on the mechanical properties can also be found in some studies [74-76].

1.5.2 Electrochemical Deposition

Another technique, electrochemical deposition, is a relatively new method to fabricate calcium phosphate based coatings. It was first introduced in 1990s [77, 78] and since then it has attracted significant interest in recent years. It has been considered to be the most promising technique to fabricate calcium phosphate based coatings[79].

In the electrochemical deposition, the nucleation and growth of calcium phosphate coating is induced by the ion concentration change in the vicinity of catholically polarized electrodes[80-82].

The simplified experimental setup of electrochemical deposition is shown in Fig 1-5. The system contains an electric source, two electrodes and electrolyte containing calcium and phosphate ions. During electrochemical deposition, voltage is applied between the electrodes, and water is reduced, both of the hydrogen gas and hydroxyl ions are produced on the surface of substrate (cathode). When the increasing concentration of hydroxyl ions reach the critical point, the hydroxyl ions reaction with calcium ions and phosphate groups to form calcium phosphates. After a certain time for stabilization, the calcium coating will be produced on the surface of the substrate.

This method has several advantages over plasma spray including: i) low process temperature; ii) the ability to coat porous, geometrically complex surface; iii) easier control over composition and microstructure of the coating and iv) relatively low cost. However it also has some disadvantages, such as the limitation of thickness of the coating due to the decrease of electroconductivity of the substrate during deposition, and the defects caused by hydrogen gas assembling on the substrate surface.

Various forms of calcium phosphates such as DCPD, OCP, HA can be deposited by electrochemical deposition. Some researchers [83]reported that $CaHPO_4 \cdot 2H2O$ can be directly deposited on the substrate by electrochemical deposition at relatively low temperature (20 ~ 60°C), and then converted into hydroxyapatite by hydrothermal

treatment. while other researcher [84]obtained octacalcium phosphate by this method using revised simulation body fluid as electrolyte at 36.5°C. In some research, it was found that hydroxyapatite usually forms via precursor such as octaclcium phosphate and brushite[85, 86]. However, Zhang et al. also claimed hydroxyapatite can be directly deposited on the substrate without the formation of precursor phase from dilute electrolyte (concentration of Ca^{2+} = 0.61mM)[87, 88]. The synthesized coatings can also be the mixture two or more phases. Achariya Rakngarm's group obtained coating with both of DCPD and OCP under low current density (3mA/cm^2) at room temperature[89], Ye and Shih obtained the combination of DCPD and HA at 60 °C, with cathodic polarization: 10V. Those coatings have various surface morphologies, containing crystals which have different appearance such as needle-like shape[90], plate-like shape[90-92], ribbon or rod-like[93] as well as faceted-crystallites[94].

1.6 Summary of Literature Findings

Calcium phosphates are a kind of bioactive materials widely used in orthopedics and dentistry, mainly due to their similarity to nature bone in chemical composition and structure. They are usually used in the form of coating on the top of metal substrate to obtain optimal combination of bioactivity and mechanical performances.

Among various process methods to synthesize calcium phosphate based coating, plasma spray and electrochemical deposition are two promising techniques which have demonstrated their own advantages as mentioned before. Both of the methods can produce calcium phosphates coatings with different morphologies and phase compositions.

Additionally, the osteoconductivity of pure calcium phosphates is relatively slow. Incorporating strontium into calcium phosphates can better mimic the natural bone, thus may have the potential to achieve improved bioactivity performance.

References Cited

1. Meghji, S., Bone remodelling. Br Dent J, 1992. 172(6): p. 235-242.

2. Mistry, A. and A. Mikos, Tissue Engineering Strategies for Bone Regeneration, in Regenerative Medicine II, I. Yannas, Editor 2005, Springer Berlin Heidelberg. p. 1-22.

3. Chan, G.K. and G. Duque, Age-Related Bone Loss: Old Bone, New Facts. Gerontology, 2002. 48(2): p. 62-71.

4. Rho, J.-Y., L. Kuhn-Spearing, and P. Zioupos, Mechanical properties and the hierarchical structure of bone. Medical Engineering & Physics, 1998. 20(2): p. 92-102.

5. Buckwalter, J. and R. Cooper, Bone structure and function. Instructional course lectures, 1987. 36: p. 27.

6. Stancu, I.C., et al., The in vivo calcification capacity of a copolymer, based on methacryloyloxyethyl phosphate, does not favor osteoconduction. Journal of Biomedical Materials Research Part A, 2004. 69A(3): p. 584-589.

7. Nakano, Y., W.N. Addison, and M.T. Kaartinen, ATP-mediated mineralization of MC3T3-E1 osteoblast cultures. Bone, 2007. 41(4): p. 549-561.

8. Goding, J.W., B. Grobben, and H. Slegers, Physiological and pathophysiological functions of the ecto-nucleotide pyrophosphatase/phosphodiesterase family. Biochimica et Biophysica Acta (BBA) - Molecular Basis of Disease, 2003. 1638(1): p. 1-19.

9. Lerner, U.H., Osteoblasts, Osteoclasts, and Osteocytes: Unveiling Their Intimate-Associated Responses to Applied Orthodontic Forces. Seminars in Orthodontics, 2012. 18(4): p. 237-248.

10. Nakamura, H., Morphology, Function, and Differentiation of Bone Cells. Journal of hard tissue biology, 2007. 16(1): p. 15-22.

11. J.D.Currey, Differences in the blood-supply of bone of different histological types. Quarterly Journal of Microscopical Science, 1960. 101(3): p. 31-370.

12. Ratner, B.D., et al., Biomaterials Science - An Introduction to Materials in Medicine (2nd Edition), Elsevier.

13. Cao, W. and L.L. Hench, Bioactive materials. Ceramics International, 1996. 22(6): p. 493-507.

14. Jayaswal, G., S. Dange, and A. Khalikar, Bioceramic in dental implants: A review. The Journal of Indian Prosthodontic Society, 2010. 10(1): p. 8-12.

15. Sola, A., et al., Bioactive glass coatings: a review. Surface Engineering, 2011. 27(8): p. 560-572.

16. Cheang, P. and K.A. Khor, Addressing processing problems associated with plasma spraying of hydroxyapatite coatings. Biomaterials, 1996. 17(5): p. 537-544.

17. Hench, L., The story of Bioglass<sup>®</sup&gt. Journal of Materials Science: Materials in Medicine, 2006. 17(11): p. 967-978.

18. Liu, X., et al., Bioactive calcium silicate ceramics and coatings. Biomedicine & Pharmacotherapy, 2008. 62(8): p. 526-529.

19. Sun, L., et al., Material fundamentals and clinical performance of plasma-sprayed hydroxyapatite coatings: A review. Journal of Biomedical Materials Research, 2001. 58(5): p. 570-592.

20. Laroudie, F., C. Tassin, and M. Pons, Hardening of 316L stainless steel by laser surface alloying. Journal of Materials Science, 1995. 30(14): p. 3652-3657.

21. Dall'Ara, E., et al., Reduced tissue hardness of trabecular bone is associated with severe osteoarthritis. Journal of biomechanics, 2011. 44(8): p. 1593-1598.

22. Zioupos, P., M. Gresle, and K. Winwood, Fatigue strength of human cortical bone: Age, physical, and material heterogeneity effects. Journal of Biomedical Materials Research Part A, 2008. 86A(3): p. 627-636.

23. Prokopiev, O. and I. Sevostianov, Dependence of the mechanical properties of sintered hydroxyapatite on the sintering temperature. Materials Science and Engineering: A, 2006. 431(1–2): p. 218-227.

24. Ducheyne, P. and Q. Qiu, Bioactive ceramics: the effect of surface reactivity on bone formation and bone cell function. Biomaterials, 1999. 20(23–24): p. 2287-2303.

25. Suzuki, O., et al., Bone formation enhanced by implanted octacalcium phosphate involving conversion into Ca-deficient hydroxyapatite. Biomaterials, 2006. 27(13): p. 2671-2681.

26. Barrère, F., et al., Osteogenecity of octacalcium phosphate coatings applied on porous metal implants. Journal of Biomedical Materials Research Part A, 2003. 66A(4): p. 779-788.

27. Habibovic, P., et al., Osteoconduction and osteoinduction of low-temperature 3D printed bioceramic implants. Biomaterials, 2008. 29(7): p. 944-953.

28. Zavgorodniy, A.V., et al., Adhesion of a chemically deposited monetite coating to a Ti substrate. Surface and Coatings Technology, 2012. 206(21): p. 4433-4438.

29. Tamimi, F., et al., The effect of autoclaving on the physical and biological properties of dicalcium phosphate dihydrate bioceramics: Brushite vs. monetite. Acta Biomaterialia, 2012. 8(8): p. 3161-3169.

30. Akao, M., et al., Dense polycrystalline β-tricalcium phosphate for prosthetic applications. Journal of Materials Science, 1982. 17(2): p. 343-346.

31. Kim, H., et al., Control of phase composition in hydroxyapatite/tetracalcium phosphate biphasic thin coatings for biomedical applications. Journal of Materials Science: Materials in Medicine, 2005. 16(10): p. 961-966.

32. Romeo, H. and M. Fanovich, Synthesis of tetracalcium phosphate from mechanochemically activated reactants and assessment as a component of bone cements. Journal of Materials Science: Materials in Medicine, 2008. 19(7): p. 2751-2760.

33. Nagano, M., et al., Differences of bone bonding ability and degradation behaviour in vivo between amorphous calcium phosphate and highly crystalline hydroxyapatite coating. Biomaterials, 1996. 17(18): p. 1771-1777.

34. Detsch, R., H. Mayr, and G. Ziegler, Formation of osteoclast-like cells on HA and TCP ceramics. Acta Biomaterialia, 2008. 4(1): p. 139-148.

35. Kitsugi, T., et al., Four calcium phosphate ceramics as bone substitutes for non-weight-bearing. Biomaterials, 1993. 14(3): p. 216-224.

36. Dorozhkin, S.V., Calcium orthophosphates and human beings. Biomatter, 2012. 2(2): p. 53-70.

37. Klein, C.P.A.T., et al., Biodegradation behavior of various calcium phosphate materials in bone tissue. Journal of Biomedical Materials Research, 1983. 17(5): p. 769-784.

38. Bigi, A., et al., Chemical and structural characterization of the mineral phase from cortical and trabecular bone. Journal of Inorganic Biochemistry, 1997. 68(1): p. 45-51.

39. Suzuki, T., T. Hatsushika, and Y. Hayakawa, Synthetic hydroxyapatites employed as inorganic cation-exchangers. Journal of the Chemical Society, Faraday Transactions 1: Physical Chemistry in Condensed Phases, 1981. 77(5): p. 1059-1062.

40. Suzuki, T., K. Ishigaki, and M. Miyake, Synthetic hydroxyapatites as inorganic cation exchangers. Part 3.-Exchange characteristics of lead ions (Pb2+). Journal

of the Chemical Society, Faraday Transactions 1: Physical Chemistry in Condensed Phases, 1984. 80(11): p. 3157-3165.

41. Yasushi Takeuchi, T.S., and Hironori Arai, A study of Equilibrium and mass transfer in processes for removal of heavy-metal ions by hydroxyapatite. Journal of Chemical Engineering of Japan, 1988. 21(1): p. 98-100.

42. Tanizawa, Y., K. Sawamura, and T. Suzuki, Reaction characteristics of dental and synthetic apatites with Al3+ and La3+ ions in acidic solutions. Journal of the Chemical Society, Faraday Transactions, 1990. 86(24): p. 4025-4029.

43. Suzuki, S., et al., Cation-Exchange Characteristics of Sintered Hydroxyapatite in the Strongly Acidic Region. Journal of the American Ceramic Society, 1993. 76(6): p. 1638-1640.

44. Radtke, R.L., Strontium-calcium concentration ratios in fish otoliths as environmental indicators. Comparative Biochemistry and Physiology Part A: Physiology, 1989. 92(2): p. 189-193.

45. Dow, E.C. and J.B. Stanbury, STRONTIUM AND CALCIUM METABOLISM IN METABOLIC BONE DISEASES *. The Journal of Clinical Investigation, 1960. 39(6): p. 885-903.

46. Blake, G.M., et al., Sr-89 therapy: Strontium kinetics in disseminated carcinoma of the prostate. European Journal of Nuclear Medicine and Molecular Imaging, 1986. 12(9): p. 447-454.

47. Guo, D., et al., Development of a strontium-containing hydroxyapatite bone cement. Biomaterials, 2005. 26(19): p. 4073-4083.

48. Landi, E., et al., Sr-substituted hydroxyapatites for osteoporotic bone replacement. Acta Biomaterialia, 2007. 3(6): p. 961-969.

49. Marie, P.J., Strontium ranelate: A physiological approach for optimizing bone formation and resorption. Bone, 2006. 38(2, Supplement 1): p. 10-14.

50. Takahashi, N., et al., S 12911-2 Inhibits Osteoclastic Bone Resorption In Vitro. Journal of Bone and Mineral Research, 2003. 18(6): p. 1082-1087.

51. Baron, R. and Y. Tsouderos, In vitro effects of S12911-2 on osteoclast function and bone marrow macrophage differentiation. European Journal of Pharmacology, 2002. 450(1): p. 11-17.

52. Dahl, S.G., et al., Incorporation and distribution of strontium in bone. Bone, 2001. 28(4): p. 446-453.

53. Bonnelye, E., et al., Dual effect of strontium ranelate: Stimulation of osteoblast differentiation and inhibition of osteoclast formation and resorption in vitro. Bone, 2008. 42(1): p. 129-138.

54. Chen DM, F.Y., Evaluation on the mechanic properties of the solid solution of strontium substituted hydroxyapatite. CHINESE JOURNAL OF DENTAL MATERIALS AND DEVICES, 2001. 10(4): p. 178-183.

55. De Groot, K., et al., Plasma sprayed coatings of hydroxylapatite. Journal of Biomedical Materials Research, 1987. 21(12): p. 1375-1381.

56. Kārlis A. Gross, C.C.B., Thermal Spraying of Hydroxyapatite for Bioceramic Applications. Key Engineering Materials, 1991. 53 - 5: p. 124-129.

57. Ban, S. and S. Maruno, Hydrothermal–electrochemical deposition of hydroxyapatite. Journal of Biomedical Materials Research, 1998. 42(3): p. 387-395.

58. Zhitomirsky, I. and L. Gal-Or, Electrophoretic deposition of hydroxyapatite. Journal of Materials Science: Materials in Medicine, 1997. 8(4): p. 213-219.

59. Cotell, C.M., et al., Pulsed laser deposition of hydroxylapatite thin films on Ti-6Al-4V. Journal of Applied Biomaterials, 1992. 3(2): p. 87-93.

60. Chai, C.S. and B. Ben-Nissan, Bioactive nanocrystalline sol-gel hydroxyapatite coatings. Journal of Materials Science: Materials in Medicine, 1999. 10(8): p. 465-469.

61. Fathi, M.H. and A. Hanifi, Evaluation and characterization of nanostructure hydroxyapatite powder prepared by simple sol–gel method. Materials Letters, 2007. 61(18): p. 3978-3983.

62. van Dijk, K., et al., Influence of discharge power level on the properties of hydroxyapatite films deposited on Ti6A14V with RF magnetron sputtering. Journal of Biomedical Materials Research, 1995. 29(2): p. 269-276.

63. Lugscheider, E., et al., Production of biocompatible coatings by atmospheric plasma spraying. Materials Science and Engineering: A, 1991. 139(0): p. 45-48.

64. Gopi, D., J. Indira, and L. Kavitha, A comparative study on the direct and pulsed current electrodeposition of hydroxyapatite coatings on surgical grade stainless steel. Surface and Coatings Technology, 2012. 206(11–12): p. 2859-2869.

65. Matejicek, J. and S. Sampath, Intrinsic residual stresses in single splats produced by thermal spray processes. Acta Materialia, 2001. 49(11): p. 1993-1999.

66. Wang, Z., et al., Effects of pores and interfaces on effective properties of plasma sprayed zirconia coatings. Acta Materialia, 2003. 51(18): p. 5319-5334.

67. Mohd, S.M., M.Z. Abd, and A.N. Abd, Plasma Sprayed Hydroxyapatite Coatings: Influence of Spraying Power on Microstructure. AIP Conference Proceedings, 2010. 1217(1): p. 539-545.

68. Lu, Y.P., et al., Further studies on the effect of stand-off distance on characteristics of plasma sprayed hydroxyapatite coating. Surface and Coatings Technology, 2002. 157(2-3): p. 221-225.

69. Morks, M.F. and A. Kobayashi, Effect of gun current on the microstructure and crystallinity of plasma sprayed hydroxyapatite coatings. Applied Surface Science, 2007. 253(17): p. 7136-7142.

70. McPherson, R., N. Gane, and T.J. Bastow, Structural characterization of plasma-sprayed hydroxylapatite coatings. Journal of Materials Science: Materials in Medicine, 1995. 6(6): p. 327-334.

71. Yang, C.Y., et al., The influences of plasma spraying parameters on the characteristics of hydroxyapatite coatings: a quantitative study. Journal of Materials Science: Materials in Medicine, 1995. 6(5): p. 249-257.

72. Dyshlovenko, S., et al., Relationship between plasma spray operational parameters and microstructure of hydroxyapatite coatings and powder particles sprayed into water. Surface and Coatings Technology, 2006. 200(12-13): p. 3845-3855.

73. Sun, L., C.C. Berndt, and C.P. Grey, Phase, structural and microstructural investigations of plasma sprayed hydroxyapatite coatings. Materials Science and Engineering A, 2003. 360(1-2): p. 70-84.

74. Kweh, S.W.K., K.A. Khor, and P. Cheang, Plasma-sprayed hydroxyapatite (HA) coatings with flame-spheroidized feedstock: microstructure and mechanical properties. Biomaterials, 2000. 21(12): p. 1223-1234.

75. Tsui, Y.C., C. Doyle, and T.W. Clyne, Plasma sprayed hydroxyapatite coatings on titanium substrates Part 2: optimisation of coating properties. Biomaterials, 1998. 19(22): p. 2031-2043.

76. Tsui, Y.C., C. Doyle, and T.W. Clyne, Plasma sprayed hydroxyapatite coatings on titanium substrates Part 1: Mechanical properties and residual stress levels. Biomaterials, 1998. 19(22): p. 2015-2029.

77. Redepenning, J. and J.P. McIsaac, Electrocrystallization of brushite coatings on prosthetic alloys. Chemistry of Materials, 1990. 2(6): p. 625-627.

78. Shirkhanzadeh, M., Electrochemical preparation of bioactive calcium phosphate coatings on porous substrates by the periodic pulse technique. Journal of Materials Science Letters, 1993. 12(1): p. 16-19.

79. Wang, H., et al., Early bone apposition in vivo on plasma-sprayed and electrochemically deposited hydroxyapatite coatings on titanium alloy. Biomaterials, 2006. 27(23): p. 4192-4203.

80. Ma, M., W. Ye, and X.-X. Wang, Effect of supersaturation on the morphology of hydroxyapatite crystals deposited by electrochemical deposition on titanium. Materials Letters, 2008. 62(23): p. 3875-3877.

81. Shibli, S.M.A. and S. Mathai, The role of calcium gluconate in electrochemical activation of titanium for biomimetic coating of calcium phosphate. Journal of Biomedical Materials Research Part A, 2008. 87A(4): p. 994-1002.

82. Nancollas, G.H. and B. Tomazic, Growth of calcium phosphate on hydroxyapatite crystals. Effect of supersaturation and ionic medium. The Journal of Physical Chemistry, 1974. 78(22): p. 2218-2225.

83. Huang, L.-Y., K.-W. Xu, and J. Lu, A study of the process and kinetics of electrochemical deposition and the hydrothermal synthesis of hydroxyapatite coatings. Journal of Materials Science: Materials in Medicine, 2000. 11(11): p. 667-673.

84. Yang, X., et al., BCP coatings on pure titanium plates by CD method. Materials Science and Engineering: C, 2007. 27(4): p. 781-786.

85. Eidelman, N., L. Chow, and W. Brown, Calcium phosphate phase transformations in serum. Calcified Tissue International, 1987. 41(1): p. 18-26.

86. Wang, Y.-q., et al., HA coating on titanium with nanotubular anodized TiO2 intermediate layer via electrochemical deposition. Transactions of Nonferrous Metals Society of China, 2008. 18(3): p. 631-635.

87. Zhang, Y.-y., et al., Electrochemical deposition of hydroxyapatite coatings on titanium. Transactions of Nonferrous Metals Society of China, 2006. 16(3): p. 633-637.

88. Shirkhanzadeh, M., Direct formation of nanophase hydroxyapatite on cathodically polarized electrodes. Journal of Materials Science: Materials in Medicine, 1998. 9(2): p. 67-72.

89. Rakngarm, A. and Y. Mutoh, Electrochemical depositions of calcium phosphate film on commercial pure titanium and Ti–6Al–4V in two types of electrolyte at room temperature. Materials Science and Engineering: C, 2009. 29(1): p. 275-283.

90. Ban, S. and J. Hasegawa, Morphological regulation and crystal growth of hydrothermal-electrochemically deposited apatite. Biomaterials, 2002. 23(14): p. 2965-2972.

91. Ban, S. and S. Maruno, Morphology and microstructure of electrochemically deposited calcium phosphates in a modified simulated body fluid. Biomaterials, 1998. 19(14): p. 1245-1253.

92. Wang, S.-H., et al., Morphology of calcium phosphate coatings deposited on a Ti–6Al–4V substrate by an electrolytic method under 80 Torr. Journal of the European Ceramic Society, 2005. 25(14): p. 3287-3292.

93. Ye, W. and X.-X. Wang, Ribbon-like and rod-like hydroxyapatite crystals deposited on titanium surface with electrochemical method. Materials Letters, 2007. 61(19–20): p. 4062-4065.

94. Prado Da Silva, M.H., et al., Transformation of monetite to hydroxyapatite in bioactive coatings on titanium. Surface and Coatings Technology, 2001. 137(2–3): p. 270-276.

Fig.1-1 The structure of bone [10].

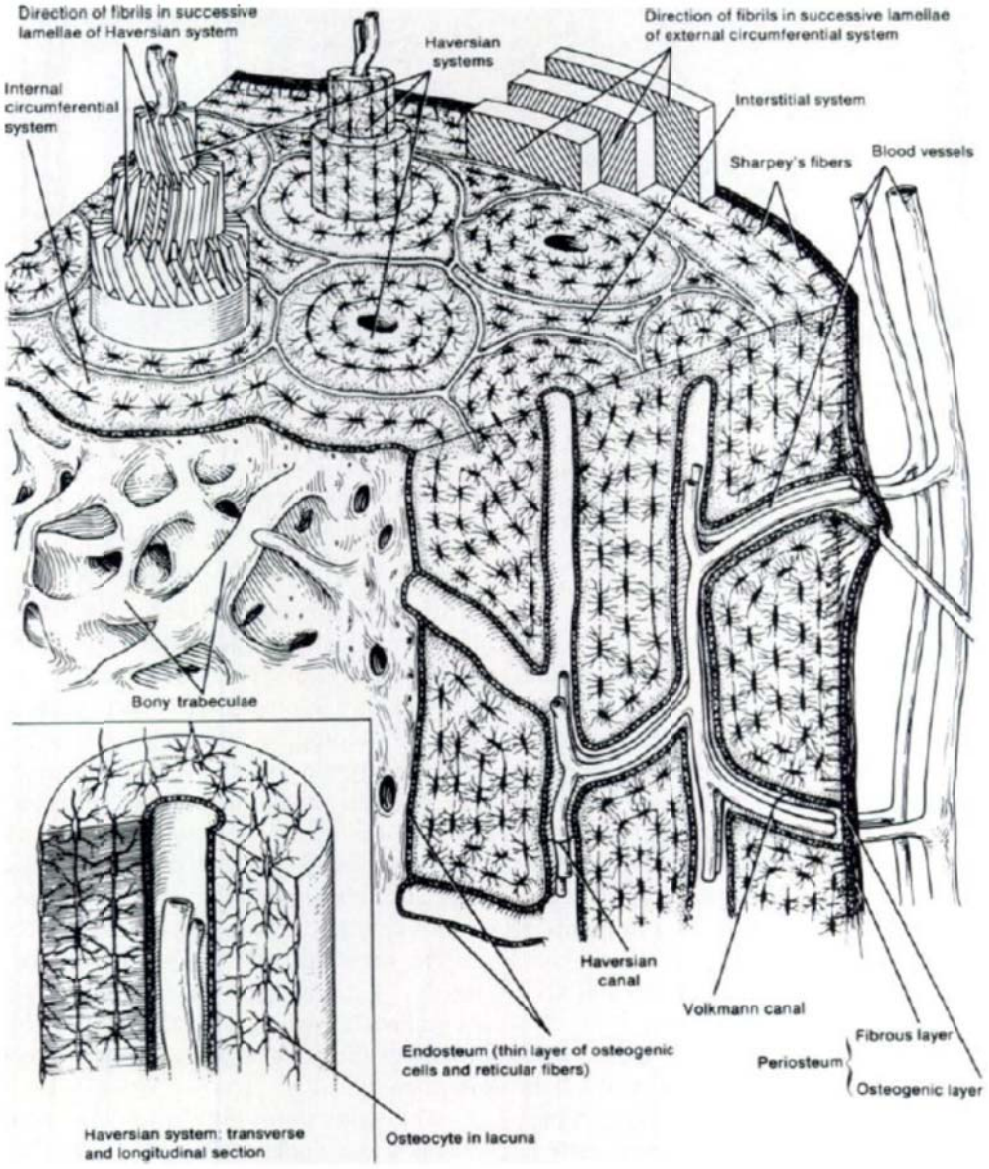

Fig.1-2 Collagen and hydroxyapatite in the bone structure [2].

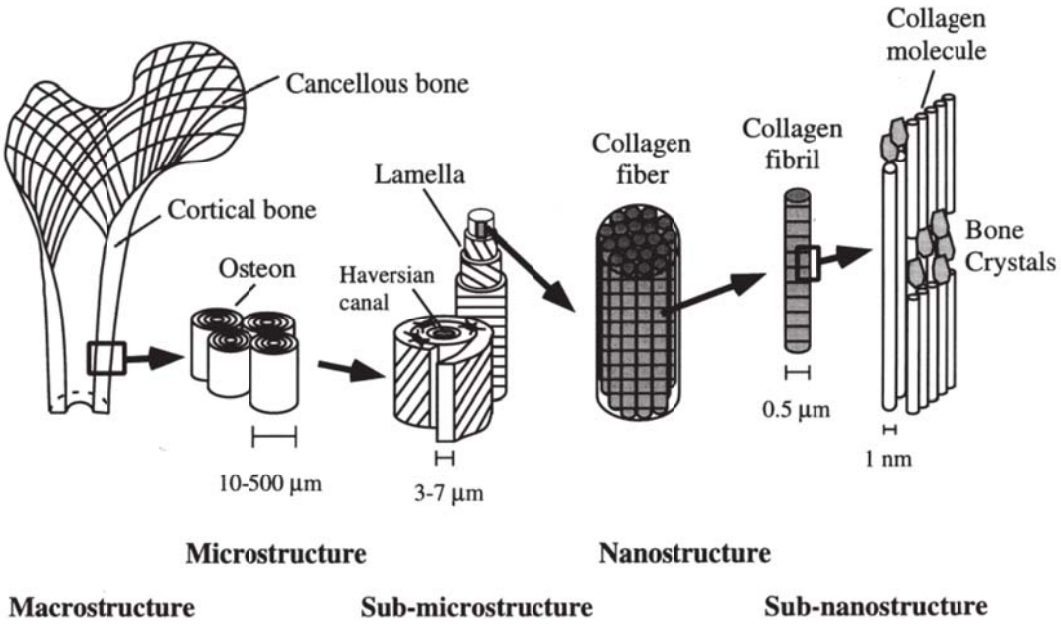
Collagen molecule
Cancellous bone
Collagen fiber
Collagen fibril
Lamella
Cortical bone
Bone Crystals
Osteon
Haversian canal
0.5 µm
1 nm
10-500 µm
3-7 µm
Microstructure
Nanostructure
Macrostructure
Sub-microstructure
Sub-nanostructure

Fig.1-3 Dual effect of Strontium: strontium can stimulate bone-forming and inhibit bone-resorbing which leads to bone gain in vivo[49].

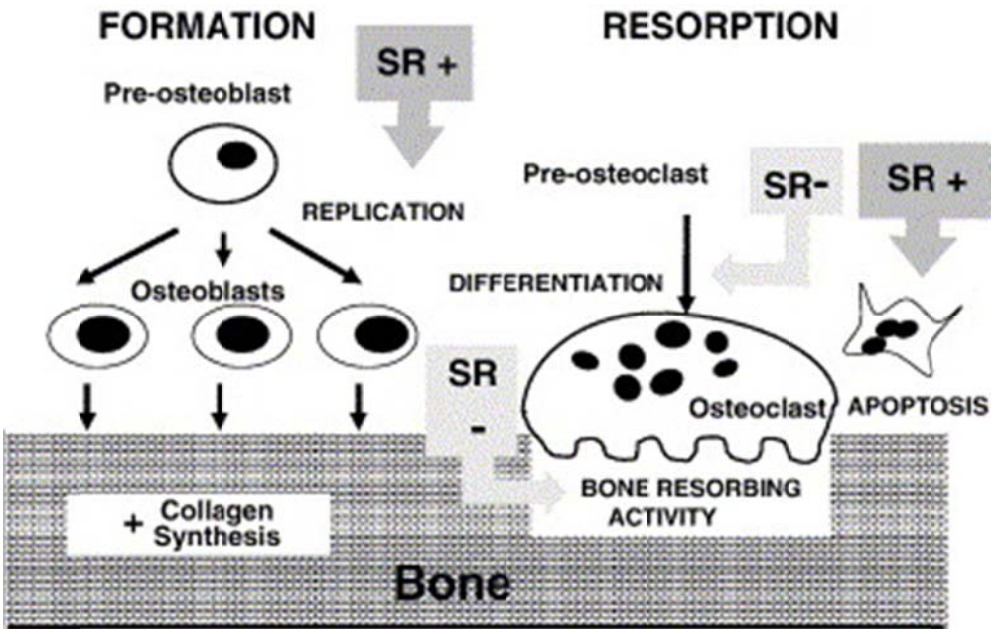

Fig.1-4 Simplified schematic diagram of plasma spray. [66]

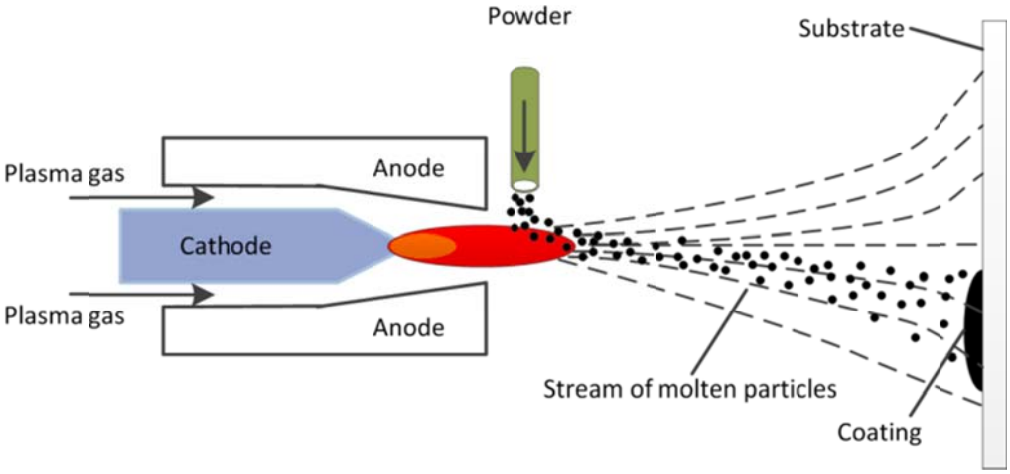

Fig.1-5 The basic experimental setup of electrochemical deposition.

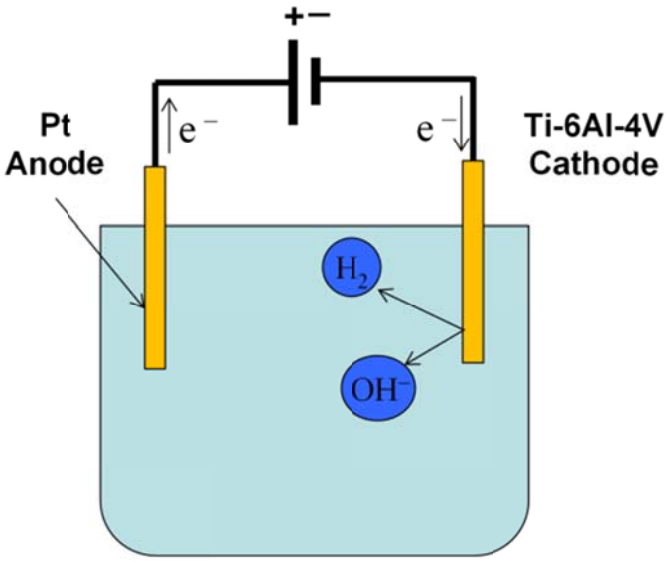

Fig.1-6 Typical microstructural features of thermal spray coating.[68]

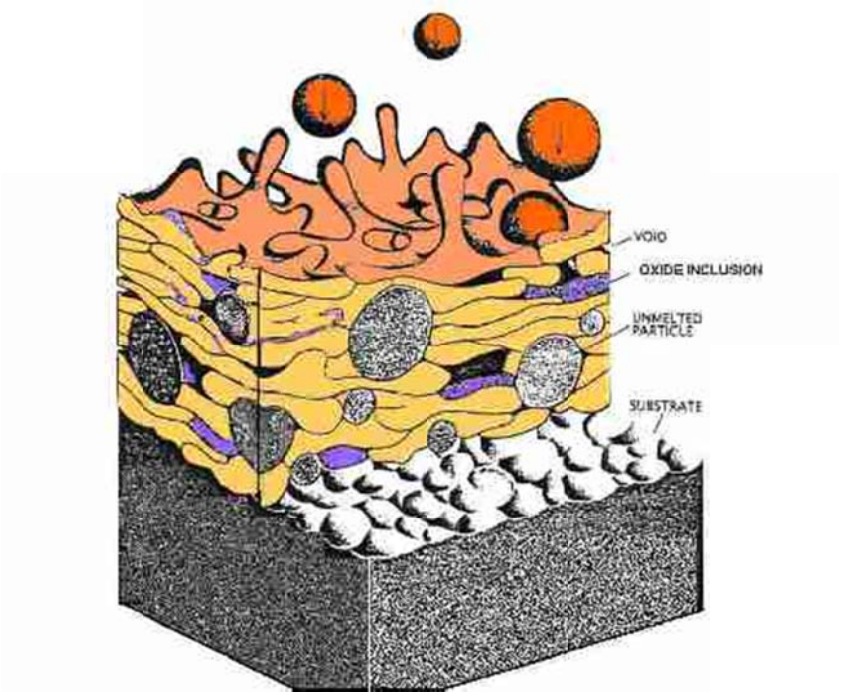

Chapter 2

MOTIVATION AND OBJECTIVES OF THE RESEARCH

2.1 Statement of the Problem

Calcium phosphate based coatings have been used to modify metal implants to obtain fast and long term stable fixture between bone and the implant. Surface reactivity is one of the most important properties for calcium phosphates, since it contributes to the bioactivity of them [1]. There are two factors controlling the surface reactivity of bioactive materials: (1) phase and chemical composition; (2) microstructure including surface morphology and porosity.

Composition and microstructure of a material can be varied by the properties of the material, process method, and process parameters. Therefore, it is crucial to investigate how they affect coating properties, and build the links between process, properties and performance. With this knowledge, through the choices of appropriate materials, process techniques and parameters, it is possible to control quality and tailor the properties of the coating to meet specific requirements of a certain case.

There are various methods to synthesize calcium phosphate based coating. Among these methods, electrochemical deposition and plasma spray are two commonly used technologies. However, due to the lack of an effective system investigation and understanding of process−property−performance in both of the technologies, controlling the properties the coatings is quite a challenge.

For electrochemical deposition, as discussed before under different combinations of process parameters such as current density, electrolyte composition and temperature, the coatings' composition and morphology can be quite different. However, since the deep-seated mechanism of the process has not been well understood, and the process parameters are interact with each other, there is not a good control over this process. As a result, the development of the electrochemical deposition has been limited, and the technology has not been widely applied, although it is a convenient and economical way to fabricate Ca-P coatings.

For air plasma spray of calcium phosphate process, as discussed in chapter 1, the system is very difficult to be controlled, due to the complexity of the process itself and the phase transformation of calcium phosphate under extremely high process

temperature. Although there are several studies conducted to link process parameters to the properties of plasma sprayed calcium phosphate coatings. However, behind those complex process parameters, the more intrinsic variable that directly affects the coatings properties is particles state, which can be quantified by temperature (T) - velocity (V) of the in-flame particles or by more comprehensive and sufficient description: melting index (MI) - kinetic energy (KE).

Plasma spray process maps were introduced by some researchers. It is a very useful tool to predict and tailor the properties of thermal spray coatings as demonstrated in literature [2-6]. It provides a graphical representation which links process parameters—> in-flame particle state—> coating property —> coating performance [5] as shown in Fig. 2-1. To our best acknowledge, there is no research yet using process map to investigate the plasma spray processing of calcium phosphate coatings. This method has latent capacity to improve the quality and control the properties of Ca-P coatings.

Furthermore, only a few studies have been published to compare calcium phosphate coatings produced by air plasma spray and electrochemical deposition. Through these two different techniques calcium phosphate coatings with distinct morphology and different phase composition can be produced. A systematically comparison study of Ca-P coatings by these two techniques can provide fresh perspective from which to understand the relationship between phase, microstructure and dissolve behaviors, as well as the underlying mechanism of the bioactive performance, therefore, it is meaningful.

Additionally, as mentioned in Chapter 1, highly crystalline stoichiometric hydroxyapatite is biocompatible and has the ability to form a biological bond with bone, however, due to its low dissolubility rate, the rate of osteoconductivity and osteoinductivity is relatively slow[7]. Therefore, developing chemically modified calcium phosphate coatings with active components incorporated to mimic the function of natural bone can be a potential solution. This type of Ca-P ceramics have improved resorbability and enhanced bioactivity compared to highly crystalline stoichiometric hydroxyapatite.

Strontium has a positive effect on enhancing bone formation and preventing undesirable bone resorption. Therefore, in this study, it has been investigated and chosen as the active component to modify calcium phosphate coatings. The influence of strontium to the microstructure and the bioactivity of strontium doped calcium phosphates will be evaluated.

2.2 Objectives of the Research

The purpose of this research is to develop biomimetic calcium phosphate coating for orthopedic and dental applications, with the objectives including:

1) Build the linkages between process parameters and deposited calcium phosphate coatings in electrochemical deposition and air plasma spray through integrated experimental studies and theoretically calculations.
2) Compare the properties including microstructure, surface morphology, chemical composition and bioactivities of strontium doped and pure calcium phosphate coatings obtained by electrochemical deposition and air plasma spry.
3) Investigate how phase composition, strontium doping and microstructure influence the bioactivity performance of calcium phosphate coatings.

The research efforts toward achieving these objectives are described in the following chapters. Chapter 3 mainly focuses on the investigation of the precipitation mechanism and impacts of process parameters on the chemical composition and morphology of the deposited Ca-P coatings in electrochemical deposition process; Chapter 4 demonstrates how to use process map as a tool to build connections between process parameters, in-flame particle state, splat characteristics and coating properties; Chapter 5 using various calcium phosphate coatings obtained by electrochemical deposition and air plasma spray, evaluates the influences of coating composition, surface morphology and the doping of strontium on the bioactivity performance of the Ca-P though in vitro cell culture test; Chapter 6 summarizes the research work in this study.

2.3 References Cited

1. Ducheyne, P. and Q. Qiu, *Bioactive ceramics: the effect of surface reactivity on bone formation and bone cell function.* Biomaterials, 1999. 20(23–24): p. 2287-2303.

2. Vaidya, A., et al., *Process maps for plasma spraying of yttria-stabilized zirconia: An integrated approach to design, optimization and reliability.* Materials Science and Engineering: A, 2008. 497(1–2): p. 239-253.

3. Friis, M. and C. Persson, *Control of thermal spray processes by means of process maps and process windows.* Journal of Thermal Spray Technology, 2003. 12(1): p. 44-52.

4. Srinivasan, V., et al., *On the reproducibility of air plasma spray process and control of particle state.* Journal of Thermal Spray Technology, 2006. 15(4): p. 739-743.

5. Vaidya, A., et al., *An integrated study of thermal spray process–structure–property correlations: A case study for plasma sprayed molybdenum coatings.* Materials Science and Engineering: A, 2005. 403(1–2): p. 191-204.

6. Sampath, S., et al., *Development of process maps for plasma spray: case study for molybdenum.* Materials Science and Engineering: A, 2003. 348(1–2): p. 54-66.

7. Klein, C.P.A.T., et al., *Biodegradation behavior of various calcium phosphate materials in bone tissue.* Journal of Biomedical Materials Research, 1983. 17(5): p. 769-784.

Fig. 2-1 Schematic overview of process maps for plasma spray[6]

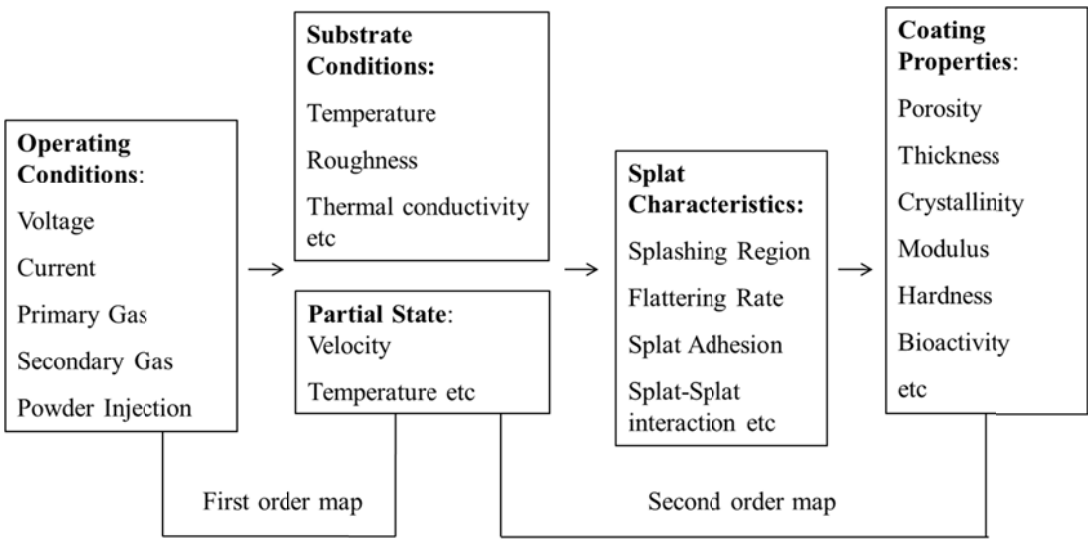

Chapter 3

ELECTROCHEMICAL DEPOSITION OF CALCIUM PHOSHPATE COATINGS

3.1 Abstract

Electrochemical deposition is a promising technology to produce calcium phosphate coatings, due to its advantages over other deposition methods as discussed before. Previous studies reported that process parameters such as current density, temperature and electrolyte have significant impacts on the coating morphology and composition in this process.

However, after review of the literature, it was found that there is almost no report on a systematic investigation of how process parameters influence electrodeposited coating properties. Therefore, controlled synthesis of calcium phosphate coatings is quite a challenge.

The purpose of this part of research is to understand how to effectively control the morphology and composition of electrodeposited coatings by manipulating the process parameters with understanding of the underlying mechanism. In this study, through a set of designed experiments and simulation, the impacts of process parameters to the coatings properties have been investigated.

3.2 Materials and Methods

The electrochemical deposition (ECD) experimental setup used here was a simple two-electrode cell configuration (Fig. 3-1). The working electrode (the coating substrate) used were commercial titanium alloy (Ti6Al4V) plates. Before coating deposition, these plates were grit-blasted using Al_2O_3, soaking in acetone ultrasonically cleaned for 10 min, after that rinsed by deionized water and then air dried. The counter electrode was a platinum mesh. The distance between the electrodes was 2 cm and the working electrode area was maintained at 0.6 cm^2.

The electrolytes were prepared by dissolving analytical grade $Ca(NO_3)_2 \cdot 4H_2O$ (Fisher Scientific, Pittsburgh, Pa), $Sr(NO_3)_2$ (Fisher Scientific, Pittsburgh, Pa) and $NH_4H_2PO_4$ (Fisher Scientific, Pittsburgh, Pa) into deionized water, with (Ca+Sr)/P molar ratio being 1.67. Both electrodes were immersed in the electrolyte where the temperature was held at specific temperature as determined by the experimental design. Electrochemical deposition was performed with a potentiostat/galvanostat instrument

(Gamry 3000). After deposition, the sample was washed in distilled water and dried at room temperature.

3.3 Pulse Current Electrochemical Deposition

During electrochemical deposition, hydrogen gas forms in the vicinity of the cathode surface as a side product. The amount of hydrogen gas produced increases with the rising of the applied current. The extensive formation of H_2 bubbles can cause a reduced amount of ions at the vicinity of substrate surface, which lead to the defects and non-uniformity in the coatings[13].

In order to solve this problem, several methods have been introduced by researchers. Szu-Hao Wang and coworkers conducted experiments to deposit calcium phosphate under 60 torr, and found that deposition under low atmospheric pressure encouraged bubble removal. Compared with coating deposited under normal atmosphere pressure, coatings obtained in this way are more integrated with improved adhesive strength. However, due to the complex experimental setup, this method faces difficulties. Another method has been proposed to perform electrochemical deposition by stirring the electrolyte[14]. However, the quality of achieved coatings produced by this method was not satisfactory.

As a promising alternative process, employing pulsed time electric fields in electrochemical deposition was introduced by several researchers. Legeros et al.[24] achieved calcium phosphate coatings with improved adhesive strength between coating and substrate on titanium alloy substrate by pulsed current electrochemical deposition. Chen et al.[25] also used this method associated with adding H_2O_2 into electrolyte to obtain uniform and adherent hydroxyapatite coatings, however, the H_2O_2's influence on coating properties was not obviously demonstrated.

Pulsed current can strongly reduce the pores caused by H_2 bubbles and increase the adhesion strength of the electrochemical deposited coating. During this procedure, the relaxation time between two deposition times (pulse cycle) is beneficial for reducing H_2 bubbles assembling and allows diffusion of ions from the electrolyte to the cathode surface.

To verify the benefit of pulsed current, both of direct and pulsed current deposition processes were employed as shown in Figure 3-2. The calcium phosphate coatings obtained under these two methods were examined and compared in order to evaluate pulsed current's effect on the quality of electrodeposited coatings.

The current density applied was set as three different levels: 5, 10 or 15 mA/cm^2. For direct current deposition, the current was constant during the whole process, as indicated in Fig 3-2(a). For pulsed current deposition, as shown in Fig 3-2(b), one cycle consisted of 1 min with current on, and followed by 1 min with current off to allow releasing of the bubbles. In each of the conditions, 5~20 pulse-cycles were used during deposition, which corresponds to a total deposition time of 5~20 min. A different number of the cycles were used for different current density in order to obtain similarly deposited masses under different current densities. After deposition, specimens were removed from the electrolyte and rinsed with distilled water and then dried off at 40 °C for 4 h. Different conditions were used as indicated in Table. 3-1.

Table. 3-1 The different conditions used to compare direct and pulsed current deposition

Sample ID	Current Density (mA/cm^2)	Pulsed Current
C1	5	Y
C2	10	Y
C3	15	Y
C4	5	N
C5	10	N
C6	15	N

The surface morphologies of the coatings deposited under those conditions were investigated, and are shown in Fig. 3-3 and Fig. 3-4. Under low current density (5 mA/cm^2) both of the direct current and pulsed current deposited coatings with reasonable adhesion to the substrate as assessed through qualitative scratching of the coatings with a metallic probe. However, when current density increased, under the direct current, the

deposited coatings were deficient and flakes off especially. The SEM morphology of coating synthesized under direct current of 10 mA/cm^2 is shown in Fig. 3-4(C), as can be seem in the figure, the obtained coating is inhomogeneous and has a highly porous structure. This structure results from bubbles gathering at the cathode surface, preventing the deposition of calcium phosphate on the substrate. When the current density was increased to 15 mA/cm^2, minimal coating was deposited by direct current. Under high current density, the deposited coating was peeled away from the surface by even faster assembling of bubbles, leaving coating thin, porous coating (as shown in Fig. 3-3 as C6 sample). Instead, as indicated in Fig. 3-4 (a) and (b), by using pulsed deposition, accumulation of H_2 bubbles on the surface were remarkable reduced (although they could not be fully removed) and deposited coatings were more regular and integrated. Here the benefit of applying pulse current in electrochemical deposition has been demonstrated. Therefore, calcium phosphate coatings were prepared by pulsed electrochemical deposition current for the remainder of the study.

3.4 Morphology and crystallite size of the electrochemical deposited coatings

In the electrochemical deposition process, various coating morphologies can be obtained by changing process parameters and dose of strontium.

Fig. 3-5 shows the SEM images of as deposited pure calcium phosphate (0% Sr doped) coatings prepared using different levels of current density: 5, 10 and 20 mA/cm². It can be seen from Fig. 3-5 (a) and (b) that under relative low current density: 5mA/cm^2 and 10mA/cm^2, undoped Ca-P coatings had the morphology of a mixture of needle-like and faceted structures.

When current density became higher, the morphology of coating experienced a conversation: the amount of faceted crystallite decreased while needle-shape crystals increased. Faceted-crystallites become smaller and even disappeared when current density reached 20 mA/cm^2 (Fig. 3-5(c)). At this high current level, the needle-shape crystals became the dominant phase throughout the coatings obtained.

The concentration and temperature of electrolyte also had a significant influence on the deposited coatings. From Fig. 3-6, it is clearly shown that coating morphology changes under various concentrations of electrolyte and temperature.

In this study, the concentration of Ca^{2+} in the electrolyte was set at four different levels: 0.084 mol/L, 0.042 mol/L and 0.021 mol/L, while (Ca+Sr)/P molar ratio was maintained at 1.67. From the results of the experiments, needle-shape crystals tended to be synthesized in diluted electrolyte, while high concentration of the electrolyte was beneficial for the formation of faceted-crystallites. When concentration of Ca^{2+} in the electrolyte reached 0.084 mol/L, faceted-crystallites became the dominant phase throughout the coatings.

The impact of the temperature on coating morphologies was investigated by comparing coatings deposited at different temperature (70 ºC and 90 ºC). From the result it was found that, with the increase of temperature, for coatings with faceted-crystallites as dominated phase (Figs. 3-6 (a) and 3-6 (d)), the number of the rock-like crystals increased, while the size of the crystals became smaller. For coatings with needle-like crystal structure (Figs. 3-6(b), (c) and 3-6(e), (f)), crystal's length and diameters increased with the increase of the temperature.

The doping of strontium also changed the coating morphology. By comparing the undoped coatings (Fig. 3-7 (a), (d)), 5% Sr-doped coatings (Fig. 3-7 (b), (e)) and 10% Sr-doped ones (Fig. 3-7 (c), (f)), it can be observed that with the increase dose of strontium in the electrolyte, the crystal size decreased and the number of crystals (either needle-like crystals or faceted crystals) tended to increase.

3.5 Chemical Composition and Phase Identification of the Coatings

The process parameters not only impacted the coating morphology, they also had dramatic influence on the phase compositions of the coatings. Fig. 3-8 shows the X-ray diffraction patterns of the coatings deposited under different current density. As can be seem in the figure, coating composition changed with the change of current density.

ECD coatings contained different Ca-P phases such as monetite (dicalcium phosphate, $CaHPO_4$) (cross) and hydroxyapatite (HA, $Ca_5 (PO_4)_3OH$) (filled triangle

symbol). For samples deposited under low current density, the peaks from monetite became stronger, while the peaks from hydroxyapatite became weaker. Therefore, the faceted crystals found in the ECD coatings which were prepared under low current density (Fig. 3-5 (a), (b)) were most likely monetite, while the needle-like crystals in Fig. 3-5 (c) were likely to be HA. Deposited HA had preferred orientation. HA has a hexagonal structure, the [002] plane is the most densely plane-packed, thus usually [002] is the preferred growth direction, which was confirmed by the SEM morphology study, where oriented growth of needle-like crystal was found.

Additionally, intense peaks from titanium (filled star symbol) can be observed in all patterns, because the coatings were thin and porous. In thin coatings, peaks of Al_2O_3 (filled square symbol) can also be found due to residue of alumina during grit-blasting process. The X-ray diffraction spectra indicate that different phases can be found in electrodeposited coatings.

Under the same level of current density, different combinations of temperature and electrolyte concentration can yield coatings with different phase composition. Fig. 3-9 shows the coatings' phase composition under 70 and 90 ºC, three different levels of electrolyte concentration. As can be seem in the figure, under 70 ºC, in dilute electrolyte (0.042 mol/L and 0.021 mol/L), the final product only contains HA, while in high concentration electrolyte (0.084 mol/L), monetite and brushite (both of them are DCPD) become part of coating composition. In high temperature, brushite can't form in high concentration electrolyte, but can be produced in dilute solution.

The influence of strontium on the coating composition was also investigated. The XRD patterns of calcium phosphates with different doping level of strontium are shown in Fig. 3-10. Usually, doping of strontium into Ca-P ceramics causes the shift of XRD pattern to the lower Bragg angles range. However, in the present study, strontium did not seem to have a significant impact on the crystal structure of as deposited coatings, which is probably attributed to the relatively low dose.

3.6 Analysis of the Mechanism during Electrochemical Deposition

Like most crystallization process, during electrochemical deposition, the precipitation of calcium phosphate contains three steps: formation of supersaturation, nucleation and growth the crystals. [6] [15]

3.6.1 Thermodynamic Analysis: Formation of Supersaturation

The formation of supersaturation is the first and critical step for the process.

The supersaturation index (SI) of a certain phase in a solution which can be express as follow:

$$SI = log_{10}(\frac{IAP}{K_{sp}}) \tag{3-1}$$

Here, IAP is the ion activity product and K_{sp} is the thermodynamic solubility product of the phase.

From thermodynamic view, the Gibbs free energy change (ΔG) is the driving force for a reaction, which is defined as:

$$\Delta G = -RTln\,(\frac{IAP}{K_{sp}})/\mathrm{n} \tag{3-2}$$

$$\Delta G = -2.203RTSI/\mathrm{n} \tag{3-3}$$

Here, T is the absolute temperature, which has the unit K, R is the gas constant (R = 8.314J/ (mol·K)), n is the number of ion units in the product's molecule, which is defined in reaction equations[16].

When SI > 0 which indicates the solution reaches supersaturation, from equation (3-3), at this moment ΔG < 0, therefore, the corresponding reaction will be trigged. When SI < 0, ΔG > 0, the solution is still undersaturation, the reaction cannot happen. While SI = 0, ΔG, the solution is saturated, the reaction reach its equilibrium status, and the reaction is reversible.

When a certain phase's ionic activity product (IAP) becomes higher than its solubility product (Ksp), SI > 0, the thermodynamic requirement is satisfied, and this phase will precipitate.

In this study, as mentioned in Section 3.2, the electrolytes were prepared by dissolving $Ca(NO_3)_2 \cdot 4H_2O$, $Sr(NO_3)_2$ and $NH_4H_2PO_4$ into deionized water. Therefore, it contains Ca^{2+}, Sr^{2+} and $H_2PO_4^-$. $H_2PO_4^-$ ion is stepwise dissociated in the water. There are three equilibrium reactions for phosphate ions as following[16]:

$$H_2PO_4^- \leftrightarrow HPO_4^{2-} + H^+ \qquad \log_{10}K_1 = 5.3541 - 0.01984T - 1979.5/T \tag{3-4}$$

$$HPO_4^{2-} \leftrightarrow PO_4^{3-} + H^+$$

$$\log_{10}K_2 = -76.17 - 0.033574T - 134.05/T + 29.658\log_{10}T \tag{3-5}$$

$$H_3PO_4 \leftrightarrow H_2PO_4^- + H^+ \qquad \log_{10}K_3 = 4.5535 - 0.01349T - 799.3/T \tag{3-6}$$

While the equilibrium of water can be expressed by[16]:

$$H_2O \leftrightarrow OH^- + H^+$$

$$\log_{10}K_3 = 22.801 - 0.010365T - 4787.3/T - 7.1321\log_{10}T \tag{3-7}$$

The increase of pH will move these reactions to the right side, due to the reaction of hydroxyl ions with hydrogen ions. Therefore, the overall reactions can be seemed as:

$$H_2PO_4^- + OH^- \rightarrow HPO_4^{2-} + H_2O \tag{3-8}$$

$$HPO_4^{2-} + OH^- \rightarrow PO_4^{3-} + H_2O \tag{3-9}$$

$$H_3OP_4 + OH^- \rightarrow H_2PO_4^{3-} + H_2O \tag{3-10}$$

So that various phosphate species may coexist in the electrolyte solution, such as $H_2PO_4^-$, $HPO4^{2-}$ and $PO4^{3-}$, the concentrations of these ions depend on the pH value of the electrolyte. In this study, the specie curve was generated by scientific software CHEMEQL, which has the ability to calculate the distribution of various phosphate species within certain pH range. The simulation result was shown in Fig. 3-11.

This figure shows that the composition of the phosphate species in the solution is pH dependent. H_3PO_4 is a possible phase under extremely low pH environment (below 2). When pH around 2 to 7, the $H_2PO_4^-$ ion is more stable and therefore is the most abundant specie. When pH increases further, HPO_4^{2-} is the majority specie. In high pH solution above 12 the dominate specie become PO_4^{3-}.

Electrochemical deposition is based on the concentration change of hydroxyl and phosphate ions due to the pH change of electrolyte solution in the applied electric field. During electrochemical deposition, before voltage was applied, the pH value of the bulk solution of electrolyte is around 4.7, therefore, although $H_2PO_4^-$ and $HPO4^{2-}$ coexist in the solution system, the amount of HPO_4^{2-} is small, and the amount of PO_4^{3-} is negligible. No precipitation of calcium phosphates will happen in this step.

When voltage is applied, the electric current passes though the cell which provides electrons on the surface of substrate (cathode). Thus the water in the electrolyte gets reduced in this area, producing both hydrogen gas and hydroxyl ions, as expressed by the Equation (3-11).

$$2H_2O + 2e^- \rightarrow H_2 \uparrow + 2OH^- \tag{3-11}$$

As produced OH^- ions rapidly diffuse from the surface of the cathode to nearby area, the pH of the electrolyte is raised locally, as shown in Fig. 3-12. And since the vicinity of the cathode surface has different ion concentration compared to bulk electrolyte, it has extensive ion exchange with the bulk electrolyte by diffusion, therefore this area is usually called the diffusion layer[17, 18].

Chen et al. used basic diffusion principles to calculate distribution of OH^- in the electrolyte[20]. In the work, Fick's second law was used, which descripts how diffusion causes the change of concentration with time:

$$\frac{\partial C_{(x,t)}}{\partial t} = D\frac{\partial^2 \mathrm{C_{(x,t)}}}{\partial \mathrm{x}^2} \tag{3-12}$$

Before current is applied, the pH of the electrolyte is constant. The relationship of pH and concentration of OH^- group can be expressed as:

$$pH = logC_{(x,t)} + 14 \tag{3-13}$$

Therefore, at this time, the distribution of OH^- is homogeneous through the solution and its concentration can be calculated. The initial condition is:

$$C(x,0) = C_0 \tag{3-14}$$

On the surface of the substrate:

$$\left(\frac{\partial C}{\partial x}\right)_{x=0} = -\frac{I_0}{nFDS} = constant \tag{3-15}$$

And for the points that is infinitely far away from the electrode:

$$C(\infty,t) = C_0 \tag{3-16}$$

The solution of the equations is:

$$C_{(x,t)} = C_0 + \frac{2i_0\sqrt{\pi Dt}}{n\pi FD}\exp\left(-\frac{x^2}{4Dt}\right) - \frac{i_0 x}{nFD}\left[1 - \mathrm{erf}\left(\frac{x}{2\sqrt{Dt}}\right)\right] \tag{3-17}$$

Therefore at time t, the pH value of a point which has a distance of x cm from the surface of cathode can be expressed by:

$$pH_{(x,t)} = \log\{10^{(pH_0-14)} + \frac{2i_0\sqrt{\pi Dt}}{n\pi FD}\exp\left(-\frac{x^2}{4Dt}\right) - \frac{i_0 x}{nFD}\left[1 - \mathrm{erf}\left(\frac{x}{2\sqrt{Dt}}\right)\right]\} + 14 \tag{3-18}$$

pH_0: The original pH value of the electrolyte solution before current applied;

i_0: Applied current density, with the unit mA/ cm^2;

D: The diffusion coefficient of OH−, which is 5.28 × 10-5cm^2/s;

t: Time, with the unit s;

x; Distance from the cathode, with the unit cm;

F: Faraday constant, which is 96 485.3415 s A / mol.

The calculation result is shown in Fig. 3-13 which clearly confirms the existence of a diffusion layer within the distance less than about 0.5 cm from the cathode as can be seem from Fig. 3-12 (a). It can also be observed that increased current density will increase the amount of OH^-, so the pH value of the electrolyte solution will become higher.

With the accumulation of OH^- ions and increase of pH in diffusion layer due to the applied current, the concentration of HPO_4^{2-} and PO_4^{3-} will also rise which has been discussed before. Phosphate ions HPO_4^{2-} and PO_4^{3-} produced during the process can react with Ca^{2+} and OH^-, as several references mentioned [15, 16], the possible reactions including:

$$Ca^{2+} + HPO_4^{2-} + 2H_2O \rightarrow CaHPO_4 \cdot 2H_2O\ (DCPD)\downarrow \quad (3\text{-}19)$$

$$4Ca^{2+} + HPO_4^{2-} + 2PO_4^{2-} + 2.5H_2O \rightarrow Ca_4H(PO_4)_3 \cdot 2.5H_2O\ (OCP)\downarrow \quad (3\text{-}20)$$

$$\text{And} \qquad 5Ca^{2+} + 3PO_4^{2-} + OH^- \rightarrow Ca_5(PO_4)_3OH\downarrow \text{ (HA)} \quad (3\text{-}21)$$

As can be seen in these reactions, the possible products can be dibasic calcium phosphate dihydrate (DCPD, $CaHPO_4 \cdot 2H_2O$), octacalcium phosphate (OCP) or hydroxyapatite (HA ,$Ca_{10}(PO_4)_6(OH)_2$). Thus compositions of the deposited Ca-P coatings are varied depending on which reactions happen during the deposition process. The corresponding ion activity product (IAP) of HA and DCPD are expressed by activities of different ions as:

$$IAP_{HA} = A(Ca^{2+})^5 A(PO_4^{3-})^3 A(OH^-) \quad (3\text{-}22)$$

$$IAP_{DCPD} = A(Ca^{2+}) A(HPO_4^{2-}) \quad (3\text{-}23)$$

$$IAP_{OCP} = A(Ca^{2+})^4 A(PO_4^{3-})^3 A(H^+) \quad (3\text{-}24)$$

Thermodynamic solubility product K_{sp} is temperature dependent, by references [15, 21-23], the K_{sp} of HA, DCPD and OCP can be expressed by:

$$log_{10}K_{sp}(HA) = -1.6657 - 0.098215T - 8219.41/T \quad (3\text{-}25)$$

$$log_{10}K_{sp}(DCPD) = 18.180752 - 0.0420307T - 3649.5701/T \quad (3\text{-}26)$$

$$\log_{10}\mathrm{K_{sp}(OCP)} = 1039082.71 + 196.004417\mathrm{T} - \frac{48333918.7}{\mathrm{T}} - 388521.579\log\mathrm{T} + 2303600498/\mathrm{T}^2 \quad (3\text{-}27)$$

In order to evaluate the precipitation behavior of different calcium phosphate phases, PHREEQC was used to calculate the SI of each phase under different pH value. In the calculation, besides the equations and thermodynamic data from (3-4) ~ (3-10) and (3-19) ~ (3-27), data on the equilibrium of several ion pairs should also be used in the calculation, including[24]:

$$Ca^{2+}+H_2PO_4^{-}\rightarrow CaH_2PO_4^{+} \quad \log Ksp = 57.1388-0.09592T- 8232.51/T \tag{3-28}$$

$$Ca^{2+}+HPO_4^{2-}\rightarrow CaHPO_4 \quad \log Ksp = -81.1027+0.14275T+12213.79/T \tag{3-29}$$

$$Ca^{2+}+PO_4^{3-}\rightarrow CaPO_4^{-} \quad \log Ksp = 6.4624 \tag{3-30}$$

$$Ca^{2+}+OH^{-}\rightarrow CaOH^{+} \quad \log Ksp = 1.3010 \tag{3-31}$$

$$NH_4^{+} = NH_3 + H^{+} \quad \log Ksp= 0.6322 – 0.00123T – 2835.8/T \tag{3-32}$$

3.6.2 Thermokinetic Analysis: Nucleation and Crystal Growth

In thermodynamic analysis, through calculating of SI and ΔG, one can determine whether a reaction will happen or not. However it also has some limitations such as it cannot provide the information regarding the kinetics of the reactions and the nucleation rate. Therefore, a thermokinetic model should be built to investigate the nucleation behavior during electrochemical deposition process.

There are two types of nucleation: homogenous nucleation and heterogeneous nucleation. When nucleation occurs without preferential sites, it is called homogenous nucleation. Homogenous nucleation happens spontaneously and randomly. Heterogeneous nucleation occurs at preferential sites such as phase boundaries or impurities. The wetting between new phase and preferential site provides contact angle θ greater than zero which reduce the energy need to form nuclear. The energy needed for heterogeneous nucleation is equal to the product of the contact angle function and homogeneous nucleation[25]:

$$\Delta E_{heterogeneous} = f(\theta) * \Delta E_{homogeneous} \tag{3-33}$$

$f(\theta)$: the contact angle function is defined as follow[26]:

$$f(\theta) = \left[\frac{(2+\cos\theta)(1-\cos\theta)^2}{4}\right] \quad (3\text{-}34)$$

Therefore, heterogeneous nucleation usually happens easier than homogeneous nucleation.

In electrochemical deposition, both of the two types of nucleation can be involved. When the nucleation of calcium phosphate crystals happens on preferential sites provided by the substrate surface, it should be considered as a heterogeneous process. However, when the surrounding electrolyte reaches critical superstation point of certain phase, homogeneous nucleation of that phase can also occur in the electrolyte.

The nucleation rate (J) should be expressed as [20, 26]:

$$J = K_1 \cdot P \cdot \exp\left(-\frac{\Delta E}{kT}\right) \quad (3\text{-}35)$$

For homogenous nucleation:

$$J_1 = K_1 \cdot P \cdot \exp\left(-\frac{16\pi v^2 r^3}{3k^3T^3(lnS)^2}\right) \quad (3\text{-}36)$$

For heterogeneous nucleation:

$$J_2 = K_1 \cdot P \cdot \exp\left(-\frac{16\pi v^2 r^3 f(\theta)}{3k^3T^3(lnS)^2}\right) \quad (3\text{-}37)$$

K_1: constant, which is 13.64×10^{24}cm $^{-3}$S^{-1} [26];

P: the probability that appropriate ions meet to form a nuclear of a certain phase, which can be calculated using the activities (A) of ions of HA, DCPD and OCP

$$P_{HA} = \frac{9!A(Ca^{2+})^5A(PO_4^{3-})^3A(OH^-)}{5!3![A(Ca^{2+})+A(OH^-)+A(PO_4^{3-})]^9} \quad (3\text{-}38)$$

$$P_{DCPD} = \frac{2!A(Ca^{2+})A(HPO_4^{2-})}{[A(Ca^{2+})+A(HPO_4^{2-})]^2} \quad (3\text{-}39)$$

$$P_{OCP} = \frac{7!A(Ca^{2+})^4 A(PO_4^{3-})^2 A(HPO_4^{2-})}{4!2![A(Ca^{2+}) + A(HPO_4^{2-}) + A(PO_4^{3-})]^7} \quad (3\text{-}40)$$

v: the volume of primitive crystal cell, v_{HA} =263.24 $\dot{A}^3$ v_{DCPD} =126.54 $\dot{A}^3$, v_{OCP} =310.59 $\dot{A}^3$ based on the study by Chen et al. [26] ;

γ: the interfacial energy, γ_{HA} =10.4 mJ/m^2, γ_{DCPD} =0.4 mJ/m^2, γ_{OCP} =4.3 mJ/m^2 according to the study by Wu et al.[27, 28];

$f(\theta)$: the contact angle function, which is defined in (3-27);

The study of Lu indicated that, it doesn't have significant influence on the nucleation thus here, $\theta = 90$ is set, $f(\theta)$ = 0.5[20].

k: Boltzmann constant, which is 1.38 ×10^{-23} JK^{-1};

T: absolute temperature, with the unit K.

S: supersaturation is defined as:

$$S = \frac{IAP}{K_{sp}} \quad (3\text{-}41)$$

Through calculation, it can be observed that the value of the term $-\frac{16\pi v^2 r^3}{3k^3T^3(lnS)^2}$ for these three types of calcium phosphates is close to zero, therefore, the homogenous nucleation rate and heterogeneous nucleation rate should be very similar. $J_1 \approx J_2 \approx K_1 \cdot P = J$. Therefore, in the following discussion, homogenous and heterogeneous nucleation rates won't be discriminated.

After calcium phosphate nuclei form, they begin to grow into the surrounding electrolyte solution through transfer of appropriate atoms from the electrolyte solution across the moving interface. In the electrolyte, the product's composition is different from the mother phase (electrolyte), and the growth is controlled by how fast certain atoms can diffuse away or towards the interface. Therefore the crystal growth process in electrochemical deposition is diffuse controlled [19, 29, 30].

3.7 The Influences of Process Parameters on the Coating Properties

3.7.1 The Influence of pH Value and Current Density

As discussed previously, the pH value of the solution controls the distribution of ions, thus it should have dramatic influences on the precipitation behavior of calcium phosphates and the final coating's composition in electrochemical deposition process. From Fig. 3-14(a), it can be clear seem that with the increase of pH, the activity of OH^- and $PO4^{3-}$ increase, while the activity of Ca^{2+} decrease. The activity of $HPO4^{2-}$ reach its peak around pH = 7.

According to the definition of ionic activity product (IAP) and supersaturation indexes (SI), when the activity of ions change, the IAP and SI of the phases will also change. Therefore, the SI of DCPD, HA and OCP are also pH dependent. For example, when the electrolyte containing 42 mM Ca^{2+}, with Ca:P ratio equals to1.67, at 90ºC, as shown in Fig. 3-14, with the increase of pH value, SI of HA increase, for DCPD and OCP, the value of SI first increase and then decrease in high pH range.

It can also be observed that when pH > 3.5, HA always has SI >0 which means the precipitation of HA tends to happen in high pH range. The solution's pH is within the 4 ~ 10.5, DCPD's SI is above 0, and therefore it is expected to precipitate in the range. OCP's supersaturation index SI < 0 over the whole pH range from 1 to 14, which means under this condition, OCP is not a possible phase.

Fig. 3-14(c) shows the result of kinetic calculation result using equations from (3-33) ~ (3-41). From result, it is very clear that the nucleation rate of DCPD is high than HA and OCP, especially under low pH, which indicates that DCPD is more thermodynamic favorite phase compared to the other two phases. With the increase of pH value, the nucleation rates of DCPD and HA first increase then decrease mainly due to the ion concentration change especially the dramatic decreased amount of the Ca^{2+} in the electrolyte.

The increase of current density in electrochemical deposition is directly related to the increase of pH value of the electrolyte solutions due to increased OH^- production.

The influence of current density on the precipitation behaviors of calcium phosphates should be similar to the impact of pH. Generally speaking, the increase of current density will benefit the formation of HA (hydroxyapatite), and DCPD (dicalcium phosphate dehydrate) tends to be produced under low current density. However, it is worth to point that that, the pH rises due to the current density is localized in diffusion layer with a gradient, unlike the pH change of the electrolyte which has a homogenous change in the whole electrolyte solution.

3.7.2 The Influence of Concentration of the Solutions

Electrolyte concentration has significant influence on the precipitation behavior of calcium phosphates. As Fig. 3-15(a) shows, increasing electrolyte concentration means increase the amount of Ca^{2+}, HPO_4^{2-}, PO_4^{3-} ions, thus the supersatureation index of each phases will increase. Therefore high concentration benefits for the deposition of calcium phosphates. Although increased concentration rise the values of SI of calcium phospahtes slowly as shown in Fig.3-15(b), it significantly broadens the pH range for calcium phosphate to precipitate. Especially for DCPD, as shown in Fig. 3-16(b), at 90 ºC, in electrolyte containing 10.5mM Ca^{2+}, DCPD can only be deposited from pH = 5 to 9. As can be seen in Fig 3-13(a), the reaction will happen in a limited area. However when electrolyte's concentration increased to 168 mM Ca^{2+}, the pH range for DCPD precipitation becomes to pH = 3 to 11. Since the original pH value of electrolyte is 4.7, which means the precipitate of DCPD can happen in the whole electrolyte solution. The pH range for precipitate of HA also increase during the electrolyte concentration change, HA can only be deposited when pH above 4, when electrolyte concentration is 10.5mM, but when concentration increases to 169mM, pH = 3 becomes the threshold. For OCP, although the SI curve moves up when concentration increases, the whole curve still below zero, so there will not be any precipitation happens under this condition.

Ion concentration doesn't have significant impact on the nucleation rate of those phases as shown in Fig. 3-15(C). And in all concentration range, the nucleation rate (J) of DCPD is much higher than the other two phases, so once the precipitation of DCPD happens, DCPD will become predominate phase. As Therefore, in high concentration

electrolyte, when DCPD has more precipitate area in the electrolyte solution, it will become the majority composition in the coating.

Additionally, high electrolyte concentration benefits the growth of the crystals, due to the sufficient ion supplies for the growing crystal in the interface. That is why the crystals have a larger size when they are obtained in high concentration electrolyte, which correlates with the experimental result shown in Fig. 3-6 and 3-7.

3.7.3 The Influence of Electrolyte Temperature

As discussed before, SI is controlled by two factors solubility product (Ksp) and ion activity product (IAP).

As mentioned before, thermodynamic solubility product Ksp is temperature dependent. Fig.3-17 shows the influence of temperature to the solubility products of HA, OCP and DCPD. According to this figure, For HA and OCP, when temperature increase from 0 to around 20 degree C, the solubility products increase a little bit, then with further increase of the temperature, the solubility products decrease dramatically. For DCPD, with the increase of temperature, the solubility product remains almost unchanged until around 50 degree C, after that, solubility product increase remarkably.

The activities of ions are also influenced by temperature. As can be seen in Fig.3-18, when temperature increase, the activity of OH^- increases, while activities of Ca^{2+}, HPO_4^{2-} and PO_4^{3-} decrease.

Therefore, the electrolyte's temperature impacts the formation of the three types of calcium phosphates. Fig. 3-19 shows the supersturation index of HA, OCP and DCPD under 90 ºC, 70 ºC and 25 ºC. As can be seen in this figure, temperature doesn't have much impact on the SI of HA, but it has dramatic influence on OCP. With the increase of temperatue, the SI of OCP decreases. When temperature rise to 90 ºC, the SI of OCP is below zero in the whole pH range (pH = 1 to 14), which means OCP is not a possible phase under this temperature. Temperature also affect the SI of DCPD in certain pH range (pH = 5 to 10). However, since the zero point of SI didn't change a lot under different temperature, which means temperature won't change the supersaturation forming behavior of DCPD a lot.

Temperature also has a significant influence on the nucleation rate of calcium phosphates in certain pH ranges as shown in Fig. 3-20. For HA, when pH is below 10,nucleation rate slowly increase with the increase of temperature, but dramatically decreases with the increase of temperature under the pH above 10. For DCPD, in the pH range 4 to 11, where DCPD is a possible phase (SI above zero), the nucleation rate is lower in high temperature than in low temperature. Temperature may not have dramatic impact on the nucleation of OCP, when pH is below 11; in high pH range above 11, on one hand, increasing temperature benefits the nucleation of OCP, but on the other hand, high temperature may stop the formation of OCP, due to the decrease of OCP's SI.

3.8 Verification of the Model

In order to verify the models developed in this study, theoretical calculation were compared with the experimental results. When the current density is applied, as it was discussed before, at certain temperature, the pH distribution in the electrolyte is the function of time, current density applied and distance from the cathode.

When the electrolyte containing 42 mM Ca^{2+}, with Ca:P ratio equals to 1.67, at 90ºC, as calculated before, when electrolyte pH value higher than 10.5, DCPD has SI below zero, while HA's SI is above zero, thus the HA will become the dominant phase in the coating. Therefore, pH = 10.5 is the threshold of DCPD formation under this condition. Fig. 3-21 shows the impacts of current density on the formation of the DCPD. The curve in this figure represents the combinations of current density, distance and time to obtain pH = 10.5 in the electrolyte.

In this figure, the area below each curve is the time-distance range, where pH of electrolyte below 10.7 under certain current density, and DCPD will be produced. It can be observed that with the increase of current density, the curve moves down, which indicate that less DCPD will be produced, which confirms the experimental findings as shown in Fig. 3-5 and Fig. 3-8. Therefore, the model is considered to be reasonable and effective.

3.9 The Influence of Strontium

The doped calcium phosphates have complex structures, and it is difficult to build the theomodynamic and thermokinetic models for them due to the lack of thermodynamic data of them. However, from the experiment results, the doping of strontium has the effect of reducing crystal size, as shown in Fig. 3-7. And since the atom size of strontium is larger than that of calcium, the doping of strontium into calcium phosphate will cause the expansion of crystal lattice of calcium phosphates. It means more energy is required to form Sr-doped calcium phosphates than those pure ones, therefore the incorporation of strontium in calcium phosphate may change the growth behavior of the crystals due to the changes on crystal structure. Strontium's incorporation inhibited the growth of crystals, and therefore reduces the size of the crystals[31].

3.10 Conclusion

Sr-doped calcium phosphate (Ca-P) coatings with different microstructures and morphologies have been successfully produced by electrochemical deposition (ECD).

In electrochemical deposition process of calcium phosphates, the morphology and composition of electrodeposited Ca-P coatings can be controlled by process parameters including current density, temperature, and concentration of electrolyte and dose of strontium.

The mechanism of ECD have been investigated using classic thermodynamics and kinetics theory, and the simulated results confirm the findings in the experiments, thus calculation is proved to be valid.

3.11 References Cited

1. Huang, L.-Y., K.-W. Xu, and J. Lu, A study of the process and kinetics of electrochemical deposition and the hydrothermal synthesis of hydroxyapatite coatings. Journal of Materials Science: Materials in Medicine, 2000. **11**(11): p. 667-673.

2. Yang, X., et al., BCP coatings on pure titanium plates by CD method. Materials Science and Engineering: C, 2007. **27**(4): p. 781-786.

3. Eidelman, N., L. Chow, and W. Brown, Calcium phosphate phase transformations in serum. Calcified Tissue International, 1987. **41**(1): p. 18-26.

4. Wang, Y.-q., et al., HA coating on titanium with nanotubular anodized TiO2 intermediate layer via electrochemical deposition. Transactions of Nonferrous Metals Society of China, 2008. **18**(3): p. 631-635.

5. Zhang, Y.-y., et al., Electrochemical deposition of hydroxyapatite coatings on titanium. Transactions of Nonferrous Metals Society of China, 2006. **16**(3): p. 633-637.

6. Shirkhanzadeh, M., Direct formation of nanophase hydroxyapatite on cathodically polarized electrodes. Journal of Materials Science: Materials in Medicine, 1998. **9**(2): p. 67-72.

7. Rakngarm, A. and Y. Mutoh, Electrochemical depositions of calcium phosphate film on commercial pure titanium and Ti–6Al–4V in two types of electrolyte at room temperature. Materials Science and Engineering: C, 2009. **29**(1): p. 275-283.

8. Ban, S. and J. Hasegawa, Morphological regulation and crystal growth of hydrothermal-electrochemically deposited apatite. Biomaterials, 2002. **23**(14): p. 2965-2972.

9. Ban, S. and S. Maruno, Morphology and microstructure of electrochemically deposited calcium phosphates in a modified simulated body fluid. Biomaterials, 1998. **19**(14): p. 1245-1253.

10. Wang, S.-H., et al., Morphology of calcium phosphate coatings deposited on a Ti–6Al–4V substrate by an electrolytic method under 80 Torr. Journal of the European Ceramic Society, 2005. **25**(14): p. 3287-3292.

11. Ye, W. and X.-X. Wang, Ribbon-like and rod-like hydroxyapatite crystals deposited on titanium surface with electrochemical method. Materials Letters, 2007. **61**(19–20): p. 4062-4065.

12. Prado Da Silva, M.H., et al., Transformation of monetite to hydroxyapatite in bioactive coatings on titanium. Surface and Coatings Technology, 2001. **137**(2–3): p. 270-276.

13. Drevet, R., et al., Effects of pulsed current and H2O2 amount on the composition of electrodeposited calcium phosphate coatings. Materials Characterization, 2010. **61**(8): p. 786-795.

14. Lopez-Heredia, M., P. Weiss, and P. Layrolle, An electrodeposition method of calcium phosphate coatings on titanium alloy. Journal of Materials Science: Materials in Medicine, 2007. **18**(2): p. 381-390.

15. Lin, D.-Y., X.-X. Wang, and Y. Jiang, Effect of trisodium citrate on electrolytic deposition of hydroxyapatite coatings. Journal of Biomedical Materials Research Part B: Applied Biomaterials, 2011. **96B**(1): p. 1-8.

16. Eliaz, N. and T.M. Sridhar, Electrocrystallization of Hydroxyapatite and Its Dependence on Solution Conditions. Crystal Growth & Design, 2008. **8**(11): p. 3965-3977.

17. Engstrom, R.C., et al., Measurements within the diffusion layer using a microelectrode probe. Analytical Chemistry, 1986. **58**(4): p. 844-848.

18. Eliaz, N., et al., Electrochemical processes of nucleation and growth of calcium phosphate on titanium supported by real-time quartz crystal microbalance measurements and X-ray photoelectron spectroscopy analysis. Journal of Biomedical Materials Research Part A, 2009. **89A**(1): p. 270-280.

19. Walsh, F.C. and M.E. Herron, Electrocrystallization and electrochemical control of crystal growth: fundamental considerations and electrodeposition of metals. Journal of Physics D: Applied Physics, 1991. **24**(2): p. 217.

20. Chen, S., et al., The simulation of the electrochemical cathodic Ca–P deposition process. Materials Science and Engineering: C, 2009. **29**(1): p. 108-114.

21. Mcdowell, H.G., T. M.; Brown, W. E., Solubility of Ca5(PO4)3OH in the system Ca(OH)2-H3PO4-H2O at 5-degrees-C, 15-degrees-C, 25-degrees-C and 37-degrees-C. Journal of Research of the National Bureau of Standards, 1977. **81A**: p. 273-274.

22. Heughebaert, J.C. and G.H. Nancollas, Solubility of octacalcium phosphate at 25 and 45.degree.C in the system calcium hydroxide-phosphoric acid-potassium nitrate-water. Journal of Chemical & Engineering Data, 1985. **30**(3): p. 279-281.

23. Gregory TM, M.E., Brown WE, Solubility of $CaHPO_4 \cdot 2H_2O$ in the system $Ca(OH)_2 \cdot H_3PO_4 \cdot H_2O$ at 5, 15, 25 and 37°C. Journal of Research of National Bureau of Standards, 1970. **74A**: p. 461 - 462.

24. Tung, M., Eidelman N, Sieck B, Brown WE, Octacalcium phosphate solubility product from 4 to 37°C. Journal of Research of National Bureau of Standards,1988. **93**: p. 613 - 624.

25. David A. Porter, K.E.E., Phase transformations in metals and alloys. Sencond ed1992, London: Chapman & Hall.

26. Boistelle, R. and I. Lopez-Valero, Growth units and nucleation: The case of calcium phosphates. Journal of Crystal Growth, 1990. **102**(3): p. 609-617.

27. Wu, W. and G.H. Nancollas, Determination of interfacial tension from crystallization and dissolution data: a comparison with other methods. Advances in Colloid and Interface Science, 1999. **79**(2–3): p. 229-279.

28. G.H.Nancollas, W.W.a., The dissolution and growth of sparingly soluble inorganic salts: A kinetics and surface energy approach. Pure and Applied Chemistry, 1998. **70**(10): p. 1867-1872.

29. G. H. Nancollas, B.T., Growth of calcium phosphate on hydroxyapatite crystals. Effect of supersaturation and ionic medium. The Journal of Physical Chemistry, 1974. **78** (22): p. 2218-2225.

30. Aogaki, R. and T. Makino, Theory of powdered metal formation in electrochemistry—morphological instability in galvanostatic crystal growth under diffusion control. Electrochimica Acta, 1981. **26**(11): p. 1509-1517.

31. Li, Z.Y., et al., Chemical composition, crystal size and lattice structural changes after incorporation of strontium into biomimetic apatite. Biomaterials, 2007. **28**(7): p. 1452-1460.

Fig. 3-1 The experimental setup for electrochemical deposition.

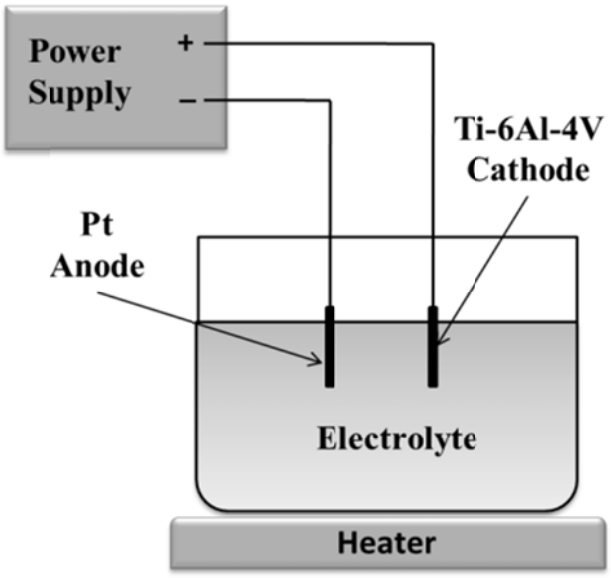

Fig. 3-2 Two different current patterns for electrochemical deposition.

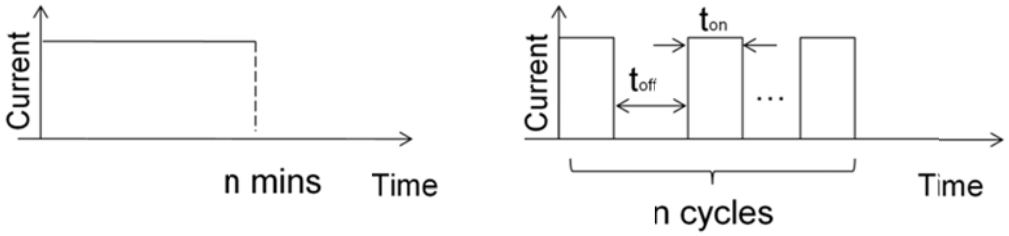

(a) direct current (b) pulsed current

Fig. 3-3 The surface morphologies of samples synthesized under direct current and pulsed current.

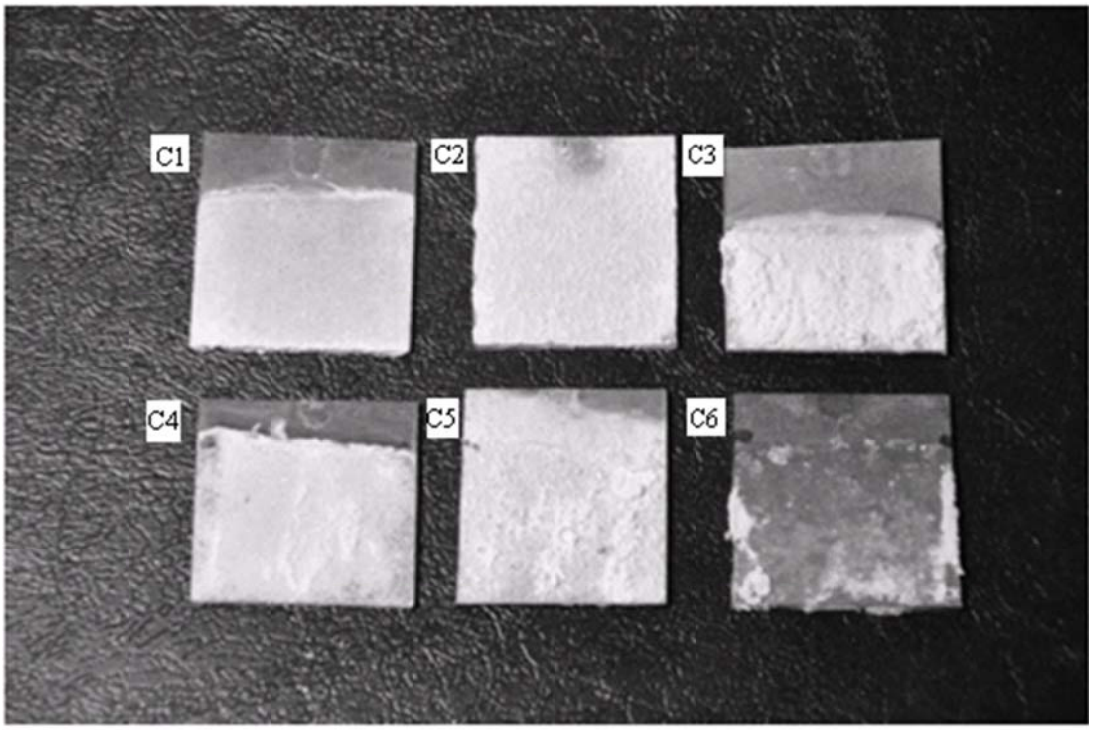

Fig. 3-4 Surface morphology of electrodeposited 10% Sr-doped calcium phosphate coatings at 70°C ,under different conditions: (a) C1, prepared under pulsed current, current density=5 mA/cm^2 ; (b)C2 sample, prepared under pulsed current, current density=10 mA/cm^2; (c)) C5 sample, prepared under direct current, current density=10 mA/cm^2 .

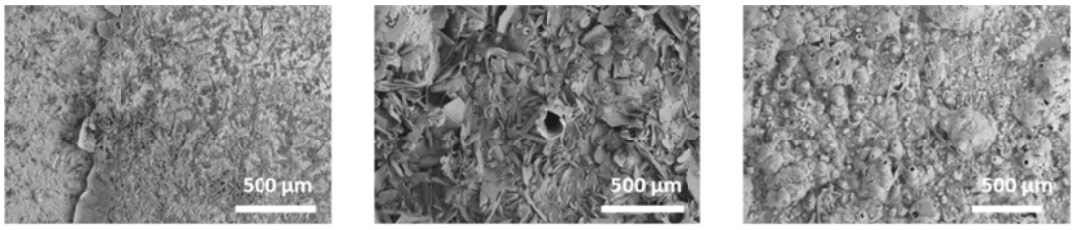

(a) (b) (c)

Fig. 3-5 SEM images of pure calcium phosphate coatings deposited at 90 degree C, with concentration of Ca^{2+} equal to 0.042 mol/L in electrolyte, under pulsed current different current density were applied: (a) 5 mA/cm^2, 20 cycles; (b) 10 mA/cm^2, 10 cycles; (c) 20 mA/cm^2, 5 cycles.

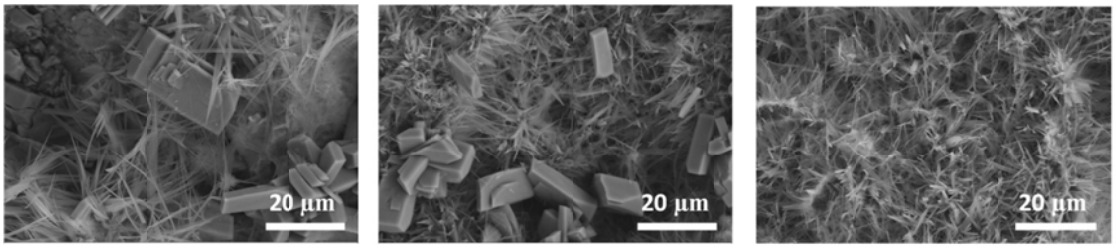

(a) (b) (c)

Fig. 3-6 SEM images of pure calcium phosphate coatings deposited at 70 and 90 degree C, under pulsed current with current density of 10mA/cm^2, 10 cycles were applied. Electrolytes with different concentration (defined by total concentration of Ca^{2+} and Sr^{2+} in the electrolyte) were used: (a) 70ºC, 0.084mol/L; (b) 70ºC ,0.042mol/L; (c) 70ºC, 0.021mol/L; (d) 90ºC, 0.084mol/L; (e) 90ºC ,0.042mol/L; (f) 90ºC, 0.021mol/L.

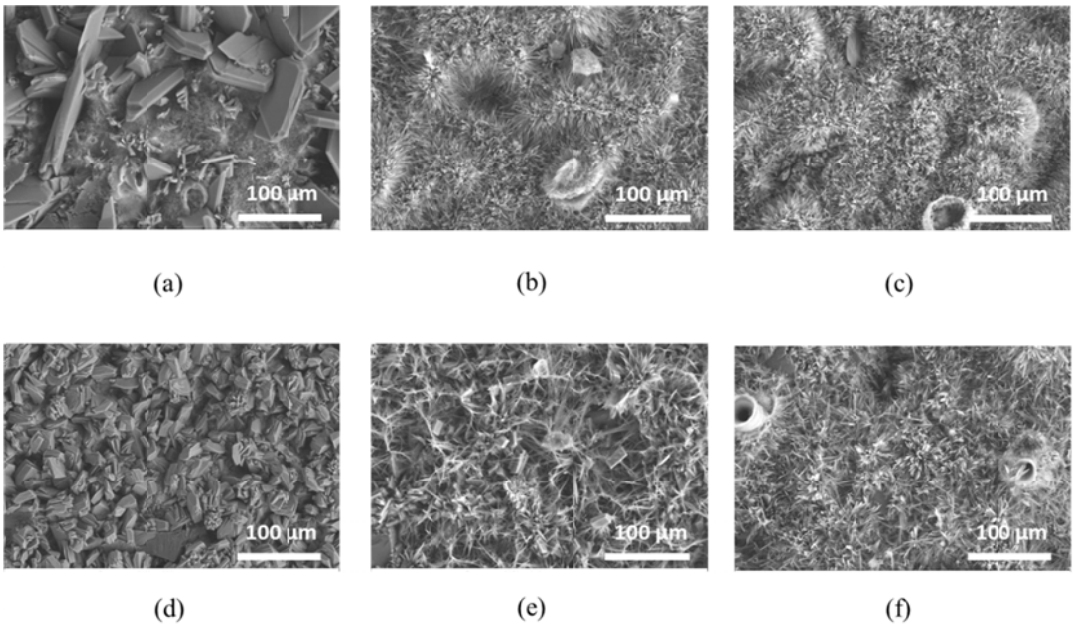

Fig. 3-7 SEM morphologies of calcium phosphate coatings deposited at 90 degree C, under pulsed current with current density of 10mA/cm^2, 10 cycles were applied. Coatings were synthesized by electrolyte with different strontium dose and total concentration of Ca^{2+} and Sr^{2+}. (a) 0% Sr, 0.084 mol/L; (b) 5% Sr, 0.084 mol/L; (c) 10% Sr, 0.084 mol/L; (d) 0% Sr, 0.021 mol/L; (e) 5% Sr, 0.021 mol/L;(f) 10% Sr, 0.021 mol/L.

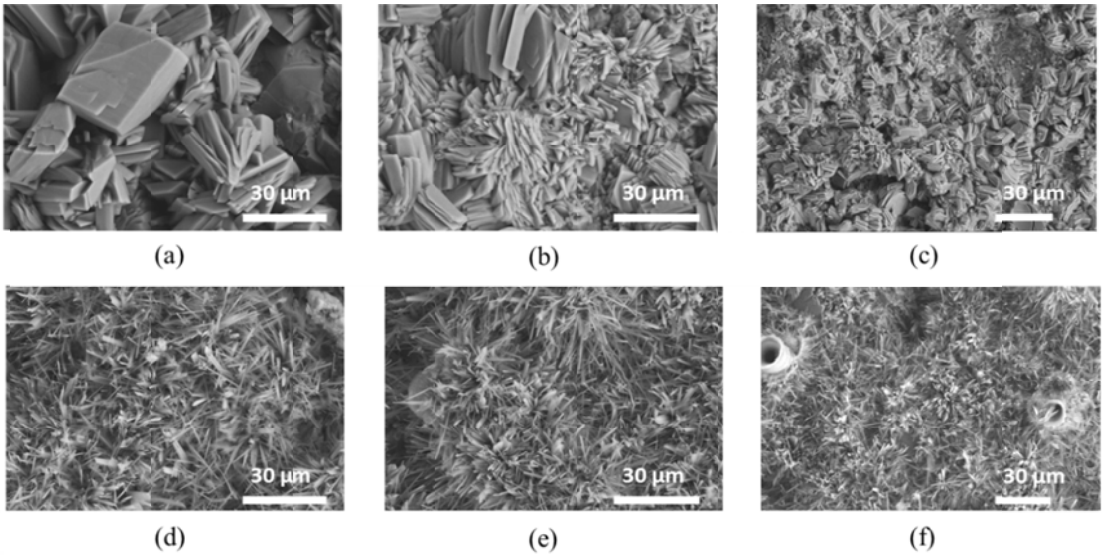

Fig. 3-8 XRD patterns of pure calcium phosphate coatings deposited at 90 degree C, with concentration of Ca^{2+} equal to 0.042 mol/L in electrolyte, under pulsed current different current density were applied: (a) 5mA/cm^2, 20 cycles; (b) 10mA/cm^2, 10 cycles; (c) 20mA/cm^2, 5 cycles.

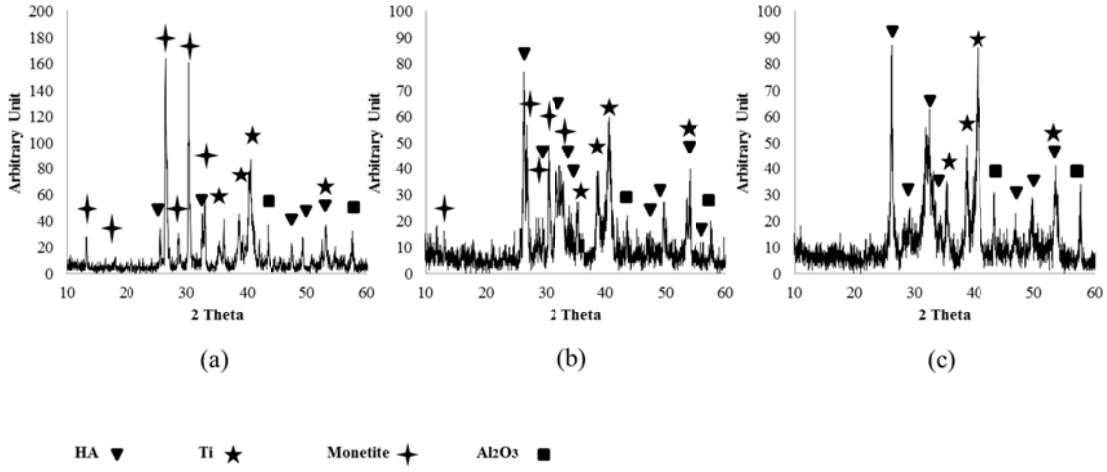

Fig. 3-9 XRD patterns of pure calcium phosphate coatings deposited at 70 and 90 degree C, under pulsed current with current density of 10mA/cm^2, 10 cycles were applied. Electrolytes with different concentration (defined by total concentration of Ca^{2+} and Sr^{2+} in the electrolyte) were used: (a) 70ºC, 0.084mol/L; (b) 70ºC ,0.042mol/L; (c) 70ºC, 0.021mol/L; (d) 90ºC, 0.084mol/L; (e) 90ºC ,0.042mol/L; (f) 90ºC, 0.021mol/L.

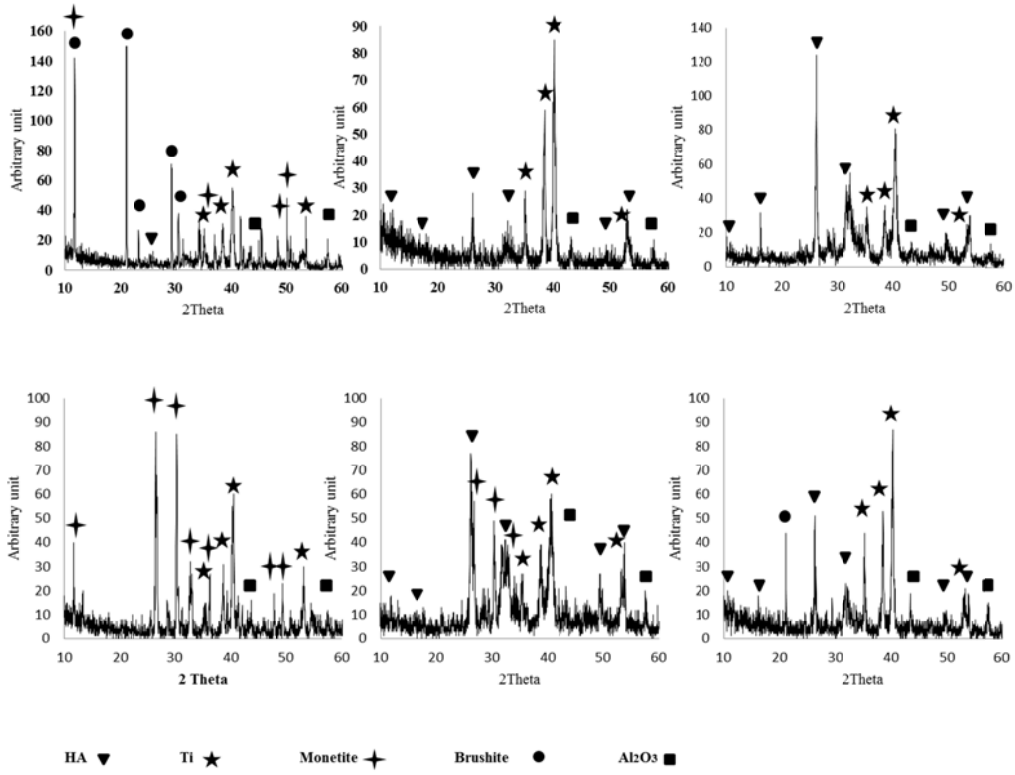

Fig. 3-10 XRD patterms of calcium phosphate coatings deposited at 90 degree C, under pulsed current with current density of 10mA/cm^2, 10 cycles were applied. Coatings were synthesized by electrolyte with different strontium dose and total concentration of Ca^{2+} and Sr^{2+}. (a) 0% Sr, 0.084mol/L; (b) 5% Sr, 0.084mol/L; (c) 10% Sr, 0.084mol/L; (d) 0% Sr, 0.021mol/L; (e) 5% Sr, 0.021mol/L;(f) 10% Sr, 0.021mol/L.

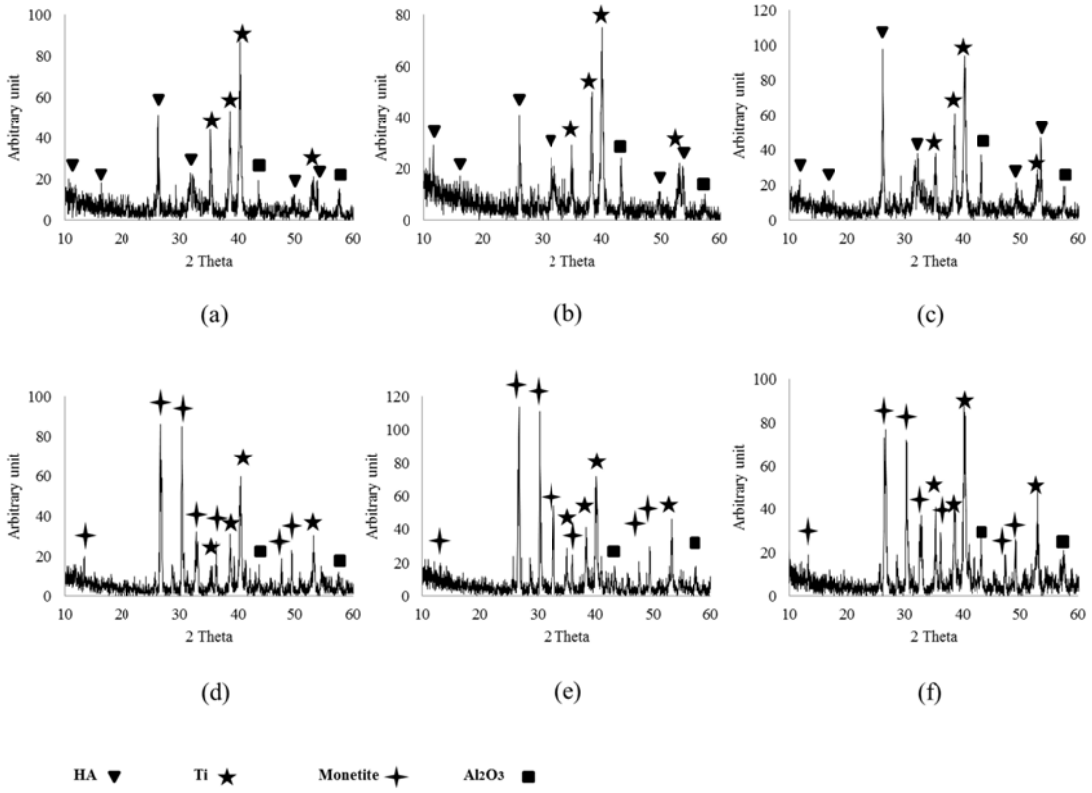

Fig. 3-11. Simulation result by CHEMEQL of the distribution of phosphate species within pH value of the solution ranges from 0 to 14, at 25ºC. The total concentration of all phosphate species was set as 1 mM, and the free concentration of the hydrogen ions in the solution was set to be 1.0×10^{-6} M.

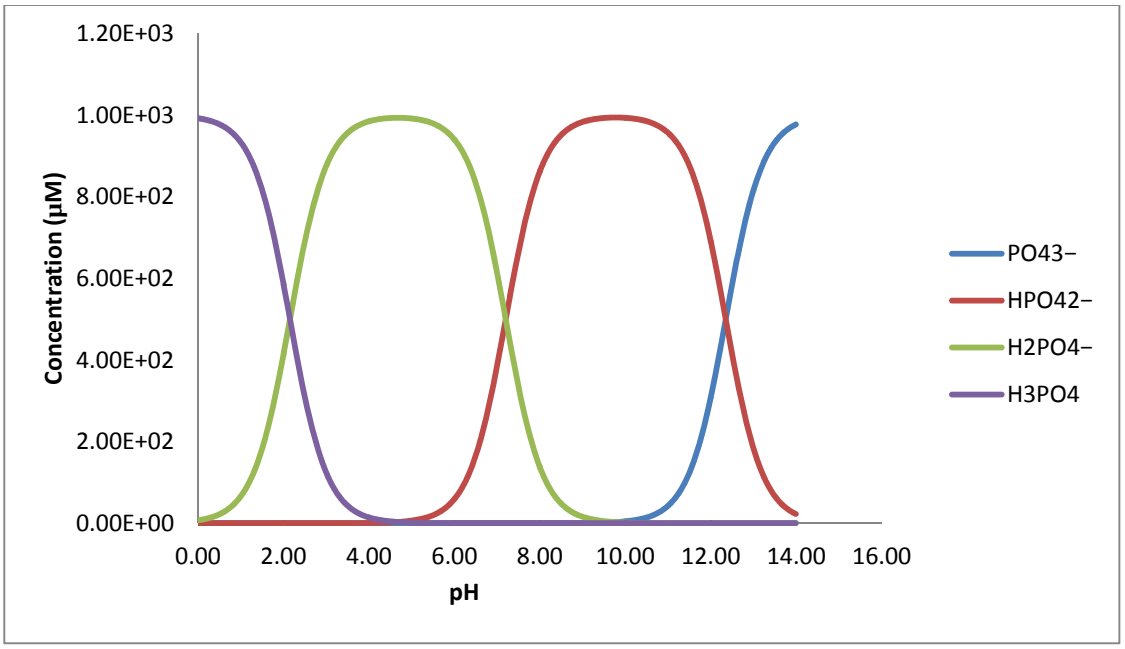

Fig. 3-12. The schematic view of the cathode-electrolyte interface during electrochemical deposition[6, 19].

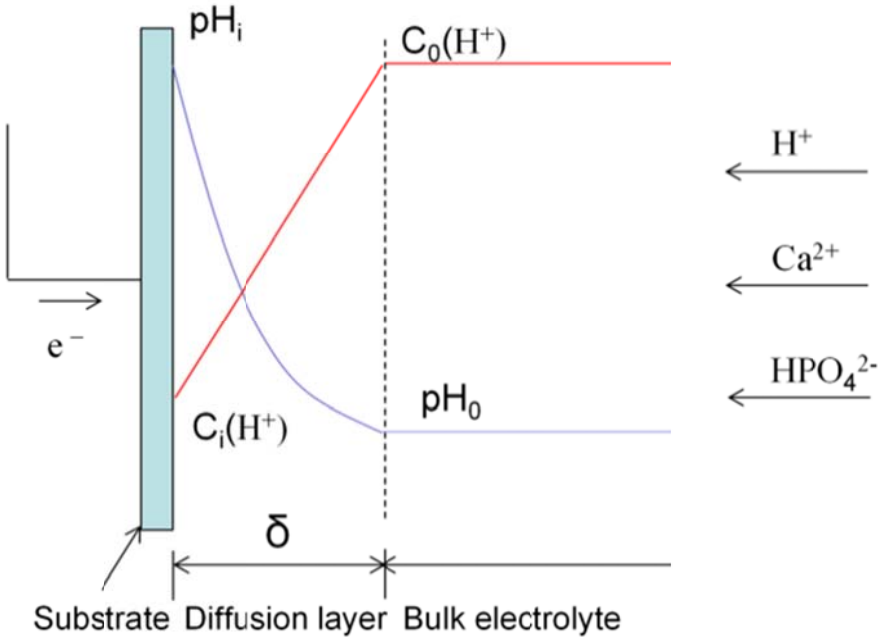

Fig. 3-13 The influence of the distance from the cathode and applied current density on the pH value in electrolyte solution: (a) the pH change with the time and current density (distance is fixed at 0 cm); (b) the pH dependence on distance and time (current density is fixed at 10mA/cm^2).

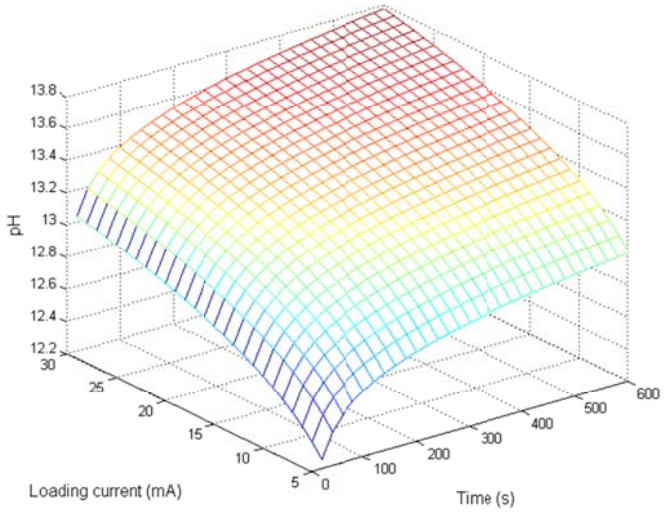

(a)

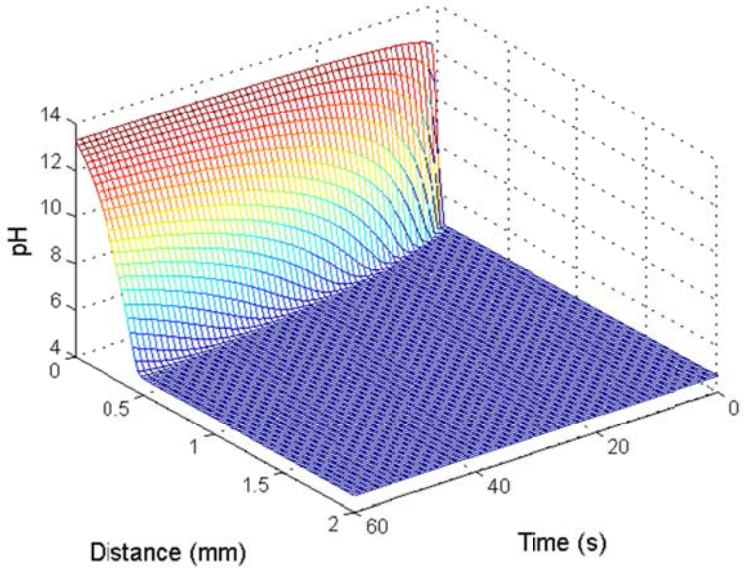

(b)

Fig. 3-14 The influence of pH on the precipitation behavior of calcium phosphates: (a) activity change of ions; (b) the comparison of saturation indexes (SI) of DCPD, HA and OCP; (c) the nucleation rate of DCPD, HA and OCP.

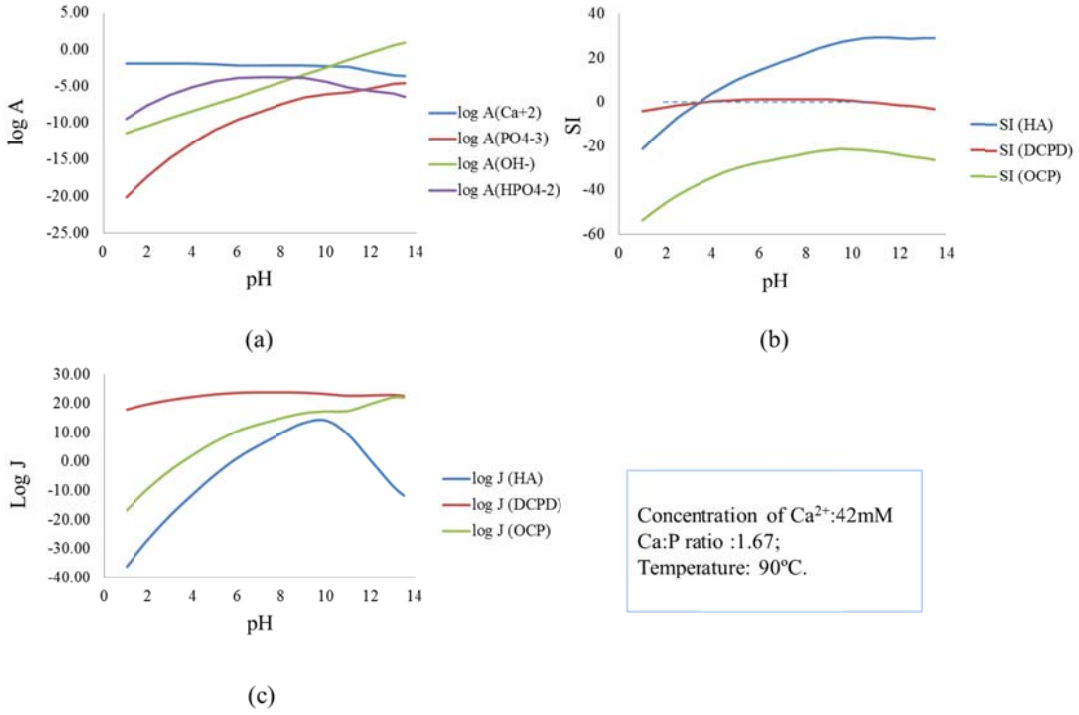

Fig. 3-15 The influence of electrolyte concentration on the precipitation behavior of calcium phosphates: (a) activity change of ions; (b) the comparison of saturation indexes (SI) of DCPD, HA and OCP; (c) the nucleation rate of DCPD, HA and OCP.

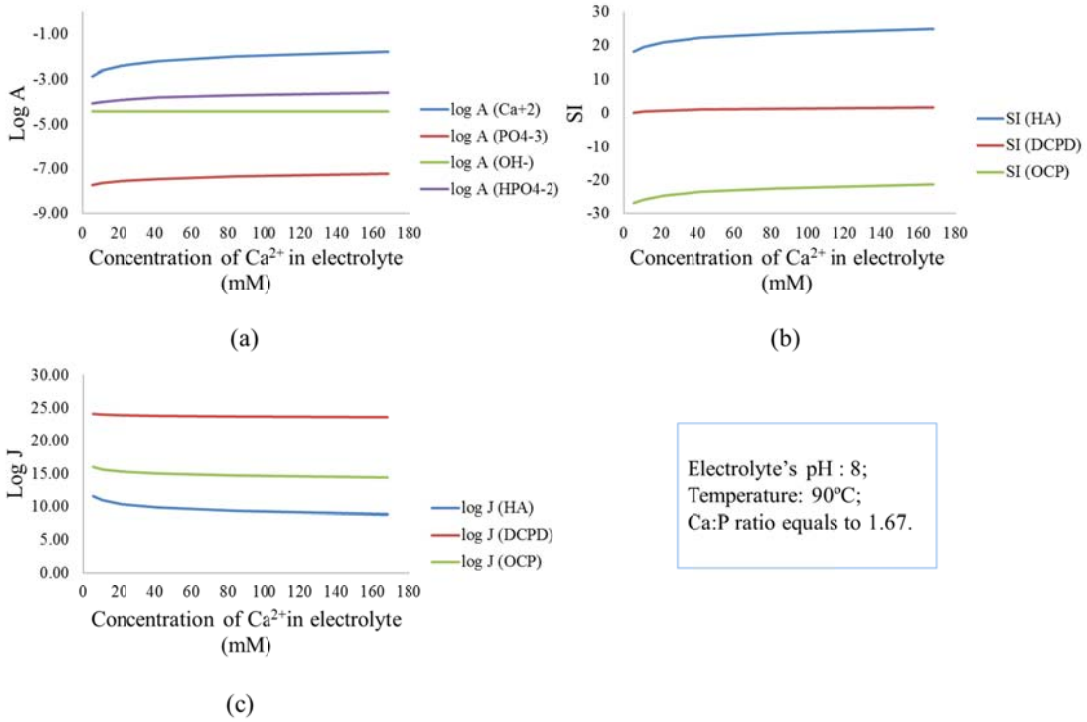

Fig. 3-16 The influence of electrolyte concentration on saturation indexes (SI) of HA, DCPD and OCP under different pH at 90 ºC.

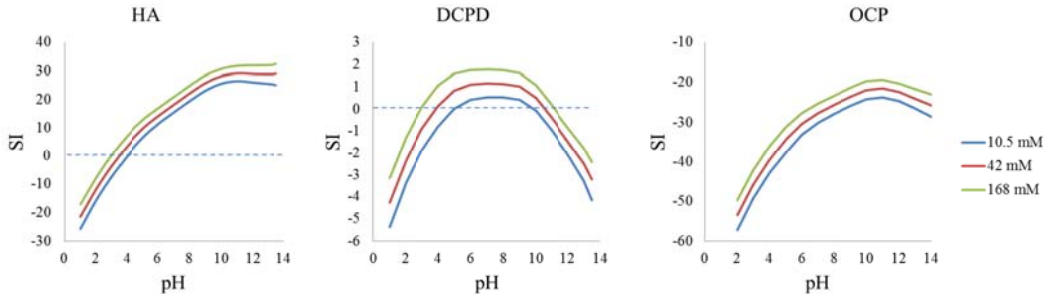

Fig. 3-17 The influence of temperature thermodynamic solubility product K_{sp} of HA, DCPD and OCP under different pH at 90 ºC.

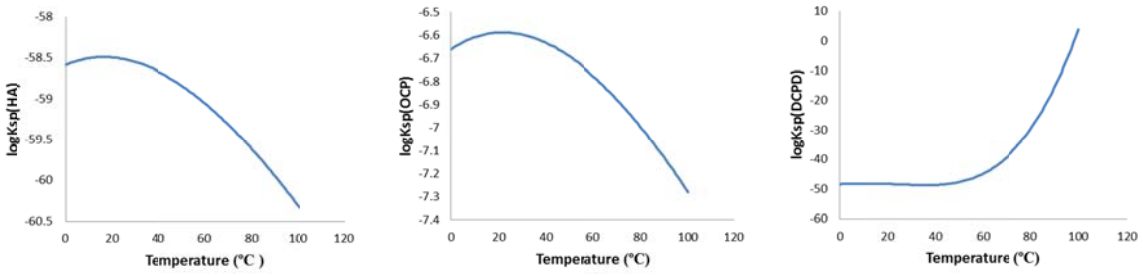

(a) (b) (c)

Fig. 4-18 The influence of temperature on activity of ions, electrolyte pH = 8, original concentration of Ca^{2+} is 42mM, with Ca:P ratio equals to 1.6.

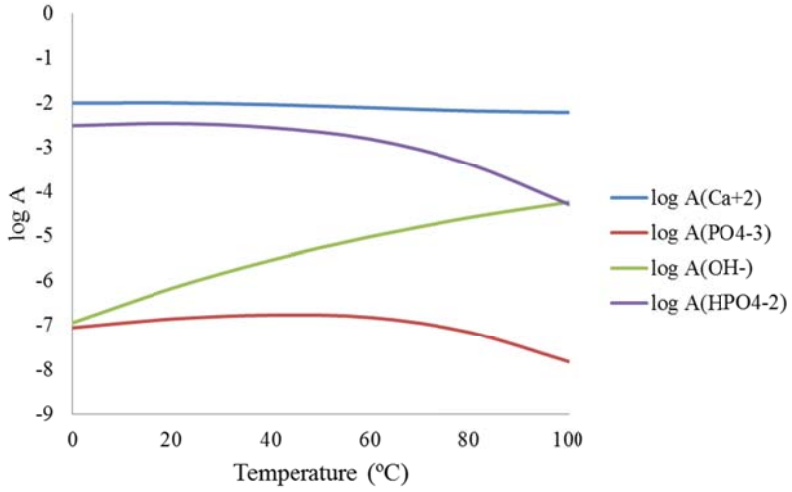

Fig. 3-19 The influence of electrolyte temperature on the supersaturation indexes of different calcium phosphate phase, the electrolyte containing 42mM Ca^{2+}, with Ca:P ratio equals to 1.67.

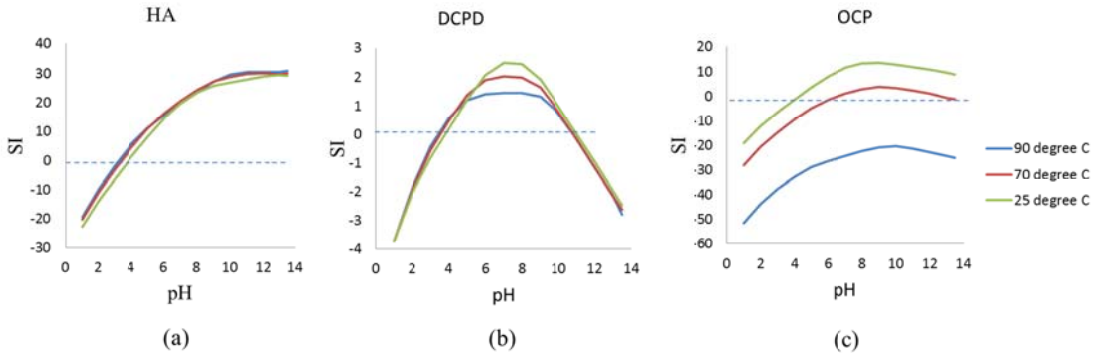

Fig. 3-20 The influence of electrolyte temperature on nucleation rate of different calcium phosphate phase, the electrolyte containing 42mM Ca^{2+}, with Ca:P ratio equals to 1.67.

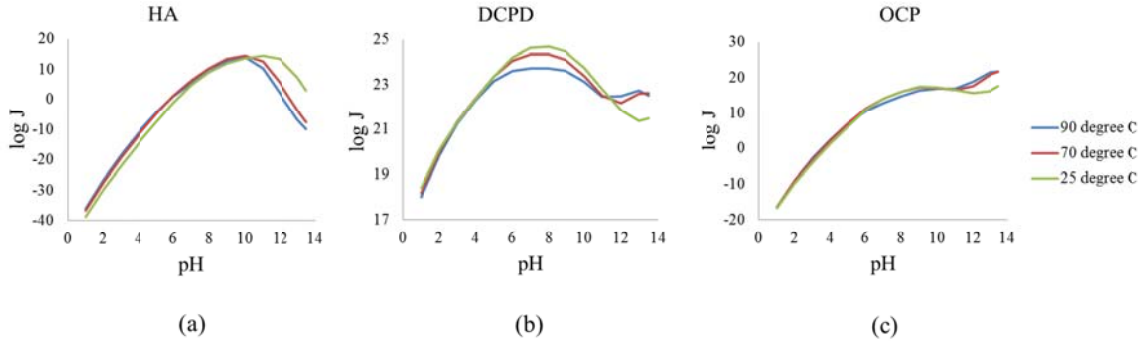

Fig. 3-21 The distance and time's combinations to obtain pH = 10.5, under three different current density levels: 5mA/cm^2, 10mA/cm^2 and 20mA/cm^2.

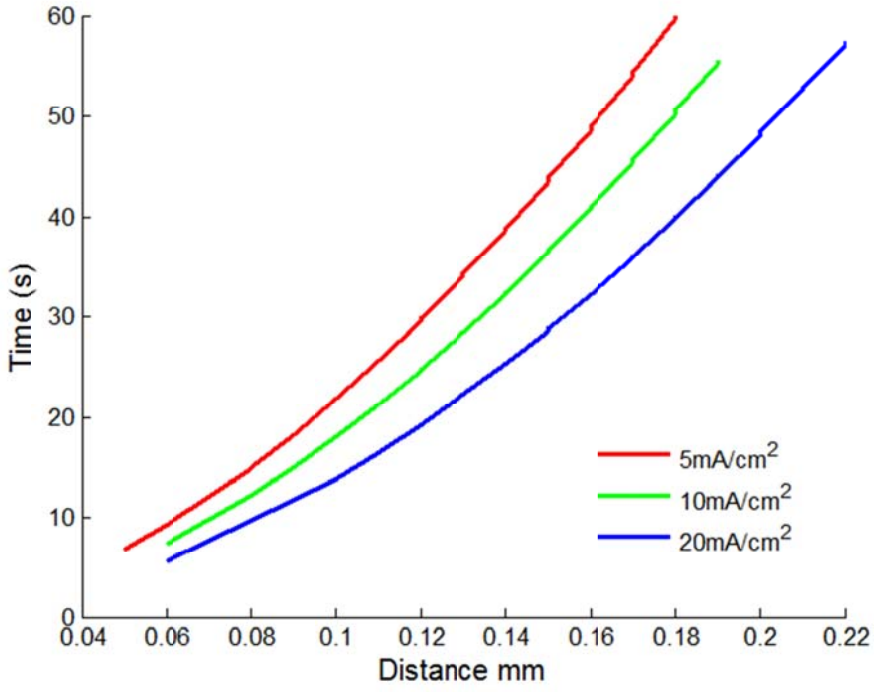

Chapter 4

AIR PLASMA SPARY OF CALCIUM PHOSPHATE COATINGS

4.1 Abstract

In this chapter, a systematic investigation was performed using process map approach to evaluate the influence of spray parameters on the properties and performances of air plasma sprayed calcium phosphate coatings. Two primary parameters, the current and total gas flow were adjusted to achieve various in-situ particle states resulting in coatings with different microstructure and phase composition. Subsequent analysis was used to determine material properties and assess the in vitro performances through simulated body fluid test. The aim of this study was to build the links between particle states, coatings properties, in vivo performance of plasma sprayed calcium phosphate coatings. With the knowledge, produce coatings with favorable phase composition and suitable microstructure and thus high bioactivity become possible.

4.2 Experiment Procedure

4.2.1 HA Powder and Preparation of the Coating Substrate

Commercial HA powder (F.J. Brodmann & Co., Harvey, LA) was used as feedstock to produce coatings in this study. The general morphology and size distribution of the HA powder were observed using SEM. As shown in the Fig. 4-1(a) SEM image, this powder was comprised of loosely agglomerated nanoparticles with an average agglomerate size of 35 μm. The purity of the powder was determined by XRD. The XRD pattern of powder, shown in Fig. 4-1(b), indicated that the main composition of the powder was hydroxyapatite, no significant peaks of impurities were found to be present. Low carbon steel coupons (~5 cm × 2.5 cm × 0.5 cm) were used as substrates. Prior to deposition, those coupons were grit-blasted using Al_2O_3 and then ultrasonic cleaned in acetone to obtain rough and clean surface suitable for deposition.

4.2.2 Design of Experiments

In this study, HA powder was plasma sprayed at a standoff distance of 100 mm using a nozzle 7 mm in diameter with a commercial F4 plasma spray torch (Sulzer Metco, Westbury, NY). Plasma gases used were Ar_2 and H_2, with a constant volume ratio

of 9:1. Gun traverse speed was 500 mm/sec, and 40 passes were sprayed for each coating. Argon (at 5m/s) was used as the carrier gas for the spray powder, powder discs was set at 2.0 rpm, stirrer at 50 rpm during spray.

As discussed previously, plasma spray process is a very complicated technique, which has a lot of variables including electric power input, power feed rate, composition of the plasma forming gas, spray distance. However, behind those complex process parameters, the more intrinsic variable that directly affects the coatings properties is particles state, which can be described by temperature (T), velocity (V) and diameter (D) of the particle. Particle state is the most importance factor which controls splat formation and solidification behaviors in plasma spraying processing, and thus is considered to be critical factor that affect the properties of the coatings. In this study, two primary parameters, the current and total gas flow (TGF), were changed to achieve various particle state. In order to measure the particle state in each condition, A DPV 2000 sensor (Tecnar Automation td. Quebec, Canada) was employed to perform realtime in-flight diagnostics. The information of size, temperature and velocity for each of about 5,000 particles was obtained by this sensor at the plasma flow center.

To investigate the impact of substrate temperature, air cooling was applied from the back of the substrate for half of the coating samples. The design of experiments is shown in Table 4-1.

Table. 4-1: Plasma spray parameters

Sample	Current(A)	TGF(SLM)	Cooling
1N	402	50	No
1C	402	50	Yes
2N	302	60	No
2C	302	60	Yes
3N	303	40	No
3C	303	40	Yes
4N	500	60	No
4C	500	60	Yes
5N	500	40	No
5C	500	40	Yes

Plasma sprayed coatings are built up by accumulating of single splats, thus investigation of the behavior of single splat is meaningful. It is an essential clue to understand the formation of the coatings, a bridge to connect parameters and as sprayed coating properties.

Therefore, in this study, single splats samples were also prepared sharing the same parameters with coatings' conditions without air cooling, except the gun traverse speed was 1000 mm/sec, and a single pass was completed for each sample. Fig. 4-2 shows the T-V distribution for experimental conditions produced by this experimental design in the current study. The values of temperature and velocity of each condition were obtained by averaging approximately 5000 particles' data captured by the DPV-2000 sensor. The arrows in the figure show the impact of total gas flow (TGF) and current on particle state.

Characterization

The morphology of HA feedstock, splats, coating surfaces and cross-sectional microstructures were observed using a scanning electron microscopy (LEO 1550) under 20keV accelerating voltage. The measurement of porosity was performed by image analysis of cross-sectional SEM images. This method can be used to measure porosity due to the contrast between the darker pores and brighter coating materials[1]. In the

analysis process, SEM images were transformed from gray scale into binary, and then the porosity of the coating was calculated.

Phase identification of the feedstock and obtained coatings was performed by employing a SCINTAG X-ray diffractometer with CuKα radiation. The operating voltage was set as 45 kV and the current was 25 mA. Spectra were obtained from 2θ range of 20 to 60°, at a scanning speed of 2° 2θ/min. The spectra were analyzed using MATCH software and JCPDS cards. The crystallinity was evaluated by the following equation:

$$\text{crystallinity}(\%) = \frac{I_c}{I_t}$$

Where I_c is the integrated intensity of all the crystalline peaks above amorphous hump over the whole 2θ range, and I_t is the total integrated intensity of the entire XRD pattern over the range, which includes the sum of crystalline peaks and amorphous humps.

In order to evaluate the bio-performance of the samples, the as-sprayed samples deposited under different conditions were soaked in simulated body fluid (SBF) which had the nearly equal ion concentration to those in human blood serum for 6 weeks. The SBF used in this study followed the recipe of standard simulated body fluid [2] and was kept in a water bath at 37°C during the incubation periods. To understand how crystallinity affects the behaviors of samples in simulated body fluid (SBF), selected samples were heat treated at 700º C for 2 h to achieve higher crystallinity and were incubated in the SBF test. After exposure, the samples were taken out, washed with distilled water then dried in air for XRD and SEM examination.

4.3 Results and Discussion

4.3.1 In-flame Particle State and Morphology of the Single Splats

In some research, the two parameters: temperature and velocity are used to describe particle state. However, due to the dynamic character of the plasma stream, this description is not sufficient[3]. Instead of that, describing particle state through melting index (MI) and kinetic energy (KE) was developed and used by several researchers which is considered to be more comprehensive and sufficient. [4-6]

In this study, individual particles' state parameters: diameters (D), temperature (T), velocity (V), were converted into two group parameters: melting index (MI) and kinetic energy (KE). For MI calculation[6]:

$$\mathrm{MI} = \frac{2\mathrm{LT}}{\mathrm{VD}} \tag{4-1}$$

Where, L was the spray distance.

For KE calculation[6]:

$$\mathrm{KE} = \frac{\mathrm{mv}^2}{2} = \rho \frac{4\left(\frac{\mathrm{D}}{2}\right)^3 \pi}{3} \mathrm{v}^2 \tag{4-2}$$

For each condition, the group parameters were obtained by averaging the MI and KE values of all the particles captured by DPV2000 sensor in the certain condition.

An investigation of single splats morphology shown in Fig. 4-3 indicates that there were three types of splats: type A, the splats with regular round shape; type B, the splats with splash morphology; and type C, the partially melted splats with crushed morphology which left a "cloud" trace of tiny particles on the substrate surface. The variety of splat morphologies should be attributed to different in-flame particle states and the subsequent solidification process. When a particle is fully melted in the plasma stream, it can be type A or type B. It can be noticed that all of particles with the smallest size were found fully melted and belonged to type A, no matter in which spray condition. Fig. 4-4 shows the statistic results of particle melting index and kinetic energy at different particle diameters, which indicates that in the same condition, smaller particles had higher melting index and lower kinetic energy compared to those larger ones. Since small particles' melting index was higher compared to those large ones, they had higher plasticity. And small particles usually had lower kinetic energy than those large ones, which means they could suffer lower force when they impacted the substrate. Both of the facts allow small particles to have higher probability to keep the integrated round shape, while larger particles tended to get a splash shape. The formation of type C splats

occurred when the particle is partially melted in the plasma flame. A large unmelted core consisting of an agglomerate of nano-sized particles was retained and when these particles reach the substrate, the cores were crushed and explode under the strong impact force leaving a cloud of nanoparticles.

In Fig. 4-3, it can also be observed that melting index and kinetic energy affect the splats' melting state and morphology, which suggests the mechanisms of splat formation. In condition 1, 3 and 5, due to high melting index, most of the splats belonged to type A and type B, and with the increase of KE, more type B splats appeared. In the lower melting index condition 2 and 4, type C splats could be observed. Condition 1 and 4 had similar KE, but 1 had higher melting index, which induced type C splats evolve to the other two types in this condition.

4.3.2 Microstructure

Fig. 4-5 shows the cross sectional microstructures of as-sprayed coatings from various spray conditions. Coatings were porous and contain unmelted particles, interlamellar pores and globular pores.

Significant differences in coating microstructure can be observed in the coatings deposited with various spray conditions. In the low melting index area (conditions 2 and 4), coatings were porous with many unmelted particles and interlamellar pores which confirms the findings in the related single splat samples. While in the high melting index conditions (3 and 5), coatings were more dense, but with sample 5C being an exception, which had more and larger globular pores.

Unmelted particles could become part of the microstructure from partially melted type C splats. This feature usually can be found in coatings deposited in low melting conditions (condition 2 and 4). With the increase of melting index, in-flame unmelted particles decreased, thus very few unmelt structure could be found in the coating deposited in high melting index conditions (condition 3 and 5). The interlamellar pores result from poor wetting/adhesion between the splats as they accumulated to form the coating[7] . High melting index and kinetic energy had positive effects on splats' attachment and bonding therefore can decrease interlamellar pores. It can also be

observed that in the same condition group, coatings deposited on cooled substrates hadmore interlamellar cracks compared to those on non-cooled ones. This result is due to the weaker bonding between splats because of the cooler substrate.

Globular pores (including “half-penny” shape pores) were formed due to the expansion of trapped air captured from substrate when the impacting particles were still molten [8, 9]. The trapped air bubbles can be observed under optical microscope, as shown in the optical images of splats (Fig. 4-6). The globular pores tended to become larger under the cooled substrate condition, which can be obviously observed in the condition 5. This condition had the highest melting index.

This phenomenon is probably due to the different expansion rate of the captured gas. The original temperature of air bubble captured from a cooler substrate is lower than those captured from a hotter substrate. While heated by the splat with same temperature, the gas captured from a low temperature substrate suffered larger increase in temperature, and therefore a larger expansion rate[8].

Besides that, when a coating is made without cooling, substrate temperature is higher than those with cooling. Higher substrate temperature slows down the solidification process of the splats, which allows captured gas to move out of the splats. While in the cooler substrate, gas bubbles can be sealed quickly by fast solidified splats, and therefore form larger globular pores.

Coating porosity was evaluated use image analysis with the results shown in Fig. 4-7 for each condition sprayed on both cooled and noncooled substrates. The trend of porosity for coating made without cooling was 4>2>1>5>3; for coatings made with cooling was 4>5>2>1>3. And in the same condition cooling sample had more porosity than no cooling ones. In the low melting index range (conditions 2 and 4), as discussed before, the particles were partially melted and the bonding between splats was weak. Therefore, large amounts of interlamellar cracks formed, introduced high porosity; when the melting index increase, usually, the coating will become denser, unless the large amount of globular pores happen, such as condition 5 under cooling. The process map for cooled samples indicates the lowest porosity could be achieved in the middle of the

process space. In both of the conditions, the highest porosity appears at the range which is the combination of low MI and low KE.

4.3.3 Thickness and Deposit Efficiency

In thermal spray, relative deposit efficiency can be estimated by thickness increase per pass. However due to the different porosities of the coatings, this measurement cannot evaluate how much mass is deposited. In this study, deposit efficiency (DE) is introduced which is defined as follow:

$$\mathrm{DE} = \frac{\mathrm{T}(1-\mathrm{P})}{\mathrm{N}} \tag{4-3}$$

Here, T is the thickness of the coating, P is the total porosity of the coating, and N is the number of passes.

A comparison of the thickness is shown in Fig. 4-8 (a), deposit efficiency of the samples is shown in Fig. 4-8 (b) and a second-order process map of deposit efficiency in MI-KE Space is shown is 8(c).

It can be observed that, within the same condition group, non-cooled samples had higher deposit efficiency compared to cooled ones. However, when melting index become higher, the difference tended to become smaller. The rule of thickness between cooled and non-cooled samples is not very clear due to the complex coupling factors: cooling tends to decrease the deposited mass because of lower cohesive strength between splats, but cooling also introduces more porosity that “expands” the coating to make it thicker. Therefore, using defined DE rather than thickness to indicate actually deposited mass is more effective.

The trend among the different groups of both thickness and deposit efficiency was: 1, 3, 5 > 2, 4. This can be clearly understood through the related single splats of each condition. In the conditions 1, 3 and 5, with higher MI, there were more fully melted type A and type B splats, which means higher deposit efficiency. In the other two conditions 2 and 4, with lower MI, type C splats appeared. The tiny debris came from the crushed unmelted cores which could not be efficiently deposited causing a loss of the powder and low deposit efficiency. However, when MI increased further, the deposit

efficiency decreased, because of the high decomposition rate of HA, this will be further discussed later. Kinetic energy also had positive effect on DE, when compare condition 2 and 4, 4 had higher melting index, but the deposit efficiency of them turned out to be close, due to 2 having higher kinetic energy. Second-order process map Fig. 4-8 indicates the region can obtain the highest deposit efficiency in MI-KE space, which is in the middle of the process range for both of the cooling and uncooling conditions.

4.3.4 Coating Composition

As discussed in Chapter 1, during the process of plasma spray, hydroxyapatite particles undergo melting and decomposition due to the extremely high temperature. They may transform into amorphous phase or other phases including oxyhydroxyapatite (OHAP), oxyapatite, tricalcium phosphate (TCP), tetracalcium phosphate (TTCP), and calcium oxide (CaO)[10-13]. For calcium phosphate coatings, the crystallinity of the coatings is very important. It not only has influences on the coating structural stabilization, but also controls the bioactivity performance of the coating. The amorphous contents dissolve much faster than crystallized ones. The dissolution of amorphous contents can provide a rich Ca-P area around the coating[14] which benefits the ingrowth of new bone. However, on the other hand, if there is too much amorphous content, the dissolution speed of the coatings will become too high, so the structure will be weaken and may induce the failure of the whole coating. Therefore, to tailor the proper crystallization to fit the application is very essential for calcium phosphate coatings.

The crystallized content of the as sprayed coatings comes from two parts: one is from the unmelted core of the particles; the other is from the recrystallization of amorphous contents due to the heat accumulation during spray. Thus, there are two main factors that could affect the crystallinity of the coating: the melting state of the particles and the cooling rate of the attached particles on the substrate. The temperature of the particle controls the degree of melting before it impacts the surface of the substrate. When the molten particles attach to the substrate, the temperature and thermal conductivity of the substrate together with the flattening ratio of the splats will mainly determine the cooling rate of the splat. High cooling rate enables the amorphous phase to form, while low cooling rate allows the splat to recrystallize. Particles with higher

melting index do not necessarily mean they can introduce more amorphous phase, because they also cause heat built-up of the substrate. Heat built-up increases the temperature of the substrate, therefore, lowering the cooling rate of the splats, which tends to increase the crystallinity of the coatings.

In this study, different spray parameters were used to achieve samples with different crystallinity and phase composition. The XRD patterns for the various conditions are shown in Fig. 4-9. Comparison of the crystallinity of as-sprayed samples is shown in Fig. 4-10. From those figures, the trend of crystallanity of non-cooled samples from highest to lowest was: 5>3>4>1>2, for cooling samples was: 4>3>1>2>5.

For non-cooled samples, MI had significant effect on crystallinity, with increased MI corresponding to increased crystallinity. This can be attributed to the accumulation of heat in the substrate leading to coating recrystallization. Meanwhile, no clear dependence of KE was observed for sample's crystallinity.

For cooled samples, the crystallinity was affected by both MI and KE. With the increase of KE, the crystallinity tended to decrease, especially in low MI index area. This may due to the increasing flattening ratio. Meanwhile, the effects of heat accumulation from high MI particles became weaker compared to non-cooled conditions. Due to the cooling effects, fast cooling down of high MI particles tend to form an amorphous phase. That was the reason for the 5C sample having very low crystallinity, while the 4C sample, which benefitted from both unmelted cores and accumulation of heat, became the highest crystallized one.

However, the difference of crystallinity between the various conditions was not significant, indicating that due to the complex effect of particle state as discussed, the process parameters explored in this study did not have a large effect on the crystallinity. While comparing the crystallinity of samples in the same condition group but different substrate state, the samples without cooling always have higher crystallinity than those with cooling. This confirmed the effect of splat cooling rate as discussed previously.

4.3.5 Bioactivity

Bioactivity, which determines how well the material will be incorporated in a live body, is one of the most important properties for these coatings. SBF tests have been widely used as an in vitro method to investigate the bioactivity of biomaterials. The formation of bone-like apatite on the surface of biomaterials is considered to be the essential requirement when they are implanted in the living body[2]. In SBF, with surrounding ion concentrations close to human blood plasma, calcium phosphates can be similarly formed on the surface of soaked biomaterials. Thus, this method can be used to predict the in vivo performance of implanted biomaterials.

Obviously, the thickness of the deposit layer of HA is affected by the ratio of amorphous material in the coating. Because the amorphous phase has high solubility in SBF, it will provide high concentrations of calcium and phosphate ions around the coating [14]. Thus the apatite can nucleate more easily and deposition process can be accelerated. Porosity and thickness of the coating also affect the thickness of deposit HA, since they have influences on the amount of material that can dissolve from the coating.

From the SBF test of this study, it can be observed that after a 6-week soaking, the surfaces of the coatings are covered by a newly formed layer.

The ability of as-sprayed samples to deposit apatite on the surface was much higher than heat treated samples. Fig. 4-11(a) and (c) shows the top view of as-sprayed samples and heat treated samples after the 6 week SBF test respectively. It can be observed that the surface of the as-sprayed sample was fully covered by a thick layer of newly formed material, while only a small amount of mass deposited on the surface of heat treated samples. The cross section view of heat treated samples in Fig. 4-11(b) and as sprayed samples in Fig. 4-11(d) after SBF test also show the dramatic difference between the two types of samples.

Fig. 4-12 shows the typical XRD patterns of as sprayed and heat treated samples after SBF test. For as-sprayed samples, after 6 weeks SBF test, the main peaks of hydroxyapatite were still maintained, while the peaks from TCP and TTCP disappeared. The amorphous hump's presentation suggested that the newly formed layer could be

amorphous apatite. For heat treated samples, the XRD patterns didn't change much after SBF test, but the peaks become lower, that may due to the dissolution of the coatings.

Comparison of the thickness on as-sprayed samples after SBF tests is shown in Fig. 4-13.The trend for thickness was 5>4>1>3>2. The as-sprayed coating thickness and porosity of 2 is greater than 4. The dramatic difference in the deposited layer's thickness after SBF test could be attributed to the difference in the morphology and size distribution of the two types of pores. Condition 2 has more narrow interlamellar cracks, and condition 4 contains more large open interlamellar pores. In SBF, interlamellar cracks mostly expose unmelted particles in the coating. Interlamellar pores may expose more amorphous parts of the coatings, which provide more dissolved calcium and phosphate ions in the solution, and then help to deposit apatite layer.

In the same condition group, the deposited apatite layers had almost the same thickness. That may be because although the crystallinity of samples with cooling was lower than those without cooling which encourages the growth of new apatite, the deposit efficiency and porosity of them were also lower compared to coatings without cooling. The comprehensive effects of these three factors contribute to the observed similar deposit thickness.

4.4 Conclusions

In the current study, a systematic investigation were carried out to evaluate the relationship between spray parameters and the properties of coatings, and to build the links between spray parameters, particle states, coatings properties and performance. Spray parameters current and TGF had significant effects on the particle state which can be expressed as melting index (MI) and kinetic energy (KE), and ultimately impacted the morphology of the coating building blocks: splats. Three different splat morphologies were identified: type A, the splats with regular round shape; type B, the splats with splash morphology; and type C, the partially melted splats with crushed morphology which left a trace of "cloud "of tiny particles on the substrate surface. The type C splat was the main cause of lower deposition efficiency in these HA coatings.

Highest porosity was achieved at low MI and low KE range. For non-cooled samples, lowest porosity point was in high MI and high KE range. For cooled samples indicates the lowest porosity appears in the middle of the process space. Cooling substrate will introduce higher porosity.

MI had significant effect on crystallinity. In this process space, high MI corresponded to increasing crystallinity. KE was observed to have no obvious impact on crystallinity. However, crystallinity decreased when the substrate was cooled.

Deposit efficiency was increased by increased KE. Increasing MI can also achieve higher deposit efficiency, but extremely high MI can cause fast decomposition of HA, thus lowering the DE. Uncooled samples had higher DE than those cooled ones.

In vitro SBF testing of the coatings, suggested that higher crystallinity will decrease the deposited apatite layer in SBF, which indicated high crystallinity samples have lower bioactivity. The thickness of the deposited layer in SBF is controlled by the crystalline, and the type and number of pores and thickness of coatings.

In conclusion, plasma spray parameters do have significant effects on the particle state, which controls the thickness, microstructure and composition of coatings, and ultimately affect the bioactivity performance of the coatings. Through the effective tool process map, links between spray parameters, particle states, coatings properties, in vivo performance of plasma sprayed HA coatings can be built, thus tailor the coating properties and performance become possible.

4.5 References Cited

1. Deshpande, S., et al., *Application of image analysis for characterization of porosity in thermal spray coatings and correlation with small angle neutron scattering.* Surface and Coatings Technology, 2004. **187**(1): p. 6-16.

2. Kokubo, T. and H. Takadama, *How useful is SBF in predicting in vivo bone bioactivity?* Biomaterials, 2006. **27**(15): p. 2907-2915.

3. Srinivasan, V. and S. Sampath, *Estimation of Molten Content of the Spray Stream from Analysis of Experimental Particle Diagnostics.* Journal of Thermal Spray Technology, 2010. **19**(1): p. 476-483.

4. Li, L., et al., *Particle characterization and splat formation of plasma sprayed zirconia.* Journal of Thermal Spray Technology, 2006. **15**(1): p. 97-105.

5. Sampath, S., et al., *Role of thermal spray processing method on the microstructure, residual stress and properties of coatings: an integrated study for Ni–5 wt.%Al bond coats.* Materials Science and Engineering: A, 2004. **364**(1-2): p. 216-231.

6. A.Vaidya, G., Bancke, S.Smapath, and H. Herman. *Influence of Process Variables on the Plasma Sprayed Coatings:An Integrated Study*. 2001. Singapore,Materials Park,OH: International thermal spray conference(ITSC).

7. Kulkarni, A., et al., *Processing effects on porosity-property correlations in plasma sprayed yttria-stabilized zirconia coatings.* Materials Science and Engineering: A, 2003. **359**(1-2): p. 100-111.

8. Qu, M., et al., *Observations of nanoporous foam arising from impact and rapid solidification of molten Ni droplets.* Applied Physics Letters, 2007. **90**(25): p. 254101.

9. Deshpande, S., S. Sampath, and H. Zhang, *Mechanisms of oxidation and its role in microstructural evolution of metallic thermal spray coatings—Case study for Ni–Al.* Surface and Coatings Technology, 2006. **200**(18-19): p. 5395-5406.

10. Hartmann, P., et al., *Solid State NMR, X-Ray Diffraction, and Infrared Characterization of Local Structure in Heat-Treated Oxyhydroxyapatite Microcrystals: An Analog of the Thermal Decomposition of Hydroxyapatite during Plasma-Spray Procedure.* Journal of Solid State Chemistry, 2001. **160**(2): p. 460-468.

11. Liao, C.-J., et al., *Thermal decomposition and reconstitution of hydroxyapatite in air atmosphere.* Biomaterials, 1999. **20**(19): p. 1807-1813.

12. Zyman, Z., et al., *Phase and structural changes in hydroxyapatite coatings under heat treatment.* Biomaterials, 1994. **15**(2): p. 151-155.

13. Gross, K.A., C.C. Berndt, and H. Herman, *Amorphous phase formation in plasma-sprayed hydroxyapatite coatings.* Journal of Biomedical Materials Research, 1998. **39**(3): p. 407-414.

14. Weng, J., et al., *Formation and characteristics of the apatite layer on plasma-sprayed hydroxyapatite coatings in simulated body fluid.* Biomaterials, 1997. **18**(15): p. 1027-1035.

Fig. 4-1 SEM image (a) and X-ray diffraction patterns (b) of the HA powder used in the study.

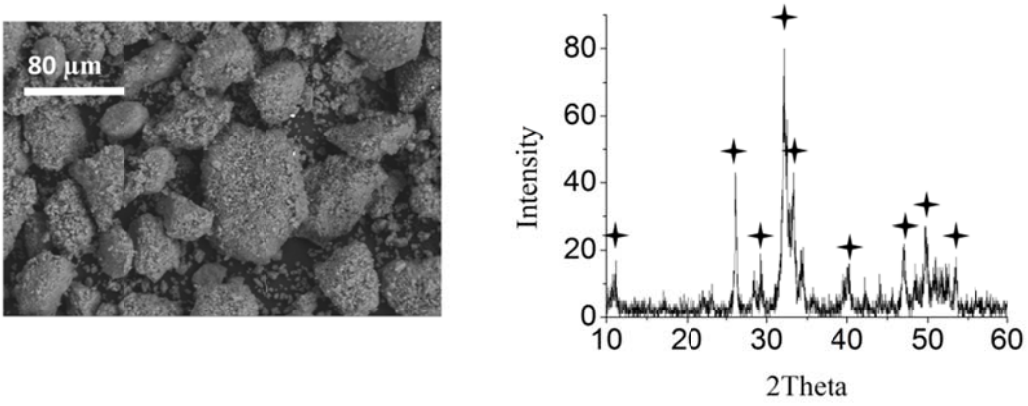

(a) (b)

Fig. 4-2 Temperature-Velocity distributions of HA particles as obtained by the experimental design.

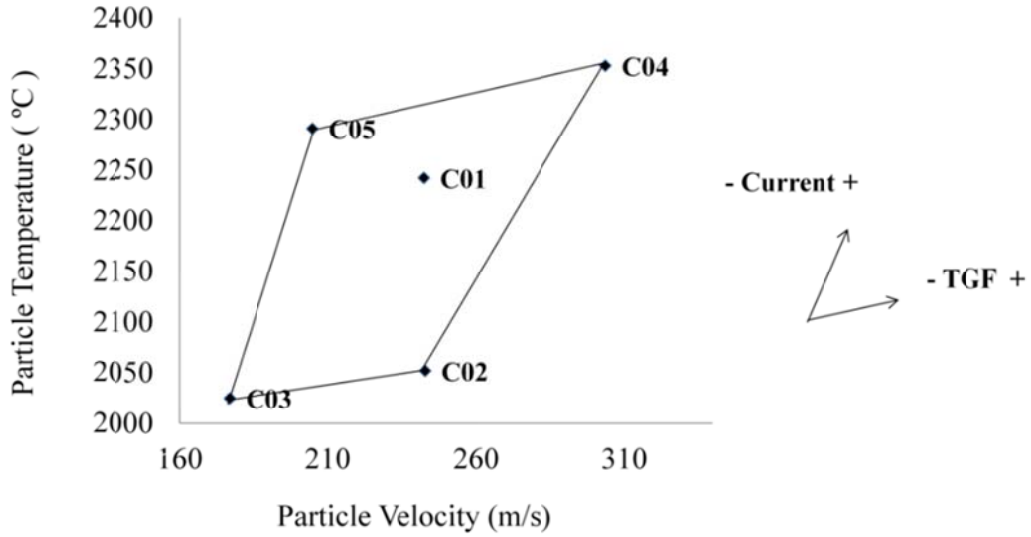

Fig. 4-3 Dependence of splat morphology on the melting index (MI) and kinetic energy (KE).

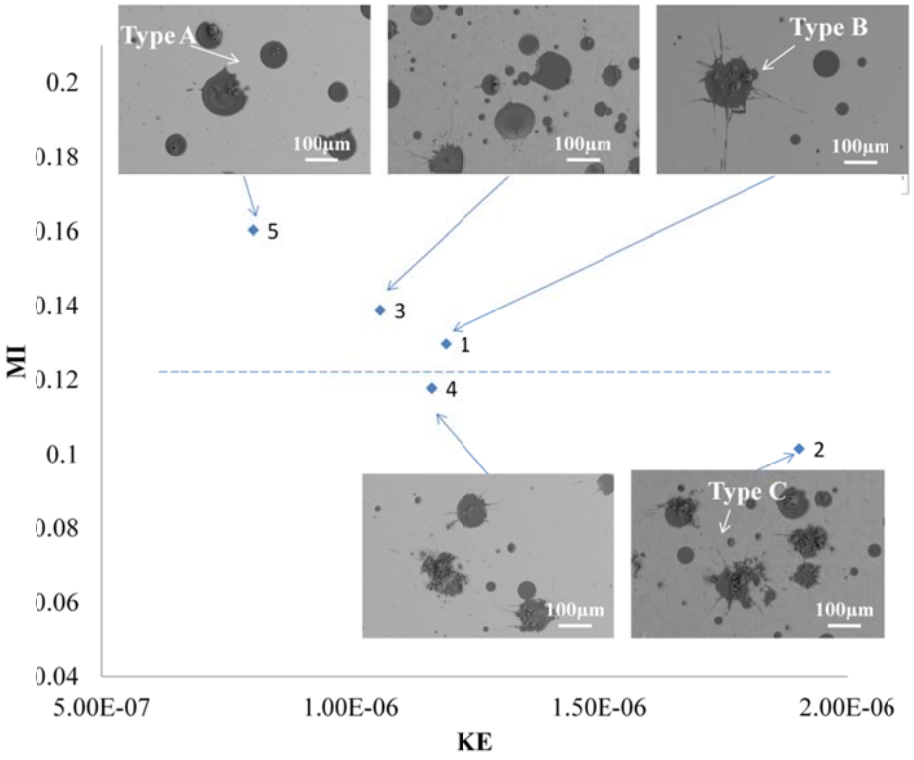

Fig. 4-4 (a) Melting index of particles with different size, (b) Kinetic energy of particles with different size (Condition 1, current 402 A, TGF: 50 SLM, from DPV 2000).

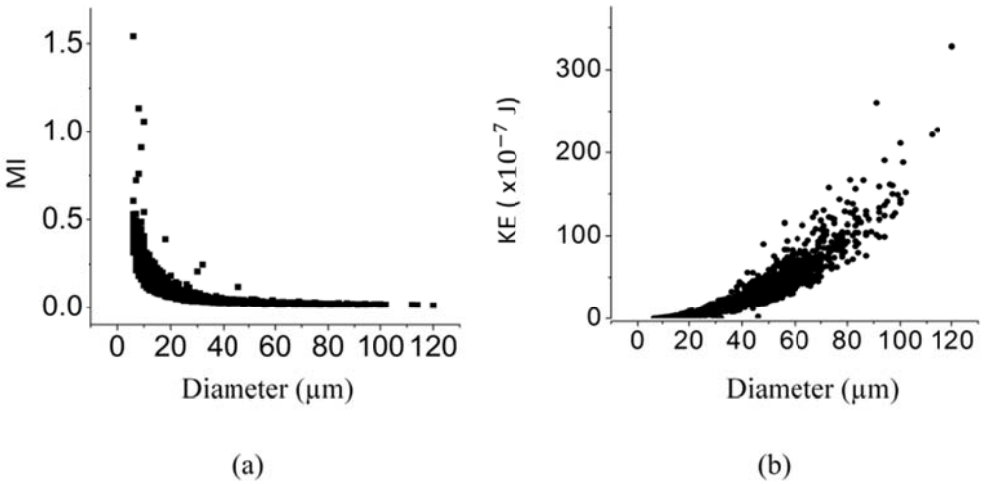

(a) (b)

Fig. 4-5 Cross sectional microstrures of as sprayed samples with and without cooling: (a) 1N sample; (b) 1C sample; (c) 2N sample; (d) 2C sample; (e) 3N sample; (f) 3C sample; (g) 4N sample; (h) 4C sample; (i) 5N sample; (j) 5C sample.

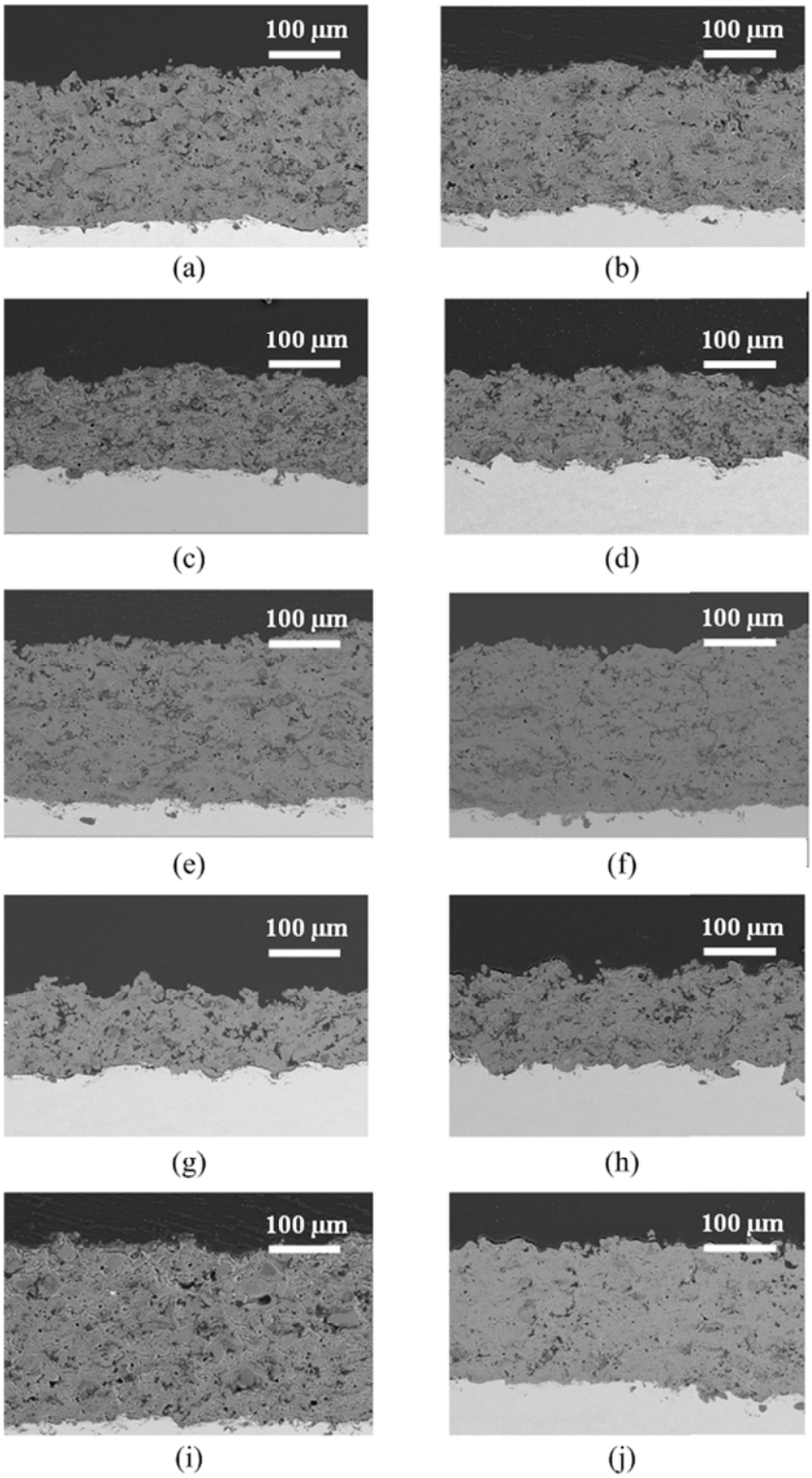

Fig. 4-6 Trapped air bubbles in splats: (a) Condition 1; (b) Condition 5, splats were deposited on the surface of substrate without cooling.

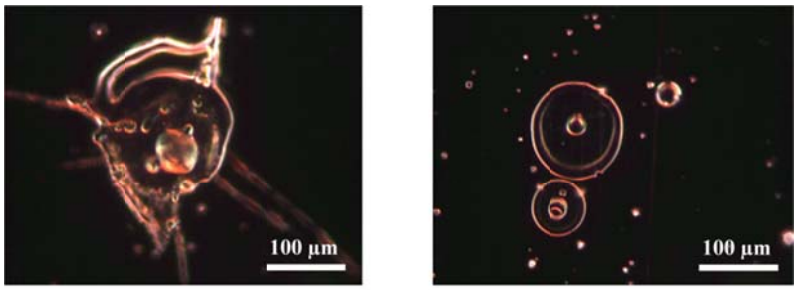

(a) (b)

Fig. 4-7 Comparison of the porosity of as sprayed samples: (a) porosity in the samples; (b) second-order process map of as sprayed samples' total porosity in MI-KE Space.

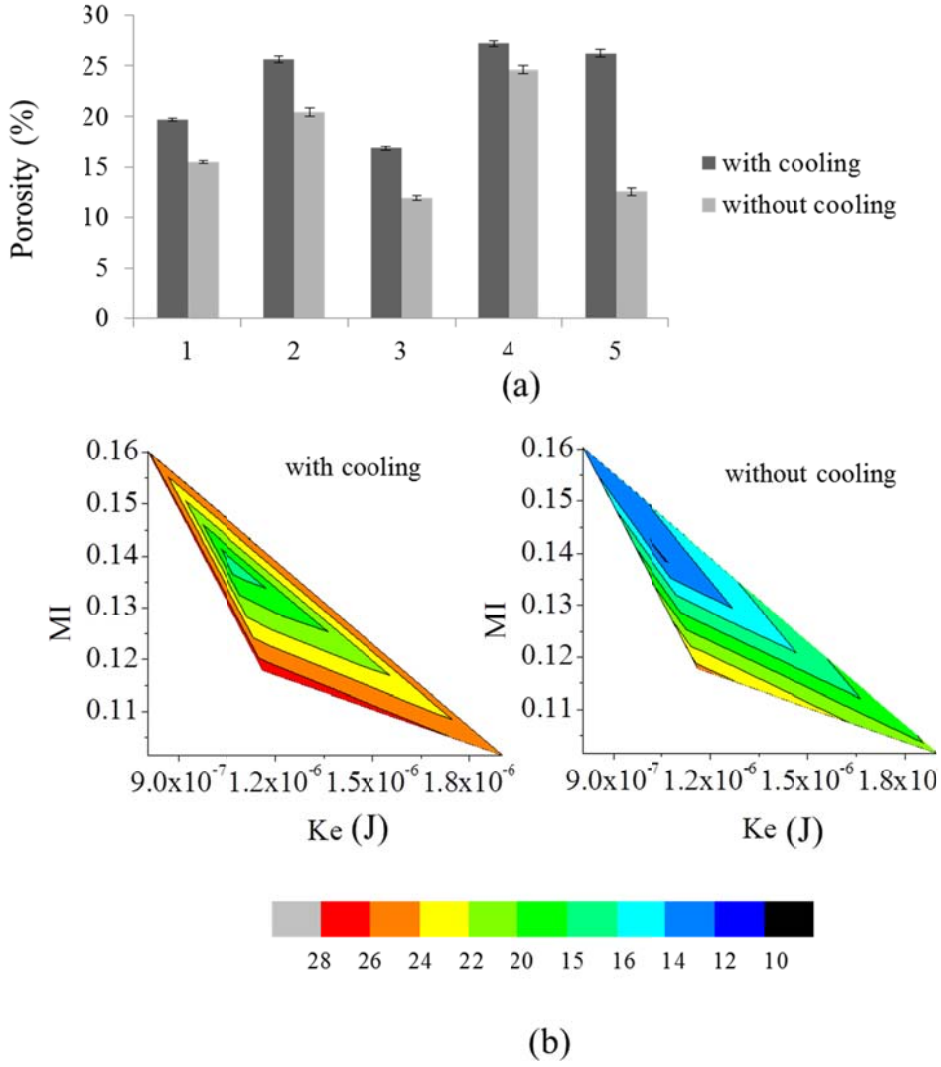

Fig. 4-8 (a) Comparison of the thickness of as-sprayed samples; (b) Comparison of the deposit efficiency of as-sprayed samples; (c) Second-order process map of deposit efficiency in MI-KE Space.

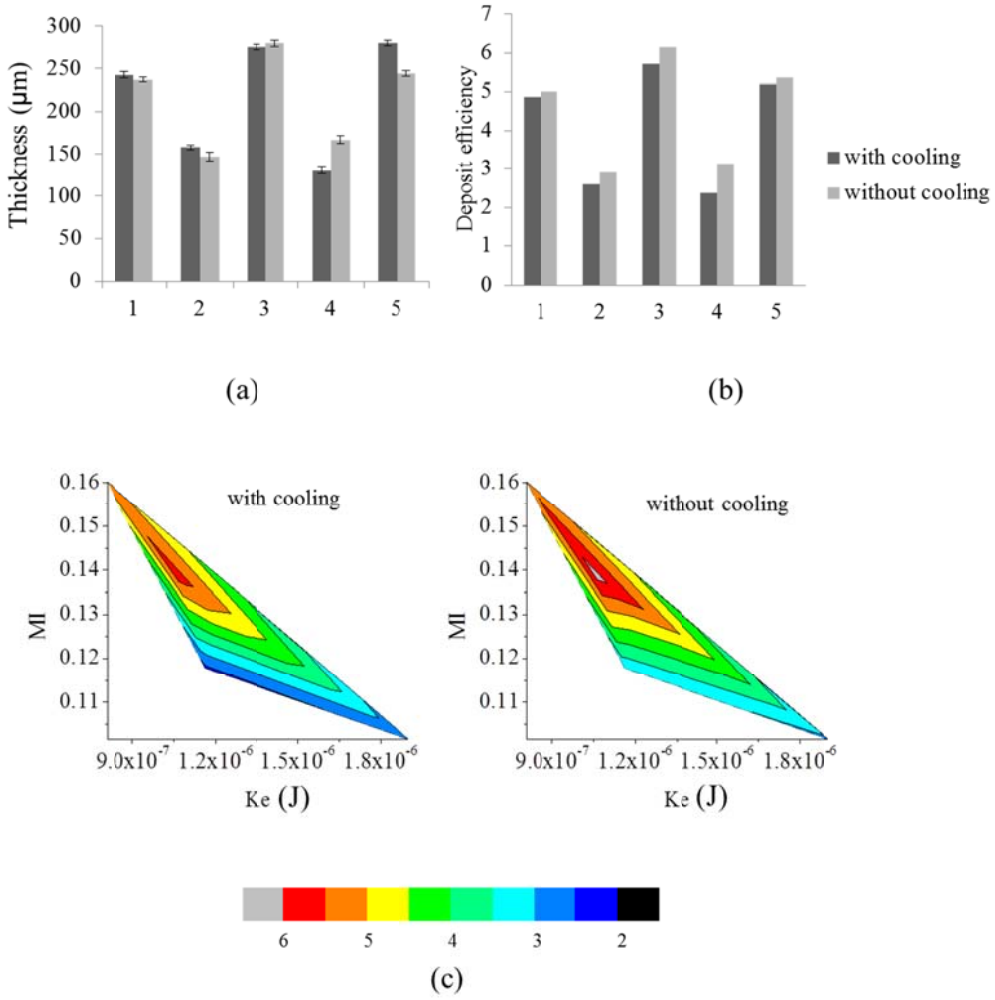

Fig. 4-9 X-ray diffraction patterns of as sprayed samples condition 2 and condition 5.

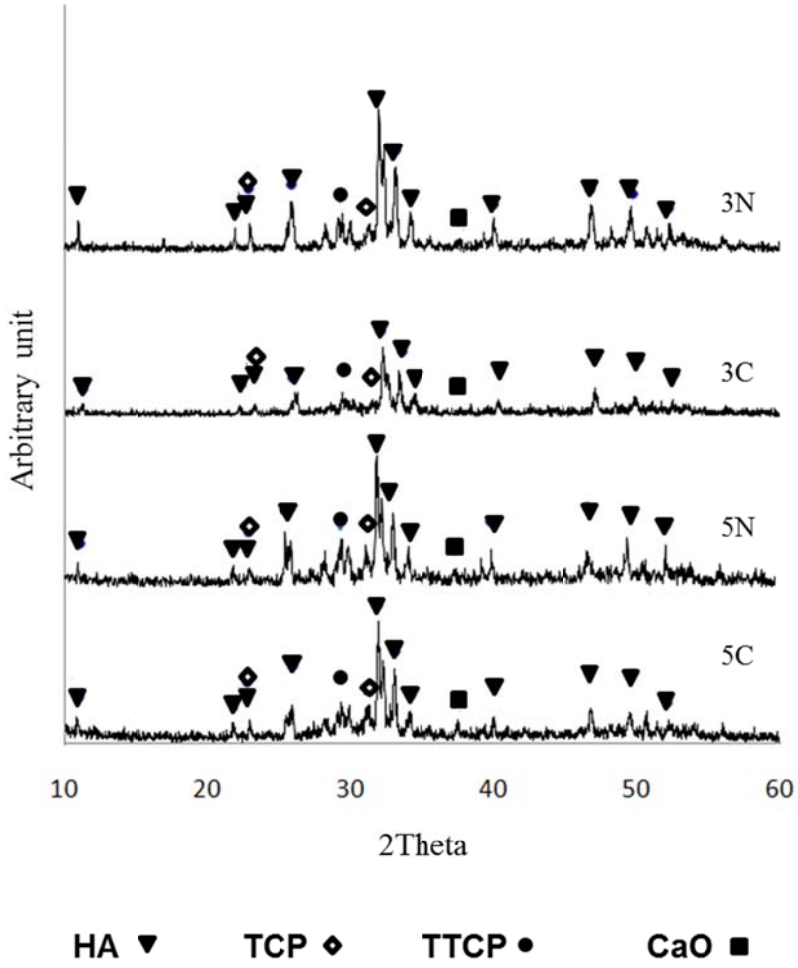

Fig. 4-10 (a) comparison of the crystalline of as sprayed samples, (b) second-order process map of as sprayed samples' crystallinity in MI-KE Space.

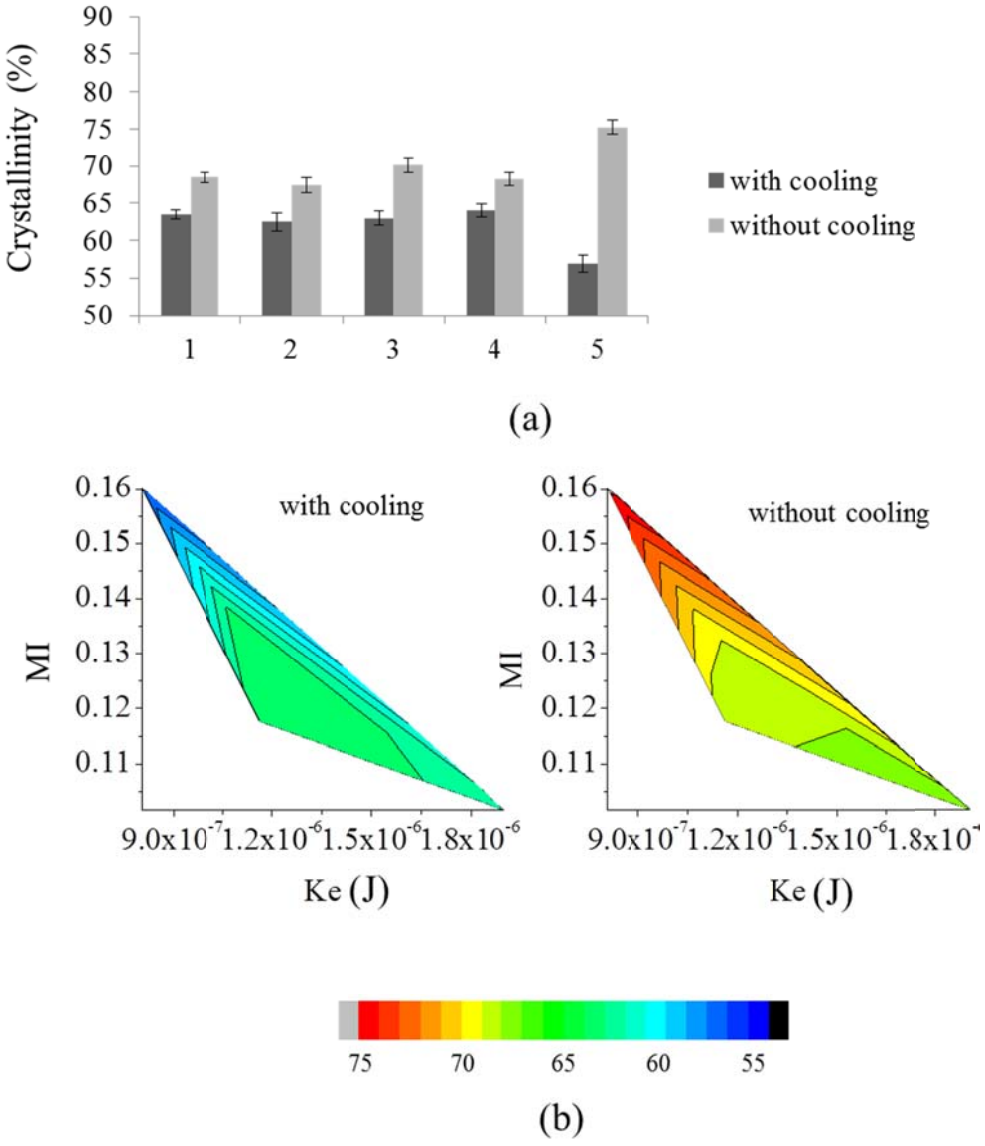

Fig. 4-11 comparison of as-sprayed samples and heat treated 4N samples after 6 weeks SBF test: (a) Top view of as sprayed sample after 6w SBF; (b) cross session view of as sprayed sample after 6 weeks SBF test; (c) top view of heat treated sample after 6 w SBF; (d) cross session of heat treated sample after 6 w SBF test.

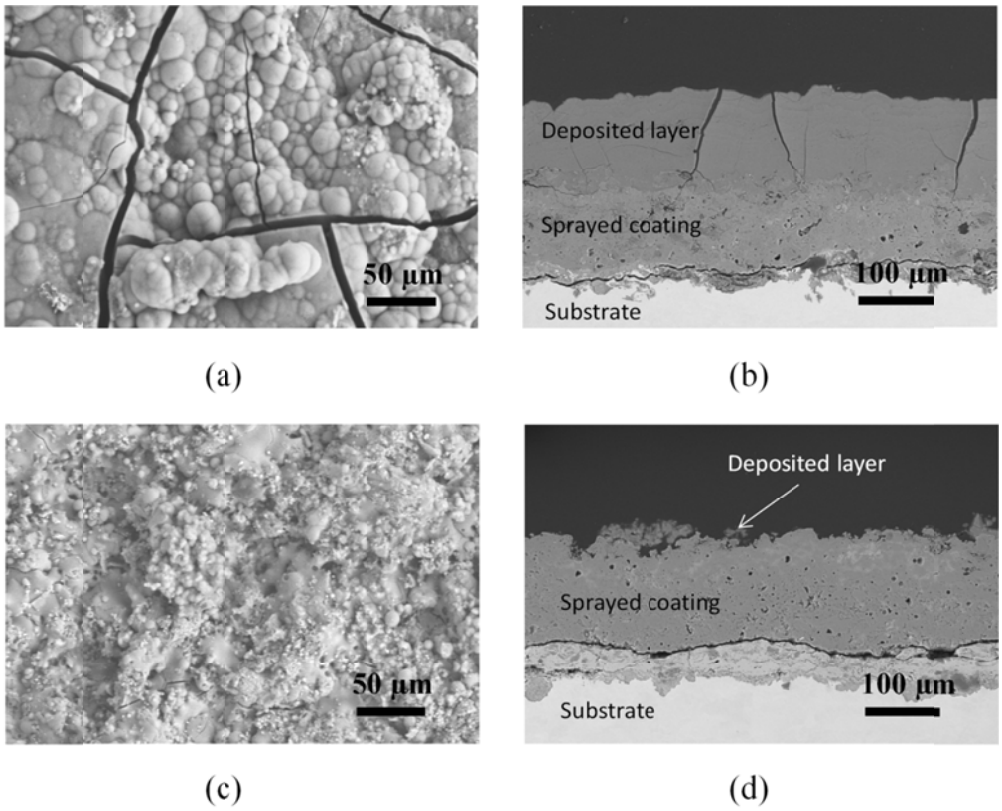

Fig. 4-12 XRD pattern of as sprayed, heat treated 4N samples before and after 6 weeks of SBF test.

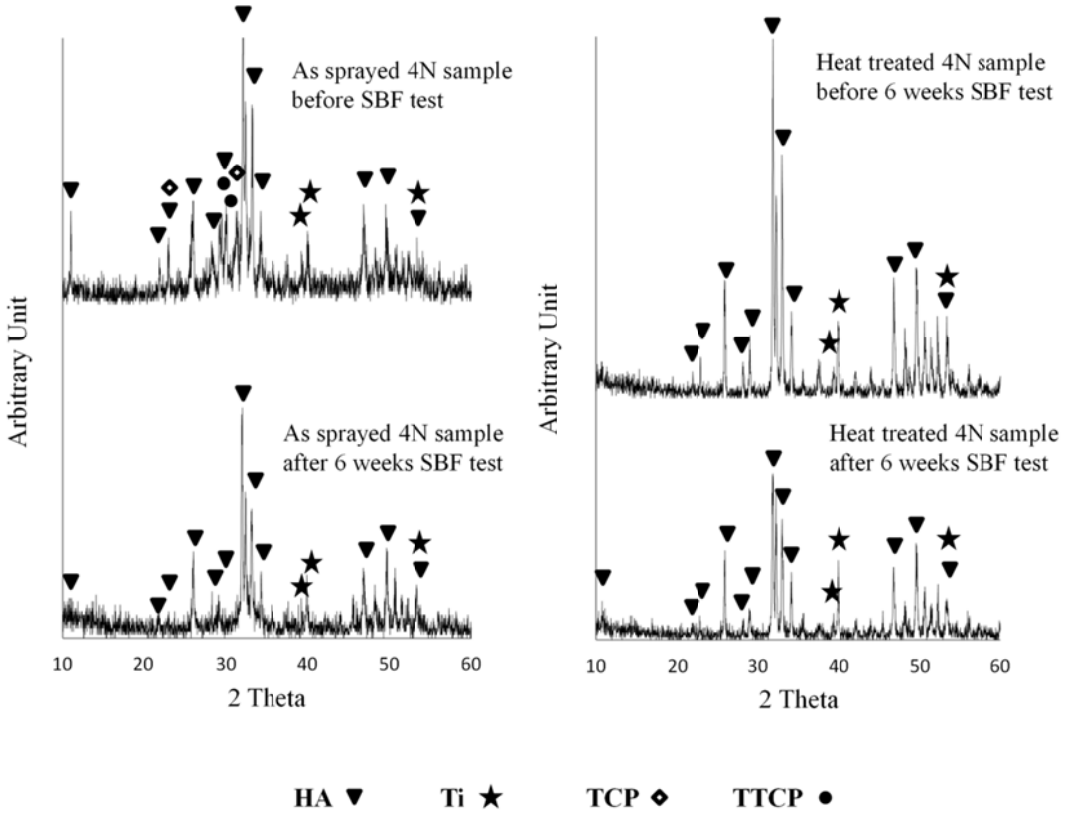

Fig. 4-13 (a) comparison of the thickness change of as sprayed samples after 6w SBF test, (b) second-order process map of as sprayed samples' thickness change in MI-KE Space.

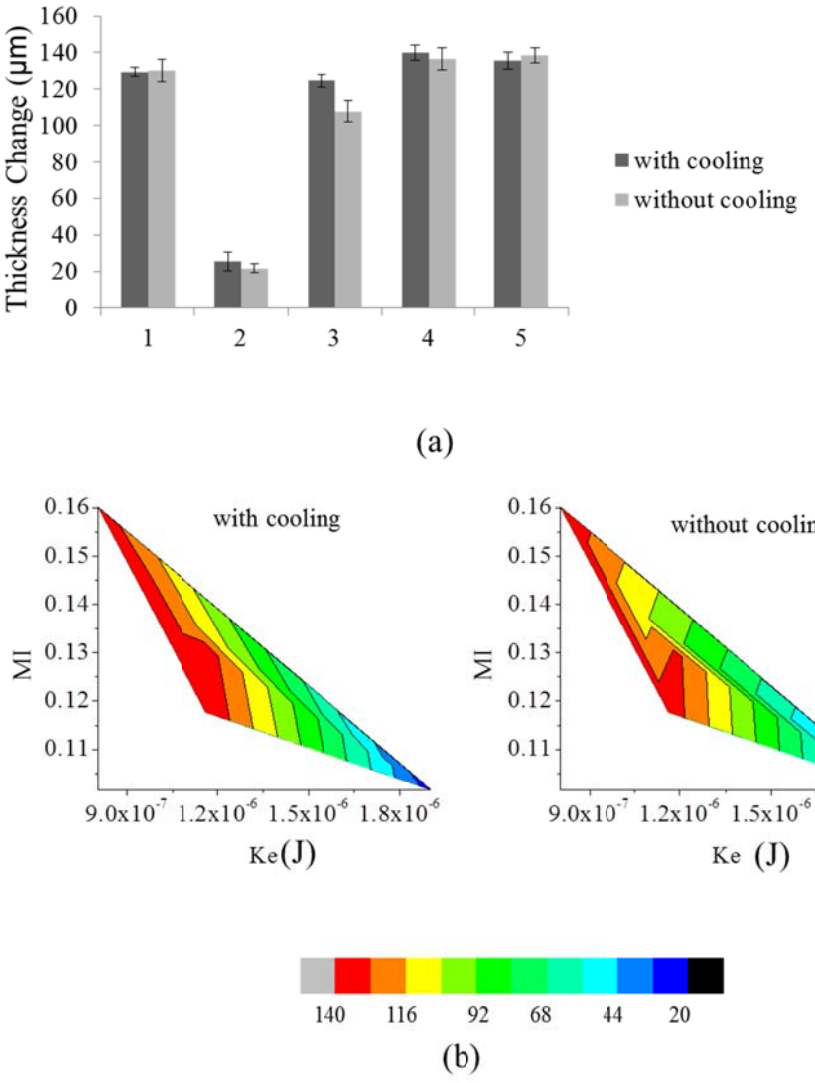

Chapter 5

COMPARISON STUDY OF STRONTIUM-DOPED CALCIUM PHOSPHATE COATINGS SYNTHESISED BY ELECTROCHEMICAL DEPOSITION AND AIR PLASMA SPRAY

5.1 Abstract

In order to understand how coating properties such as chemical composition and microstructure impact the bioactivity performances of calcium phosphate coatings, strontium-doped and pure Ca-P coatings were deposited using two different technologies: electrochemical deposition and air plasma spray. Various combinations of compositions and microstructures were obtained through manipulating the process parameters. The microstructures of obtained calcium phospahte coatings were observed through scanning electron microscopy. X-ray diffraction and energy dispersive X-ray spectroscopy were employed to study the chemical composition of the coatings. The cytocompatibility and bioactivity performances of the coatings were evaluated in MC3T3-E1 osteoblast-like cells culture system. The influences of phase composition and morphology as well as the doping of strontium as on the behaviors of the osteoblast-like cell were investigated.

5.2 Materials and Methods

5.2.1 Preparation of the Substrate

In this study, commercial Ti-6Al-4V titanium alloy plates were used as coating substrates in both of the air plasma spray and electrochemical deposition processes. Those plates have a dimension of 1.0 cm × 0.6 cm × 0.2 cm. Before coating deposition, substrates were grit-blasted and ultrasonically cleaned in acetone for 10 min, rinsed by deionized water and then air dried.

5.2.2 Electrochemical Deposition

In electrochemical deposition process, the electrolyte used in this study was prepared the same way as previous study, which has a total concentration of Ca^{2+} and Sr^{2+} 0.042M, and (Ca+Sr)/P molar ratio was maintained at 1.67.

During electrochemical deposition, the electrolyte's temperature was maintained at 90°C. Pulsed current was used, with one cycle including 1 min of current on for coating deposition, and 1 min with current off afterwards to reduce hydrogen bubbles

assembling. As shown in Table 5-1, according to the current density applied, 5~20 pulse-cycles were used for each of the conditions, that correspond to the total deposition time of 5~20 min. Through this way, the masses deposited under different current density can be maintained in similar amounts.

Table. 5-1. Electrochemical deposition parameters

Sample ID	Current Density (mA/cm2)	Number of Deposition Cycles	Ratio of Strontium in electrolyte (mol %)
ECa1	5	20	0
ECa2	10	10	0
ECa3	20	5	0
ESr1	5	20	10
ESr2	10	10	10
ESr3	20	5	10

After electrochemical deposition, the samples were washed using distilled water and then dried at room temperature.

5.2.3 Air Plasma Spray

Synthesized Sr-HA and pure HA powders were used for air plasma spray in this study. Both of the powders were produced by a wet chemical route developed by Shirkhanzadeh [1]. The powders were heat treated for two hours at 700°C. The obtained powders were comprised of agglomerated particles of nanocrystals with an average agglomerate size of 35 μm. The morphologies of the two powders are shown in Figs. 5-1(a), 5-1(b). XRD spectrums of the powders are shown in Fig. 5-1(c). All the major peaks

found in the spectrums belong to apatite. Although some miniscule peaks can be seen near the baseline, they should be attributed to the background noise. Due to the low doping dose of strontium, the crystal structure of doped powder did not show significant difference compared to those undoped one.

The powders were plasma sprayed by using a nozzle diameter of 7 mm with a Sulzer Metco F4 commercial plasma spray torch (Sulzer Metco, Westbury,NY). The standoff distance was 100 mm. Plasma gases contain Ar_2 and H_2, the total gas flow (TGF) was 50 SLM with a constant volume ratio of 9:1. Gun traverse speed was set as 500 mm/sec, and 15 passes for each coating. Argon was used as the carrier gas for the powder feedstock. The other spray parameters for APS are shown on Table 2.

Table. 5-2. Air plasma spray parameters

Sample ID	Current (A)	Voltage (V)	Power (KW)	TGF (SLM)	Ratio of Strontium in Spay Powder (mol %)
ACa	402	64.4	25.9	50	0
ASr	402	64.4	25.9	50	10

5.2.4 Characterization of the Deposited Coatings

The morphologies and composition of the coatings were investigated by scanning electron microscopy (LEO 1550) equipped with an energy dispersive X-ray spectroscope (EDS) function, under a 20keV accelerating voltage. The samples were gold coated before examination. Phase and crystal structure of achieved coatings were analyzed by X-ray diffraction (XRD) with the operating voltage of 40 kV and current of 25 mA. The diffractometer was set under the scanning speed of 2°/min over a 2θ from 10-60°, at a step size of 0.02°. The spectra were analyzed using JCPDS cards.

5.2.5 In Vitro Cell Culture Experiment

In vitro cell culture experiments were performed culturing osteoblast-like MC3T3-E1 cells (subclone 4; American Type Culture Collection, Manassas, VA) on the

samples in an 8-day cell growth period. Sr-doped and pure Ca-P coatings fabricated by two processes, ECP and APS, under different process parameters were tested.

Before cell culture, samples were sterilized by soaking in 70% ethanol for 4 hours and rinsing with sterile phosphate-buffered saline (PBS). The osteoblast-like MC3T3-E1 cells were then seeded onto the coatings at an initial density of 4000 cells/cm2, and placed in 6-well TC plates (BD Falcon) containing culture medium. Culture medium was α-MEM (Invitrogen, Carlsbad, CA) with 10% fetal bovine serum (FBS; Hyclone, Logan, UT), 100 units/mL penicillin and 100 mg/mL streptomycin (Invitrogen), 50 mg/mL L-ascorbic acid, and 4mMb-glycerophosphate (Sigma-Aldrich). The samples were then incubated at 37° C (5% CO_2, humidified). Fresh culture medium was given every 2 days.

5.2.6 Cell Morphology

Cells were prepared for SEM by first being fixed in 2.5% glutaraldehyde at pH 7.4, 0.1 M potassium phosphate buffer for 8 hours and dehydrated by graded ethanol (35%, 50%, 70%, 95%, and 100%) at 10 min each. Samples were then immersed in 50% HMDS (hexamethyldisilazane) solution in ethanol for 10 min, 100% HMDS for another 10 min, and air dried overnight and stored in a dessicator. Before SEM examination, the samples were sputter coated with gold. The cell morphology on each sample was investigated under SEM using beam voltages of 2.5 keV.

5.2.7 Cell Proliferation

The proliferation of the cells was evaluated during the 8-day cell growth period. Cell counting was performed on day 4 and day 8 using the following procedures. At each time point, the cells were rinsed with PBS, and then fixed by 3.7 vol. % formaldehyde in PBS after rinsing thoroughly three times with PBS. The nuclei of the cells were visualized by staining with 2.5 μg/ml 4', 6-diamidino-2-phenylindole (DAPI). Sixteen fluorescence pictures were taken for each sample using an inverted microscope (Olympus IX71) with a CCD camera attachment. The cell area density was then determined and averaged from the fluorescence pictures of two samples for each case.

5.3 Results and Discussion

5.3.1 Morphologies and Microstructures of the Coatings

The surface morphologies of as-deposited coatings were investigated by SEM, and represented in Fig. 5-2. Fabrication methods and process parameters had significant impact on coating morphology. In the ECD process, various coating morphologies can be obtained by changing the current density and dose of Sr. It can be seen from Fig. 5-2(a) and 3(b) that a coating morphology with a mixture of needle-like and faceted structures was obtained under 5mA/cm^2 and 10 mA/cm^2 current density in undoped Ca-P coating. With the increase of current density, coating morphology experienced a conversation from faceted crystallite shape to needle-like shape. Faceted-crystallites become smaller and even disappeared when current density reached 20 mA/cm^2 (Fig. 3(c)), while needle-like crystals became the dominant phase in the coatings. The morphology evolution trends of undoped and Sr-doped coatings were similar. However, compared to undoped coatings (Fig.5-2 (a), (b), (c)), Sr-doped ones (Fig.5-2 (d), (e), (f)) contained more faceted crystallites under the same deposition parameters. A structure dominated by faceted crystallite morphology was typically seen for samples prepared at low current density (5 mA/cm^2) (Fig. 5-2(a) and 5-2(d)).

Fig. 5-2(g) and 5-2(h) illustrate the top view of APS undoped and Sr-doped coatings respectively. The APS coating surfaces have a typical surface morphology including unmelted or partially melted apatite spheres, flatten splats and cracks. There is no appreciable difference in morphology were observed between APS Sr-doped Ca-P coatings (Fig. 5-2(h)) and undoped ones (Fig. 5-2(g)).

The cross-sectional morphologies of the coatings are presented in Fig. 5-3(a)-(h). It can be observed that, for electrochemical deposition, thicknesses of the coatings range from 15μm to 20 μm. Some voids were found between coating and substrate, which is due to the hydrogen bubble forming during deposition. Plasma sprayed coatings were approximately 40 μm thick and also contained porosity (Fig. 5-3(g) and 5-3(h)). Chemical Composition and Phase Identification of the Coatings

X-ray diffraction patterns for the coatings are shown in Fig. 5-4. Intense peaks from titanium (filled star symbol) can be found in all patterns, because the coatings are thin and porous. In thin coatings, peaks of Al_2O_3 (filled square symbol) can also be found due to the residue of alumina during grit-blasting process. The X-ray diffraction spectra indicate that different phases can be found in electrodeposited coatings and APS coatings. The phase compositions of the coatings are dependent on the process parameters.

ECD coatings contained different Ca-P phases including hydroxyapatite (HA, $Ca_5(PO_4)_3OH$) (filled triangle symbol) and monetite (dicalcium phosphate, $CaHPO_4$) (cross). Phase composition changed with the change of current density. For samples deposited under low current density, the intensity of monetite peaks increased, and the peaks from hydroxyapatite became weaker. That could be attributed to the change of pH value as discussed in previous chapter: under low pH value, monetite could be formed instead of HA during electrochemical deposition[2]. Therefore, the faceted crystals were found in the ECD coatings prepared under low current density (Fig.5-3(a), (d)) were most likely monetite, while the needle-like crystals in Fig.5-3(b), (c), (e) were likely to be HA. Deposited HA has preferred orientation. HA has a hexagonal structure, the [002] plane is the most densely plane-packed, thus usually [002] is the preferred growth direction, which is confirmed by the SEM morphology study, where oriented growth of needle-like crystal was found.

For APS coatings, besides HA (filled triangle), TCP (tricalcium phosphate,) (unfilled diamond) and TTCP (tetracalcium phosphate,) (filled circle) were found in both of the doped and undoped coatings, as shown in Fig 5-4 (g), (h). As discussed before, TCP and TTCP were the decomposition products of HA.

Usually, doped strontium in calcium phosphate causes the shift of XRD pattern to the lower Bragg angles. However, in the present study, due to the relatively low dose, strontium did not seem to have a significant influence in the crystal structure either ECD or APS coatings (Fig. 5-4).

The elemental analysis of the deposited coatings was performed by EDS as shown in Fig. 5-5. The presence of the Sr element can be observed in the deposited Sr-doped coatings as a small peak/shoulder to the left of the P peak (Fig. 5-5(d), (e), (f), (h)) are

confirmed. This indicates that strontium can be incorporated into the coating using both ECD and APS process.

5.3.2 Cellular Response

Interactions between bone and the implant surface are very essential for bioactivity of these materials. Cell morphology and proliferation, as two important factors to evaluate the bioactivity of the coatings, were investigated in the present study.

Cell culture experiments demonstrated that osteoblast-like cells were able to attach to all of the coatings. However, the morphologies of the cells on the samples are quite different. Fig. 5-6 shows the SEM morphologies of osteoblast-like cells on the coatings after 8 days culture. Coating composition and morphology have a dramatic effect on cell morphology, as cells found on faceted crystallites ECD coatings (Fig. 5-6(a), (d)), showing a flattened appearance. While on the surface of APS coatings (Fig. 5-6(g), (h)) and needle-like crystallites ECD coatings (Fig. 5-6(c), (f)) the cells were found to spread less and with a more elongated shape and spindle–like structures extending from the cell body to the coating surface. On coatings with a mixed morphology (Fig. 5-6(b), (e)), cells were more often found to attach to and spread out on the faceted structures than on the needle-like surfaces.

To study biocompatibility of these coatings, cell proliferation on coatings was quantitatively investigated. Fig. 5-7 shows the average growth rate of the MC3T3-E1 osteoblast-like cells during the 8-day cell culture. It should be noted that, compared with undoped samples (Fig. 5-7(a)-(c)), more cells were visible on the strontium doped ECD samples (Fig. 5-7(d)-(f)) fabricated under same process and parameters. On the Sr-doped sample prepared at the lowest current density (Fig. 5-7(d)), there was the greatest number of cells compared to all the other samples. These results indicated that the incorporation of strontium in calcium phosphate coatings most likely had a beneficial effect on the growth of cells on the coating surface. Comparing two groups of samples: APS sample g and h, ECP sample c and f, under similar phase and morphology, Sr-doped samples had more cells attaching at each time point.

The phase and morphology of the coating also had significant influence on the proliferation rate of the cells.

Comparing samples with the same strontium levels, among Sr-doped samples, more cells were found on coatings that were prepared at the lowest current density ($5mA/cm^2$) (Fig. 5-8), which has more faceted monetite deposition on the surface to which the cells preferred to attach (Fig. 5-7(d)). Cells on the APS coatings were more viable than the pure ECD prepared coatings with needle-like HA crystals, but not as viable as the Sr-doped ECD coatings with faceted monetite crystallites. It is needed to point out that the number of cells that were still attached on the sharp needle-like undoped ECP samples on day 8 was slightly less than on day 4. Possible explanation for this phenomenon may be that the cells were migrating out of the coatings or were killed by toxic residues in the coating.

However, it is not very clear which factor contributed most to the morphology of the cells, coating morphology and phase or strontium dose, because the incorporation of strontium was also accompanied by the changes of phase and morphology. Introduction of more monetite phase may change the activity of the materials. Because monetite phase has higher solubility comparing to HA, that may increase the dissolution rate of Ca-P coating, and change the releasing behavior of Sr^{2+}, Ca^{2+} and phosphate ions to the environment, which may make Ca-P coating more bioactive. Further study is needed using a more systematic approach to investigate these factors more thoroughly.

The result from the cell culture studies suggested that increased cell proliferation is highly correlated with a greater spreading rate of cells on the sample surface.

It needs to be pointed out that more cells were visible on the surface of control (Ti6Al4V plate without coating) compared to coated samples at each time point. The reason for that may be due to the detachment of the cells from coated samples due to the dissolution of the coating during cell culture. Also cells could be more visible on flat surface of Ti6Al4V compared to rough surface of coating, where they may be hidden in the valley of the rough surface.

5.4 Conclusions

Sr-doped calcium phosphate (Ca-P) coatings with different microstructures and morphologies have been successfully obtained using electrochemical deposition (ECD) and air plasma spray (APS) technologies. In electrochemical deposition process, faceted crystals of monetite and HA or Sr-HA with needle-like shape were synthesized by controlling the current density level. Doped strontium in general introduced more monetite phase into electrodeposited calcium phosphate compared to the pure HA coatings deposited under the same process parameters. Ca-P coatings produced by APS had the typical surface morphology containing unmelted or partially melted apatite spheres, cracks and flatten splats.

Morphology and proliferation of the cell were highly dependent on the chemical composition, topography and surface roughness of the materials. For both of the ECD and APS Ca-P coatings, the doping of strontium showed a positive effect on the proliferation of MC3T3-E1 osteoblast-like cells. Morphology and phase composition of the coatings also had dramatic influences on the bioactivity of these coatings: cells preferred to attach and grow on the faceted monetite surface of ECD coatings prepared at lower current density than relatively smooth APS Ca-P coatings or sharp needle-shape HA surface produced by ECD at high current density. Therefore, although usually HA were considered as a bioactive materials with high osteoconductivity, in this study, a needle-like HA surface fabricated by electrochemical deposition was not identified to be a favorite substrate for the growth of the cells.

Different responses of the osteoblast-like cells to the coatings were observed which should be attributed to a combination of influences from various factors including strontium dose, surface morphology and phase composition of the deposited mineral.

5.5 References Cited

1. C.M. Mardziah, I.S.a.S.R., *Strontium-Doped Hydroxyapatite Nanopowder via Sol-Gel Method: Effect of Strontium Concentration and Calcination Temperature on Phase Behavior.* Trends Biomater. Artif. Organs, 2009. **32**(2): p. 105-113.

2. Blackwood, D.J. and K.H.W. Seah, *Electrochemical cathodic deposition of hydroxyapatite: Improvements in adhesion and crystallinity.* Materials Science and Engineering: C, 2009. **29**(4): p. 1233-1238.

Fig 5-1 Morphology of the powders synthesized: (a) HA powder, (b) Sr-HA powder, (c) XRD spectrums of the powders.

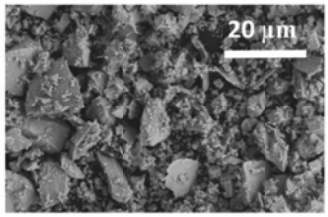

(a)

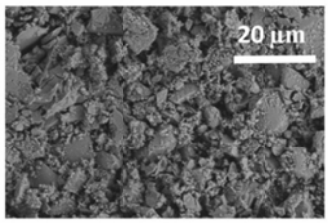

(b)

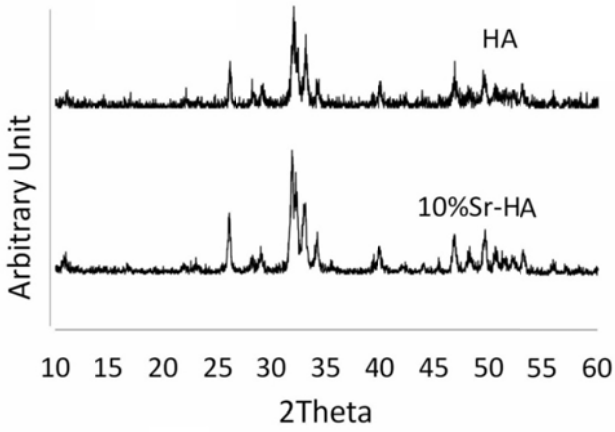

(c)

Fig. 5-2 SEM micrographs of the top view of coatings on titanium substrate produced by electrochemical deposition with (a) ECa1, (b) ECa2, (c) ECa3, (d) ESr1, (e) ESr2, (f)ESr3 and air plasma spray with (g) ACa, (h) ASr.

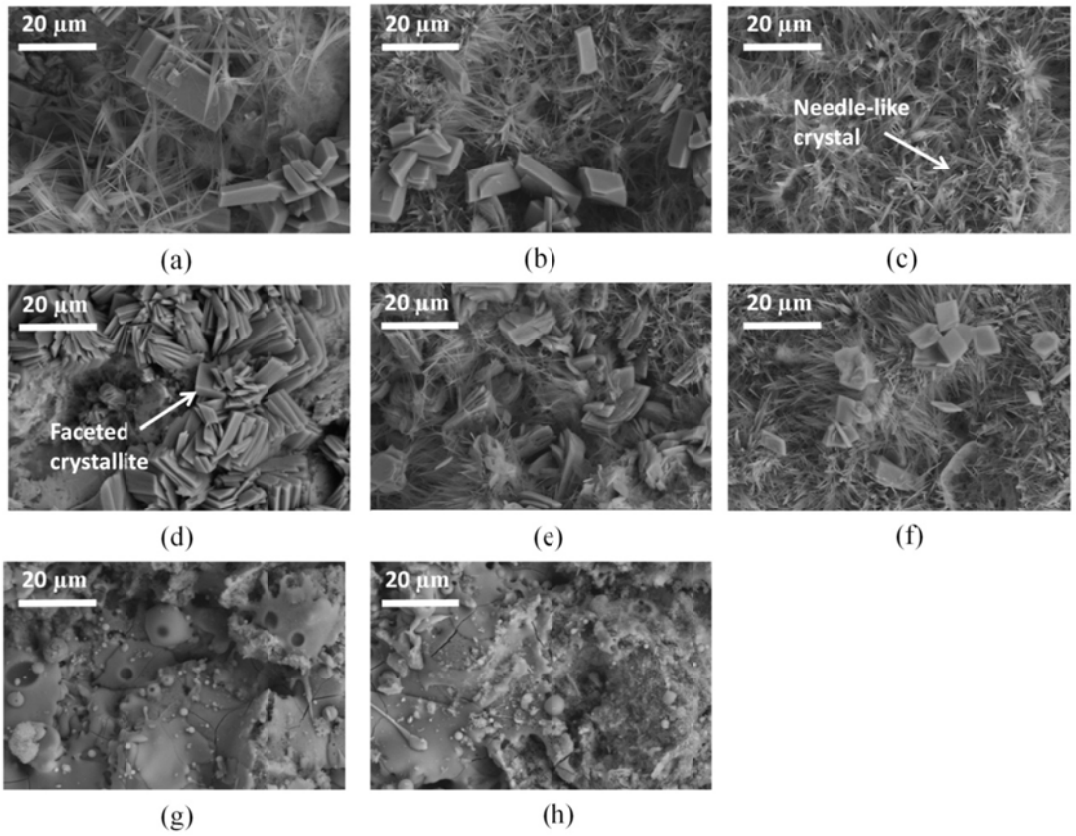

Fig. 5-3 SEM micrographs of the cross section of coatings on titanium substrate produced by electrochemical processing with (a) ECa1, (b) ECa2, (c) ECa3, (d) ESr1, (e) ESr2, (f)ESr3 and air plasma spay with (g) ACa, (h) ASr.

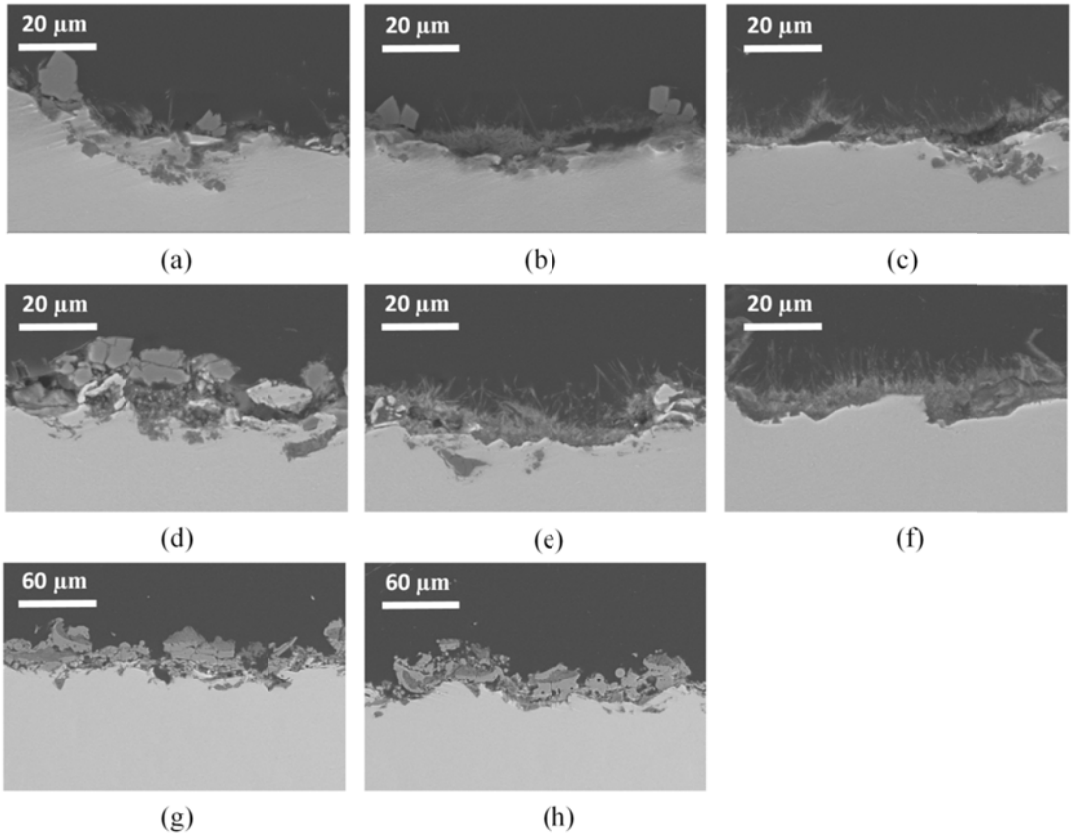

Fig. 5-4 X-ray diffraction spectra for: electrochemical deposited coatings with (a) ECa1, (b) ECa2, (c) ECa3, (d) ESr1, (e) ESr2, (f) ESr3 and air plasma sprayed coatings with (g) ACa, (h) ASr.

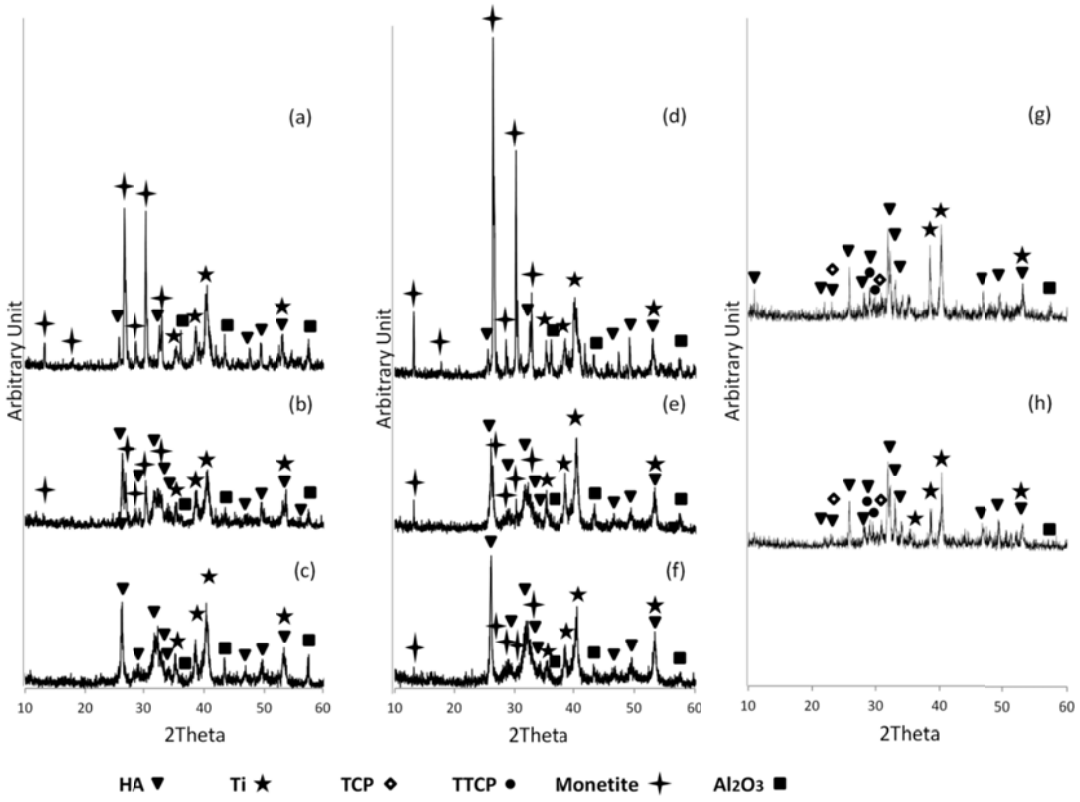

Fig. 5-5 EDS spectra for: coatings on titanium substrate produced by electrochemical processing with (a) ECa1, (b) ECa2, (c) ECa3, (d) ESr1, (e) ESr2, (f)ESr3 and air plasma spray with (g) ACa, (h) ASr.

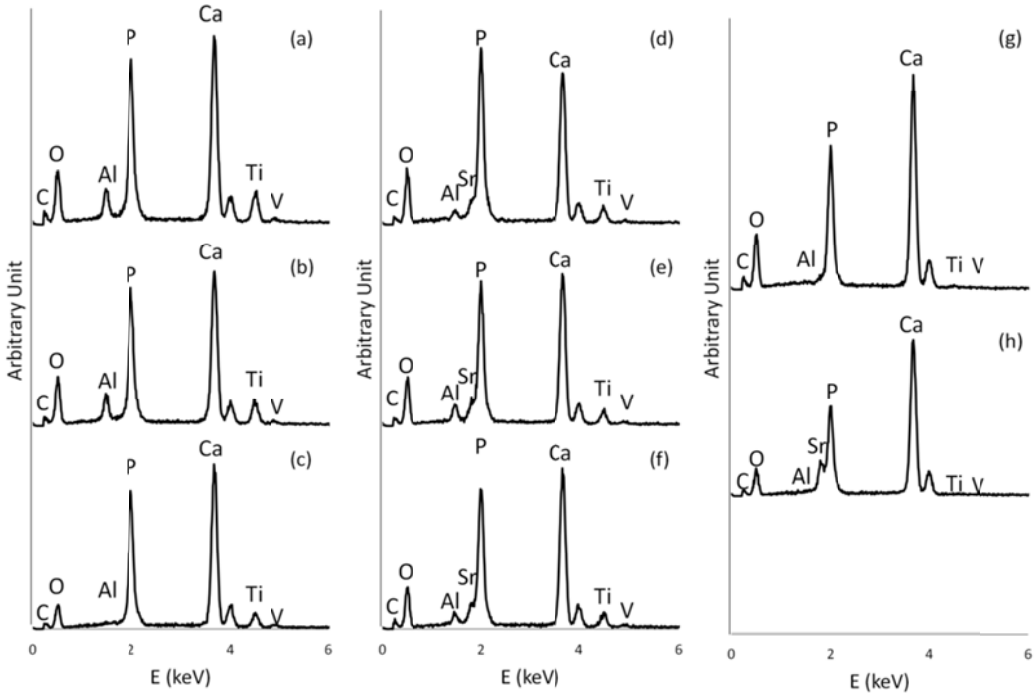

Fig. 5-6 SEM images of the cell morphologies on electrodeposited coatings: (a) ECa1, (b) ECa2, (c) ECa3, (d) ESr1, (e) ESr2, (f) ESr3 and APS coatings with (g) ACa, (h) ASr.

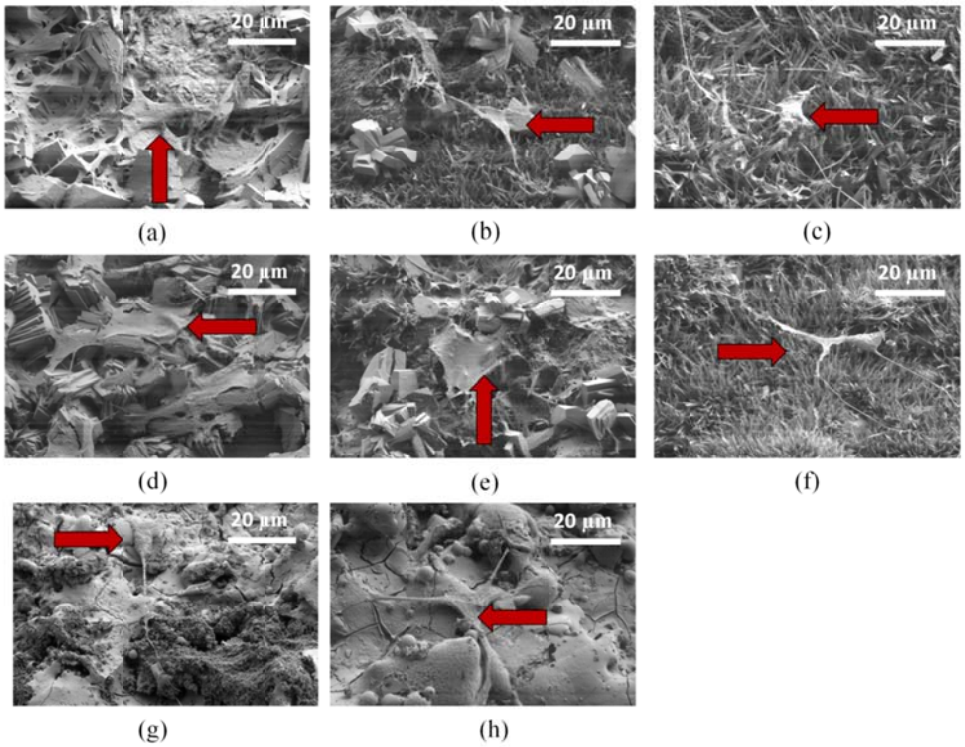

Fig. 5-7 Cell culture results of electrochemical deposited samples and air plasma sprayed samples from growth curve: (a) ECa1, (b) ECa2, (c) ECa3, (d) ESr1, (e) ESr2, (f) ESr3, (g) ACa, (h) ASr and (i) control (Ti6Al4V).

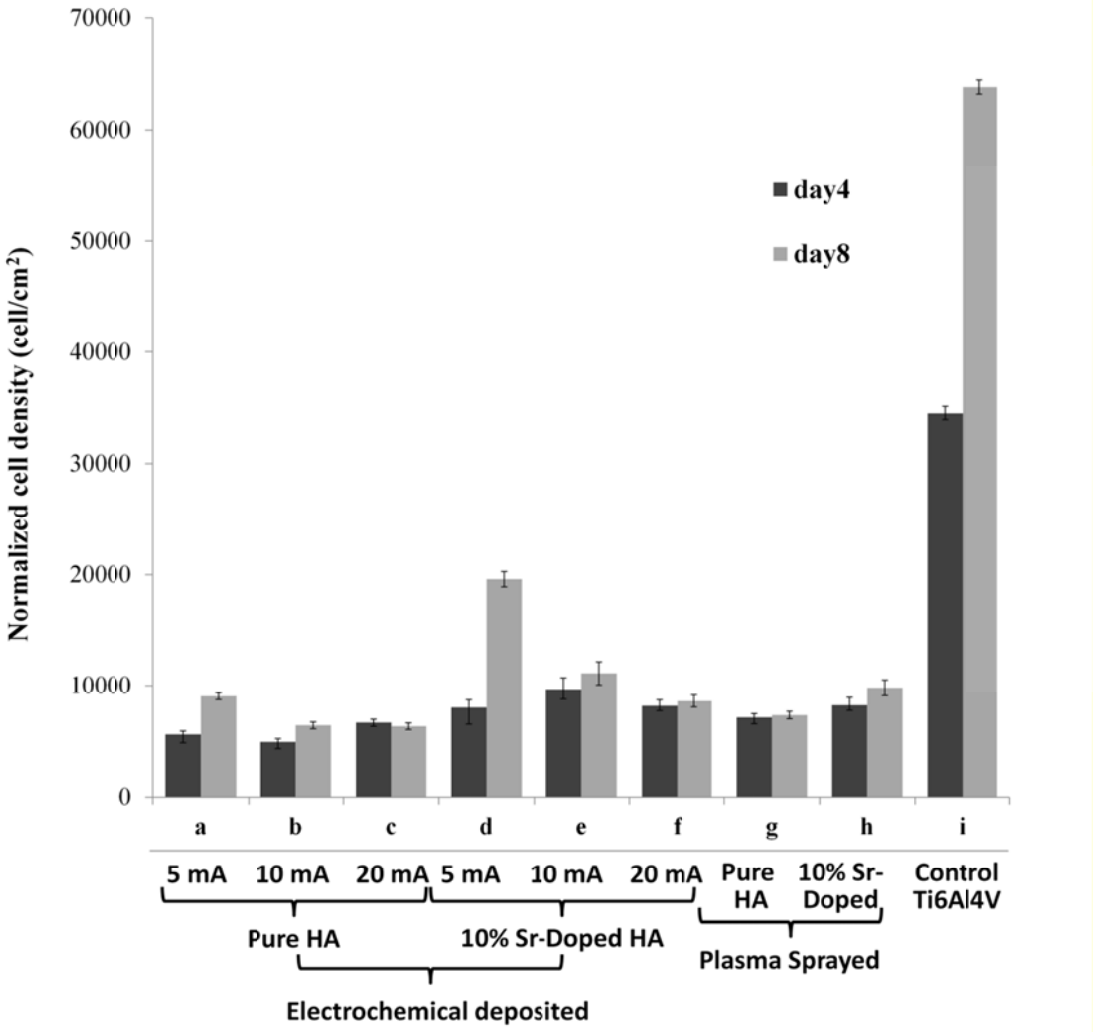

Chapter 6

SUMMARY

In this dissertation research, with the aim to develop bioactive calcium phosphate based coatings for medical application, pure and strontium doped calcium phosphate coatings with different chemical composition and microstructures were investigated. Two different technologies, electrochemical deposition and air plasma spray, were employed to synthesize the coatings. The coating properties were evaluated through multi-scale experimental methodologies and examinations ranging from cross section and surface morphology examination, thickness and porosity measurement, phase identification and in vitro bioactivity tests, and the connections between process parameters, coating properties and performance have been carefully analyzed. The study provided further understanding of the fundamental mechanism of the processes and the process-product relationship, thus can contribute to further improvements of the engineering processes. Here the significant findings and conclusions are summarized.

The work with electrochemical deposited calcium phosphate coatings (Chapter 3) was mainly focused on the investigation of the mechanism of the process and how to achieve coatings with different morphology and content by manipulating process parameters. A series of designed experiments were performed to evaluate the influences of several process parameters on the coating properties, including current density, concentration, temperature and pH value of the electrolyte as well as the dose of strontium.

A model describing Ca-P electrocrystallization behaviors during electrochemical deposition process was built based on classic theories of thermodynamics and kinetics. This model can explain the experimental results very well. For example, in this study, the main components of the electrodeposited coatings were DCPD and HA. There was not significant amount of OCP detected, although in some other literatures, OCP is a common phase presenting in the ECD coating. That is because in most of the experiments carried out during this study, the electrolyte temperature is relatively high (70 or 90 degree C) the saturation index (SI) of OCP has the value below zero, which means OCP couldn't be a possible phase. While deposition happens under room temperature, with the above zero saturation index (SI), OCP can become a possible phase as noted in literature. Through thermodynamic calculation, the nucleation rate of DCPD in most of the cases was much higher than HA and OCP, especially under low pH, low current density

conditions. Therefore, this model can be used a tool to predict and tailor the properties, especially chemical composition, in electrochemical deposition process, thus is meaningful.

The research with air plasma sprayed calcium phosphate coating was presented in Chapter 4, with the purpose of achieving better control over the complex synthesize process. In this research, a process map strategy was used as a tool to investigate the process – product relationship for calcium phosphate coatings. Two key process parameters were identified: current and TGF which dramatically impacted the in-flame particle state, the morphologies of the coating building blocks (splats), and eventually the coating properties including coating's porosity, chemical composition, deposit efficiency.

The in-flame particle state was quantified by melting index (MI) and kinetic energy (KE) of the particles. Coating properties such as porosity, crystallinity and deposit efficiency were found significantly influenced by particle state and substrate condition (with or without cooling). The graphic contours of those properties in MI-KE space were obtained, which connected the particle state and coating properties. Through in vitro SBF testing, the bioactivity of the synthesized Ca-P coatings was found to be related to the crystallinity, and the type and number of pores and thickness of coatings.

Thus the links between process—> particle state—> property —> performance were built for plasma spray calcium phosphate process. Compared with other researches in literatures, which mainly investigated single or a few process parameters' impacts on coating properties, the APS process map is a more convenient and efficient way to optimize the process.

Additionally, in order to better understand the how coating morphology and composition influence the bioactivities of the coatings, a comparison study was conducted using Sr-doped calcium phosphate coatings produced by electrochemical deposition and air plasma spray. Ca-P coatings with various combinations of morphologies and composition were obtained through controlling the process parameters including coatings containing faceted crystallites of monetite and needle-like HA crystals produced by electrochemical deposition; air plasma sprayed coatings with a surface

morphology including unmelted or partially melted apatite spheres, flatten splats and cracks.

The in-vitro cell culture experiment using osteoblast-like MC3T3-E1 indicated that cells reacted differently to different phase and morphology: compared to smoother APS Ca-P coatings or sharp needle-shape HA surface produced by ECD, a faceted monetite surface produce by ECD was a better substrate for the cell attachment and growth. Another significant finding was that the incorporation of strontium benefited the proliferation of osteoblast-like cells, thus strontium should be considered to be a positive factor to enhance the bioactivity performance of calcium phosphates.

The experimental results supported that as an alternative method to plasma spray, electrochemical deposition is definitely a promising technique to fabricate calcium phosphate coatings for biomedical application, which is a more economical technology compared to plasma spray. Furthermore, with the thermodynamic and thermokinetic models built, this process can be well controlled and the product can be predicted and tailored.